5-2014

Neutron Polarimetry with Polarized 3He for the NPDGamma Experiment

Matthew Martin Musgrave
University of Tennessee - Knoxville, mmusgrav@utk.edu

Recommended Citation

Musgrave, Matthew Martin, "Neutron Polarimetry with Polarized 3He for the NPDGamma Experiment. " PhD diss., University of Tennessee, 2014.
https://trace.tennessee.edu/utk_graddiss/2718

To the Graduate Council:

I am submitting herewith a dissertation written by Matthew Martin Musgrave entitled "Neutron Polarimetry with Polarized 3He for the NPDGamma Experiment." I have examined the final electronic copy of this dissertation for form and content and recommend that it be accepted in partial fulfillment of the requirements for the degree of Doctor of Philosophy, with a major in Physics.

Geoffrey Greene, Major Professor

We have read this dissertation and recommend its acceptance:

Robert Grzywacz, Thomas Papenbrock, Lawrence Heilbronn

Accepted for the Council:

Carolyn R. Hodges

Vice Provost and Dean of the Graduate School

(Original signatures are on file with official student records.)

Neutron Polarimetry with Polarized 3He for the NPDGamma Experiment

A Dissertation Presented for
the Doctor of Philosophy
Degree
The University of Tennessee, Knoxville

Matthew Martin Musgrave
May 2014

Acknowledgments

I would like to thank my advisor Geoff Greene for the support and guidance he has given me through the years. If not for him I would not have met all the wonderful people in the NPDGamma collaboration, and if not for his patience, I would not have been able to spend so much time with them.

I would like to thank all the people who helped me over the years including Kyle Grammer, Elise Martin, Zhaowen Tang, Chad Gillis, Nadia Fomin, and especially Serpil Kucuker who was always there during polarimetry, even when I couldn't be. I hope you enjoyed the cake.

I am deeply grateful to Seppo Penttila, David Bowman, and Vince Cianciolo for all the advice they have given me. Without any of you meetings would have been short and unhelpful.

I would like to thank the Instrument Development Group at the SNS for their help with ^{3}He cells and optical pumping. I would especially like to express my gratitude to Tony Tong for teaching me how to polarize ^{3}He and giving me freedom to work in his lab unsupervised, even though I'm sure it scared him.

For their work creating the models I used during my analysis, I would like to acknowledge Chris Crawford, David Bowman, and Kyle Grammer.

Abstract

Cold neutrons enable the study of the fundamental interactions of matter in low-energy, low-background experiments that complement the efforts of high-energy particle accelerators. Neutrons possess an intrinsic spin, and the polarization of a beam of neutrons defines the degree to which their spins are oriented in a given direction. The NPDGamma experiment uses a polarized beam of cold neutrons to make a high precision measurement, on the order of 10 ppb, of the parity-violating asymmetry in the angular distribution of emitted gamma-rays from the capture of polarized neutrons on protons. This asymmetry is a result of the hadronic weak interaction (HWI) and is directly proportional to the long-range, weak interaction modeled by the exchange of a pion between two nucleons. The results of the NPDGamma experiment are dependent on the polarization of the neutron beam used in the capture reaction. The neutron polarization is measured using the large spin-dependent neutron capture cross section of polarized helium-3 to a precision of less than 1%, which does not significantly increase the total error of the measured gamma-ray asymmetry. Reported here is a description of the NPDGamma experiment, the work done to polarize helium-3, and the results of the neutron beam polarimetry measurements.

Table of Contents

List of Tables

List of Figures

Chapter 1

Introduction

Neutrons possess many characteristics that make them ideal for high precision experiments that study the Standard Model [1]. They interact via all four of the fundamental forces (gravity, electromagnetism, strong interaction, and weak interaction) at a level that is accessible to experimentation. They have zero electric charge, which makes them less susceptible to interaction with matter and allows them to penetrate matter much better than electrically charged particles. Their relatively long lifetime means that while they are not commonly found unbound from a nucleus, they can be used in experiments and produced in large quantities at reactor and spallation sources.

Spin is an intrinsic angular moment possessed by particles such as the neutron, which has a spin of $\frac{1}{2}$. Neutrons have a magnetic moment oriented in the direction of the spin and can interact with magnetic fields. Since the neutron has no net charge, its magnetic moment is indicative of its composite structure of three charged quarks: one up and two down. When the magnetic moment of a neutron is measured in an external magnetic field, it is found to be oriented parallel or anti-parallel to the field. The total polarization of a neutron beam is defined as

$$P_n = \frac{N_\uparrow - N_\downarrow}{N_\uparrow + N_\downarrow} \tag{1.1}$$

where $N_\uparrow$ and $N_\downarrow$ are the number of neutrons measured with spins parallel and anti-parallel respectively to the external field.

The NPDGamma experiment uses polarized neutrons to study fundamental properties of the neutron and the weak interaction. The goal of the NPDGamma experiment is to measure the directional γ-ray asymmetry in the radiative capture of polarized cold neutrons on unpolarized protons in the reaction $\vec{n} + p \rightarrow d + \gamma$. The asymmetry results from the hadronic weak interaction (HWI) at low energy and gives an indication of the strength of the long-range weak interaction between nucleons.

In the $\vec{n} + p \rightarrow d + \gamma$ reaction, neutrons can capture via the strong interaction and emit γ-rays isotropically or via the weak interaction and emit γ-rays with a spatial dependence. The size of the γ-ray asymmetry is thus comparable to the strength of the weak interaction relative to the strong interaction. Two previous measurements of the γ-ray asymmetry in the $\vec{n} + p \rightarrow d + \gamma$ reaction [2, 3] have set an experimental limit on the γ-ray asymmetry at $A_\gamma \lesssim 2 \times 10^{-7}$. The inherent asymmetry of the experimental apparatus due to an individual detector position and efficiency is larger than the limit on the γ-ray asymmetry. Therefore, the emitted γ-rays are detected for both neutron spin states by periodically flipping the neutron spins 180°. Then the observed asymmetries of both neutron spin states are averaged to remove any systematic uncertainties uncorrelated with the neutron spin. The average probability of a transition between neutron spin states when the spins are flipped 180° is called the spin-flip efficiency ϵ_{sf}. The spin-flip efficiency results in a multiplicative change in the neutron polarization by a factor of 1-2ϵ_{sf}.

The observed γ-ray asymmetry $A_{\gamma,obs}$ measured in the NPDGamma experiment is dependent on the neutron polarization P_n and spin-flip efficiency ϵ_{sf}, and $A_{\gamma,obs}$ is related to the physical asymmetry $A_{\gamma,phys}$ by

$$A_{\gamma,obs} = \epsilon_{sf} P_n A_{\gamma,phys}. \tag{1.2}$$

It is therefore necessary to measure the neutron polarization P_n and the spin-flip efficiency ϵ_{sf} to a precision much better than the statistical uncertainty in the raw γ-ray asymmetry $A_{\gamma,obs}$, in order to deduce the physical asymmetry $A_{\gamma,phys}$ without substantially increasing the total uncertainty. The anticipated, ultimate statistical precision of the NPDGamma experiment is 1×10^{-8}. Based on previous limits, the asymmetry could potentially be as large as 2×10^{-7}. Thus an uncertainty of 1×10^{-8} requires the neutron polarization P_n and spin-flip efficiency ϵ_{sf} to be measured with an error less than 5%. The goal of the neutron polarimetry measurements is to measure the neutron polarization P_n and spin-flip efficiency ϵ_{sf} to within 2%. In fact, an accuracy of less than 1% was obtained.

Experiments with polarized neutron beams have used several methods for accurately measuring neutron polarization. Examples include utilizing the Stern-Gerlach effect [4] and a rotatable analyzing system consisting of two supermirror polarizers separated by a neutron spin flipper [5]. The large spin dependent capture cross section of polarized ^{3}He has also been suggested to measure the polarization of a polychromatic neutron beam [6]. For the NPDGamma experiment, a new method of measuring the polarization for a pulsed neutron source with polarized ^{3}He is used to determine the wavelength dependent neutron polarization. The ^{3}He is polarized by spin-exchange optical pumping (SEOP) [7–9]. Because it is not feasible to polarize the ^{3}He directly, lasers optically pump an alkali vapor and populate one spin state of the alkali atoms' valence electrons, which then collisionaly transfer their spin state to the ^{3}He nucleus by the hyperfine interaction. This method polarizes the ^{3}He in a compact glass cylinder called a ^{3}He cell that can be transported to the neutron beam with an insignificant amount of ^{3}He depolarization.

The theory of the Hadronic Weak Interaction is discussed in Chapter 2. The experimental apparatus for the NPDGamma experiment is described in Chapter 3. A detailed description of the polarization of ^{3}He by SEOP is discussed in Chapter 4. The method of measuring the neutron polarization and spin-flip efficiency and the results of those measurements are discussed in Chapter 5.

Chapter 2

Theory of Hadronic Weak Interaction

Basic interactions between elementary particles are described with the four fundamental forces: gravity, electromagnetism, strong interaction, and weak interaction. Hadrons, such as protons and neutrons, are composite particles made of quarks, and they are sensitive to all four of the fundamental forces. Their electromagnetic and strong interactions are well studied; however, experiments that study the weak interaction between hadrons have only recently become possible: enabling tests of current theories of HWI.

The first modern theory of the weak interaction, proposed by Enrico Fermi, explains β-decay as a four-fermion contact interaction [10]. Today the weak interaction is better understood with the electroweak theory developed by Sheldon Glashow, Steven Weinberg, and Abdus Salam in 1968, which predicted the existence of the $\mathrm{W}^{\pm}$ and Z^{0} bosons that mediate the weak force. However, the electroweak theory alone is not sufficient to describe HWI because it does not address contributions from the strong interaction caused by the constituent quarks. Additionally, the range of the $\mathrm{W}^{\pm}$ and Z^{0} bosons is too small to facilitate a direct weak interaction between two hadrons.

The first commonly accepted theory of HWI was the meson-exchange model proposed by Desplanques, Donaghue, and Holstein (DDH) [11] to explain the strangeness-conserving

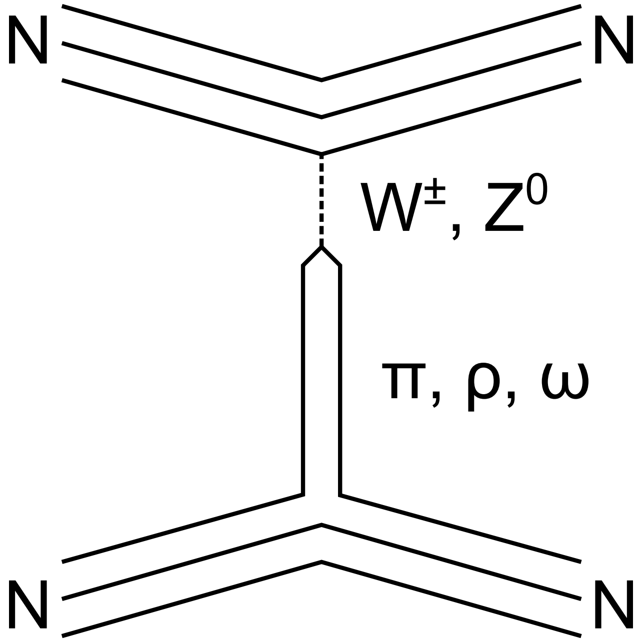

Figure 2.1: The weak nucleon-nucleon interaction.

$\Delta S = 0$ HWI. In this theory the low energy interaction between hadrons can be interpreted as the exchange of a meson, a quark-antiquark pair, and in the case of the HWI, the meson couples to one of the nucleons with a $W^{\pm}$ or Z^0 boson, as illustrated in Fig. 2.1.

2.1 The Meson Exchange Model

The strong force was first postulated to explain the bound nature of the atomic nucleus in spite of the electromagnetic repulsion of protons. The strong force acts on the quarks within hadrons by the exchange of gluons and confines protons and neutrons to a scale of ∼2 fm. At greater distances, the effect of the strong interaction quickly becomes insignificant. At low energies in the meson exchange model, the strong interaction between nucleons is mediated by the exchange of a virtual meson. The range of the virtual meson can be determined from the uncertainty relation, that energy conservation for the creation of a virtual particle can only be violated for a time $t = \hbar/mc^2$ that corresponds to a range of ∼ct. The lightest mesons are the pions, π^0, π^+, and π^-; the π^0 has a mass of 135 MeV/c^2, which results in a range of ~2 fm. In the meson exchange model, this is the cause of the negligible strength of the strong interaction outside of the nucleus such that the Coulomb repulsion of the protons becomes the more dominant nuclear force. At distances less than ~0.8 fm, there is a repulsive force between nucleons that can be understood as a consequence of the Pauli exclusion principle, which prohibits identical nucleons or quarks (in the case of a neutron-proton pair) from occupying the same state. For low energies, where strangeness is conserved $\Delta S = 0$, the three lightest mesons (π, ρ, and ω) are the carriers of the strong interaction.

The weak interaction is mediated by the exchange of virtual W$^\pm$ and Z^0 bosons. The masses of W$^\pm$ are 80 GeV/c^2 and Z^0 is 91 GeV/c^2. These large masses result in the weak interaction having a range of $\sim 2\times10^{-3}$ fm, which is significantly less than the separation between nucleons. Thus for the weak interaction between nucleons, a light meson is emitted from one nucleon, traverses the nucleon separation to within the range of the weak interaction, and then couples to the second nucleon by a W$^\pm$ or Z^0 boson, as shown in Fig. 2.1. The probability of an exchange of a W$^\pm$ or Z^0 boson at one vertex is proportional to the weak coupling constant, which is $\sim 10^{-6}$-10^{-7} compared to the strong coupling constant of ~1. Moreover, the probability of a direct exchange of a W$^\pm$ or Z^0 boson is proportional to the weak coupling constant to second order; a purely weak interaction is therefore never experimentally observed. The short range of the weak gauge bosons means that in the meson exchange model the weak interaction vertex can be approximated as a point-like four-quark interaction. For DDH's model of the HWI, observables are formulated in terms of six weak meson-nucleon coupling constants: $h^1_\pi, h^0_\rho, h^1_\rho, h^2_\rho, h^0_\omega, h^1_\omega$. The superscript denotes the change of the isospin in the HWI, where isospin is a conserved quantity in the strong interaction which follows the same mathematics as spin.

2.2 Parity Violation in the Weak Interaction

Parity is the symmetry operation that changes the sign of all spacial coordinates: $\hat{P}f(x,y,z) \rightarrow f(-x,-y,-z)$. In three dimensions a parity transformation is analogous to a mirror reflection modulo a rotation. When parity is conserved, there is no distinction between the results of an experiment and a mirror reflection of the experiment, but a parity-violating transformation would be sensitive to the "handedness" of the experiment. Polar vectors, such as position $\vec{r}$, change sign under parity, but even functions of polar vectors, such as scalars $\vec{r}\cdot\vec{p}$ and axial vectors $\vec{r}\times\vec{p}$, do not.

In 1956, the weak interaction was predicted to violate parity by Lee and Yang [12], and the following year, parity violation was observed in the β-decay of polarized ^{60}Co nuclei [13]. It is now known that within the context of the Standard Model, the weak force violates parity maximally, and it is believed to be the only force that violates parity. Therefore, experiments that search for a parity violating observable, such as NPDGamma, are a method of studying the weak interaction.

2.3 The NPDGamma Asymmetry

For the reaction $\vec{n} + p \rightarrow d + \gamma$, an HWI observable is the parity violating directional γ-ray asymmetry illustrated in Fig. 2.2. The emitted γ-rays have an angular distribution dependent on the angle θ between the neutron spin and the γ-ray momentum such that

$$\frac{d\sigma}{d\Omega} \propto 1 + A_\gamma \cos\theta \tag{2.1}$$

where A_γ is the γ-ray asymmetry. The deuteron is a loosely bound nucleus, so the interaction is dominated by the exchange of the longest range meson, the pion. DDH estimated the γ-ray

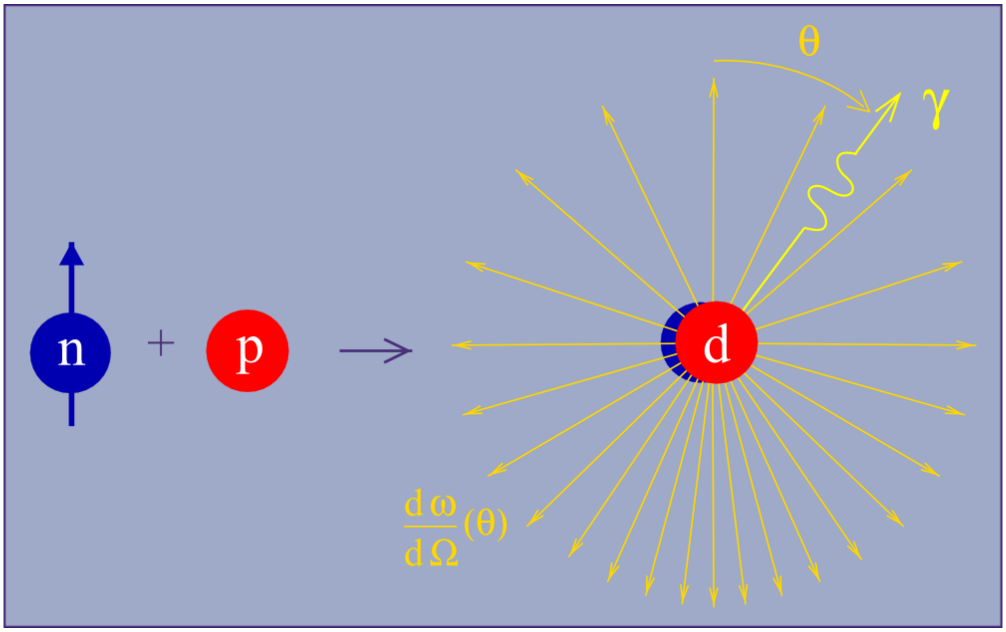

Figure 2.2: The γ-ray asymmetry from polarized neutron capture on protons. Figure courtesy of C. Gillis.

asymmetry, in terms of the weak meson-nucleon coupling constants, to be

$$A_\gamma = -0.107h_\pi^1 - 0.001h_\rho^1 + 0.004h_\omega^1. \tag{2.2}$$

This calculation confirms the γ-ray asymmetry in the $\vec{n}+p \rightarrow d+\gamma$ reaction to be dependent almost exclusively on the weak pion-nucleon coupling constant h_π^1. Neutral, spinless mesons cannot contribute to parity violation because of Barton's theorem [14], so the exchanged pions must be either π^+ or π^-. Furthermore, the weak interaction is mediated by a Z^0 boson because weak charged current that changes the isospin by $\Delta I = 1$, which is the case for the h_π^1 coupling constant, is suppressed by the Cabibbo angle [15]. The γ-ray asymmetry measurement therefore isolates the weak neutral current.

DDH gives an estimated best value of $h_\pi^1 \approx 4.56\times10^{-7}$ and a reasonable range of $0-11.4\times10^{-7}$. The h_π^1 coupling constant and the asymmetry are small because the interaction between the neutron and proton in the reaction $\vec{n}+p \rightarrow d+\gamma$ is dominated by the strong interaction, which conserves parity. The DDH "best value" suggests an asymmetry of $A_\gamma = -0.5 \times 10^{-7}$.

The meson-exchange model does not work as well at higher energies because it approximates nucleons as pointlike particles, when they are actually composite particles of quarks and gluons. This has motivated the creation of a model-independent theory of the HWI using effective field theory [16]. The low-energy limit of the effective field theory approach has six unknown coupling constants, one of which is from pion exchange and is proportional to the h_π^1 coupling constant. More recently, direct calculations of the HWI from the standard model have been performed using lattice QCD. The first calculation of the weak pion-nucleon coupling constant on the lattice found $h_\pi^1 = [1.099 \pm 0.505] \times 10^{-7}$ using a pion mass of 389 MeV/c^2 [17].

Several experiments have attempted to determine the weak pion-nucleon coupling constant h_π^1. A measurement of the γ-ray asymmetry in the $\vec{n} + p \rightarrow d + \gamma$ reaction in 1977 gave a null result with $A_\gamma = [-0.6 \pm 2.1] \times 10^{-7}$ [2]. In 1985 measurements of the circular polarization of the gamma rays emitted from a parity-mixed doublet of ^{18}F gave $h_\pi^1 < 1.2 \times 10^{-7}$ [18], which is much lower that the DDH-predicted best value. A 1997 measurement of the anapole moment of ^{133}Cs yielded a larger than expected h_π^1 [19]. The last run of the NPDGamma experiment at the Los Alamos Neutron Science Center (LANSCE) produced a null result with $A_\gamma = [-1.2 \pm 2.1(stat.) \pm 0.2(sys.)] \times 10^{-7}$ [3]. Results of current research leave some ambiguity to the size of the h_π^1 coupling constant, and this has motivated new high-precision measurements of the HWI in few-body systems. In the NPDGamma experiment, measuring the $\vec{n} + p \rightarrow d + \gamma$ reaction has an advantage over experiments that use nuclei, as there are no nuclear structure uncertainties in the γ-ray asymmetry, and the γ-ray asymmetry isolates the h_π^1 coupling constant.

Chapter 3

The NPDGamma Experiment

The NPDGamma experiment is installed on the Fundamental Neutron Physics Beamline (FNPB), beamline 13, at the Spallation Neutron Source (SNS) at Oak Ridge National Laboratory. A schematic of the experiment is shown in Fig. 3.1, and a conceptual model of the experiment in Fig. 3.2. The neutrons are transported to the experiment by a neutron guide with a pair of choppers that select the desired neutron energies. The neutron beam is polarized by a multichannel supermirror polarizer that reflects neutrons with an efficiency dependent on the neutron spin state. To maintain the neutron polarization, the entire experiment downstream of the supermirror polarizer is inside of a uniform magnetic field of $\sim$9.4 Gauss. The neutron spins can be flipped 180° by a radio frequency spin flipper (RFSF) so γ-rays can be measured for both neutron spin states. The neutron beam is then incident on a 16 L liquid para-hydrogen, where each hydrogen nuclei that captures a neutron emits a 2.2 MeV γ-ray. The 2.2 MeV γ-rays are detected by an array of 48 CsI(Tl) detectors that cover a solid angle of $\sim 3\pi$ around the para-hydrogen target. Neutron monitors detect the neutron beam intensity at various locations in the experiment. The signals from the neutron monitors and CsI(Tl) detectors, as well as the current to the RFSF, are recorded by the data acquisition system.

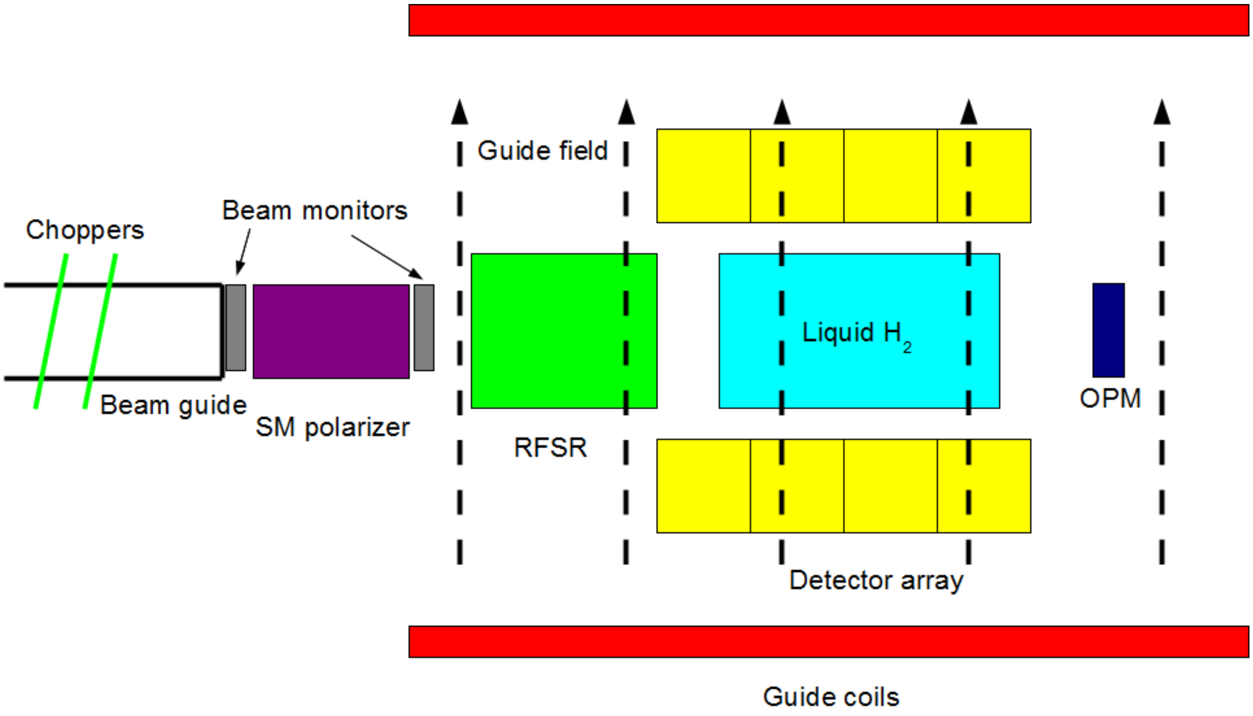

Figure 3.1: Schematic of the NPDGamma experiment. Figure courtesy of the NPDGamma collaboration.

3.1 Spallation Neutron Source

The SNS is a neutron science facility for condensed matter and fundamental neutron physics research [20, 21]. The SNS provides a high-intensity 60 Hz pulsed cold neutron beam used by the NPDGamma experiment and several condensed matter instruments. With the pulsed neutron beam, the neutron energy is characterized by the neutron time-of-flight.

The production of neutrons at the SNS starts with negatively charged hydrogen ions H^- created at an ion source, which are injected into a 331 m linear accelerator, or linac, consisting of an initial room-temperature section, followed by a superconducting section. The linac is designed to accelerate the H^- ions to a kinetic energy of $\sim$1.0 GeV. At the end of the linac, the H^- ions enter a high energy beam transfer line that injects the beam into the accumulator ring. The electrons are removed from the H^- ions by a diamond stripper

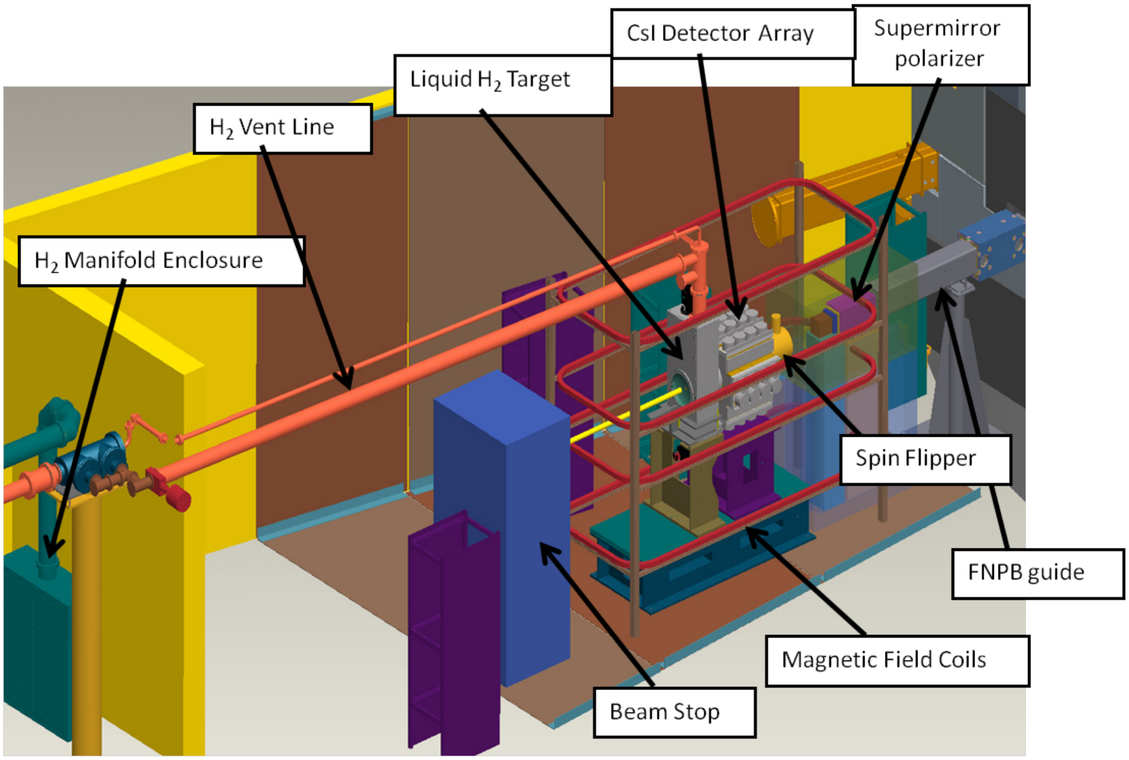

Figure 3.2: A conceptual model of the NPDGamma experimental setup. Figure courtesy of the NPDGamma collaboration.

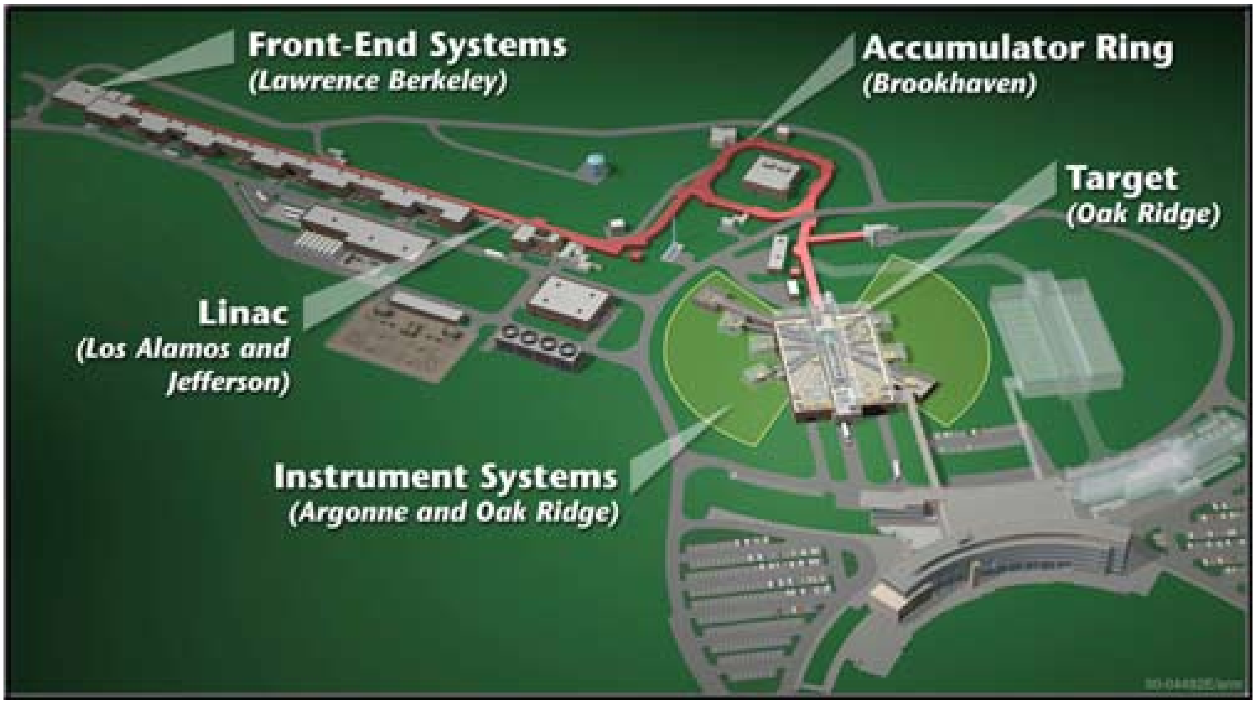

Figure 3.3: The SNS facility at Oak Ridge National Laboratory. Figure courtesy of the SNS.

foil [22] at the injection site into the accumulator ring. The accumulator ring is 248 m in circumference, and the protons revolve at a frequency of 1.058 MHz. The protons are released from the accumulator ring in pulses at a rate of 60 Hz and strike a liquid mercury target with a pulse length of $\sim$695 ns. The SNS's full design power is 1.4 MW, which at a proton kinetic energy of 1.0 GeV means 1.5×10^{14} protons per pulse. Each proton incident on the mercury target produces 20 to 30 neutrons by a combination of spallation and thermal evaporation. The statistical uncertainty of the NPDGamma experiment is dependent on the total neutron flux over the course of the experiment, and the large neutron production rate of the SNS enables a 1×10^{-8} measurement to be made. For the majority of the NPDGamma experiment, the SNS beam power was between 800 kW and 850 kW.

The neutrons produced have energies varying from nearly zero to the incident proton energy of 1.0 GeV. The neutrons lose energy by scattering off iron and beryllium reflectors

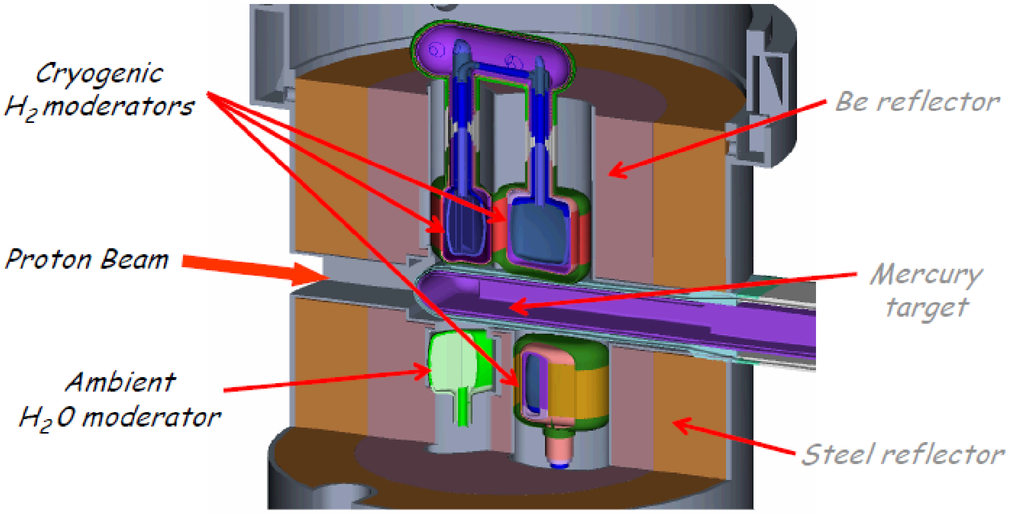

Figure 3.4: The mercury target and neutron moderators at the SNS. Figure courtesy of the SNS.

and are cooled to nearly thermal equilibrium in four moderators that are coupled with the mercury target. A schematic of the SNS target vessel is displayed in Fig. 3.4. FNPB views a liquid hydrogen moderator at 20 K. Neutrons are thermalized in the moderator over a span of ∼100 μs, which is long compared to the proton pulse length of 695 ns, but short compared to the neutron's flight time to the experiment of ∼10 ms. The time scale of neutron thermalization enables the neutron energies of the pulsed beam to be determined from time-of-flight measurements.

3.2 Fundamental Neutron Physics Beamline

The FNPB is made of several 1 to 2 m long sections of neutron guide that have a rectangular cross section with a width of 10 cm and a height of 12 cm. The neutron guide begins 1 m downstream of the moderator and ends 15.3 m downstream of the moderator at the supermirror polarizer. From 4.3 m to 7.5 m, the neutron guide is curved to eliminate a direct line of sight to the moderator. The rest of the guide consists of straight sections [23].

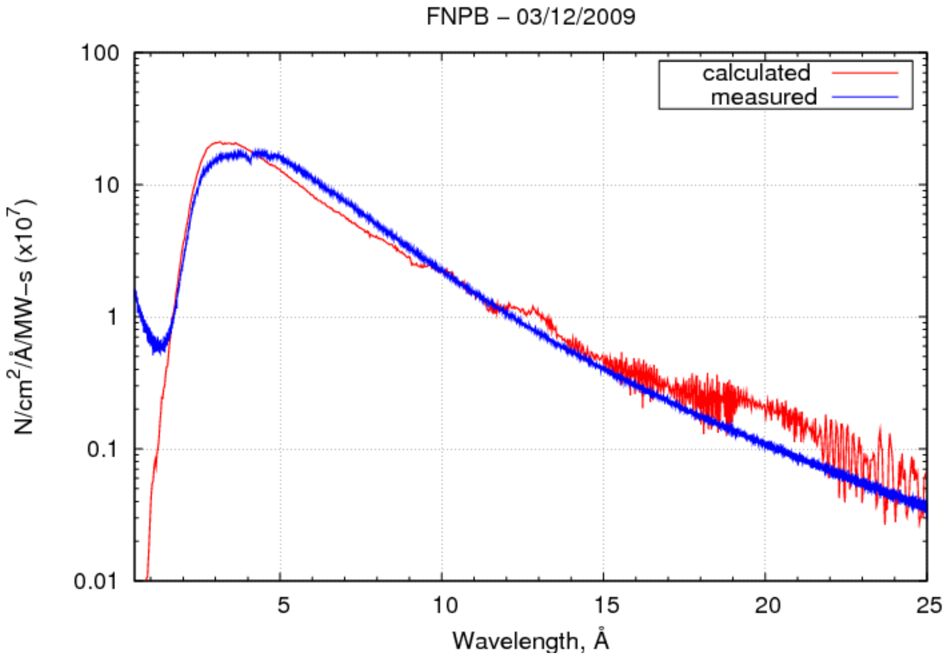

Figure 3.5: The neutron flux at the end of the FNPB. The calculated neutron flux utilizes a model of the moderated source neutrons that does not include the high energy (low wavelength) prompt neutrons measured on the FNPB. Figure courtesy of the NPDGamma collaboration.

The neutron flux measured at the end of the beamline before the supermirror polarizer is shown in Fig. 3.5 with a calculation of the expected neutron flux.

The FNPB is shielded in concrete to reduce the radiation levels in the SNS instrument hall to safe levels. There are also two shutters that can block the neutron beam when the experiment is not running or when access to the experimental cave is necessary. The primary shutter is located in the mercury spallation target shielding, and the secondary shutter is 10.5 m downstream of the moderator where it does not have a direct line of sight to the moderator. The shutters contain a section of neutron guide that is moved into the beamline when the shutters are opened.

3.2.1 Neutron Guide

The reflectivity of the neutron guide is caused by the scattering of the neutrons off the surface material due to the wave nature of neutrons. The cold neutron beam can be treated as a plane wave incident on the guide surface, which is composed of many scattering potentials. For cold neutrons with wavelengths of a few Angstroms, the range of the scattering potential of a nucleus is ∼5 orders of magnitude less than the neutron wavelength. The scattering amplitude $f(\theta)$ is the amplitude of the outgoing spherical wave relative to the incoming plane wave, such that

$$\Psi(\vec{r}) = e^{ikz} + \frac{f(\theta)}{r} e^{i\vec{k}\cdot\vec{r}}. \tag{3.1}$$

For low energies, the scattering amplitude $f(\theta)$ is approximately equal to the scattering length from which the scattering cross section can be determined. The scattering is pure s-wave, which does not have an angular dependence. For many randomly distributed point-like scatterers, the interference among all of these spherical waves gives rise to a net potential known as the "Fermi pseudopotential" [24]

$$V_F\left(\vec{r}\right) = \frac{2\pi\hbar^2}{m} b\delta^3\left(\vec{r}\right) \tag{3.2}$$

where m is the neutron mass, b is the neutron scattering length, and $\delta^3\left(\vec{r}\right)$ is the Dirac delta function. The Fourier transform of the many point-like, hard scatterers in the Fermi pseudopotential is a constant negative potential well that accurately describes low energy neutron scattering because the many point-like scatterers and the negative potential well have the same solution to the Schrodinger equation. The Fermi pseudopotential is valid when the wavelength is much greater than the range of the potential.

The nuclear scattering potential off a Ni surface calculated from the Fermi pseudopotential for the collection of Ni nuclear scattering potentials is

$$V_{nuc}\left(\vec{r}\right) = \frac{2\pi\hbar^2}{m} bN \tag{3.3}$$

where N is the number density of the Ni nuclei. The index of refraction for neutrons is given by the scattering potential and kinetic energy of the neutron by

$$n\left(\vec{r}\right) = \sqrt{1 - \frac{V\left(\vec{r}\right)}{E}} = \sqrt{1 - \frac{bN\lambda^2}{\pi}}, \tag{3.4}$$

and neutrons are reflected if the neutron kinetic energy normal to the surface is less than the potential barrier of the mirror material, $E_\perp < V$. The kinetic energy normal to the surface is equal to

$$E_\perp = \frac{1}{2} m v_\perp^2 = \frac{2\pi^2\hbar^2 \sin\theta}{m\lambda^2} \tag{3.5}$$

where θ is the angle between the neutron momentum and the surface. The critical angle θ_c is the neutron incident angle where $E_\perp = V_{nuc}$ and neutrons are totally reflected, and the critical angle is equal to

$$\theta_c = \sin^{-1}\left(\sqrt{\frac{bN\lambda^2}{\pi}}\right). \tag{3.6}$$

The performance of a neutron mirror can be improved by utilizing Bragg diffraction, where neutrons satisfying the Bragg relation,

$$n\lambda = 2d\sin\theta, \tag{3.7}$$

interfere constructively and reflect off a periodic lattice. A periodic, two-dimensional structure is produced by depositing uniform layers of a material with an index of refraction less than one alternating with another material with an index of refraction equal to one,

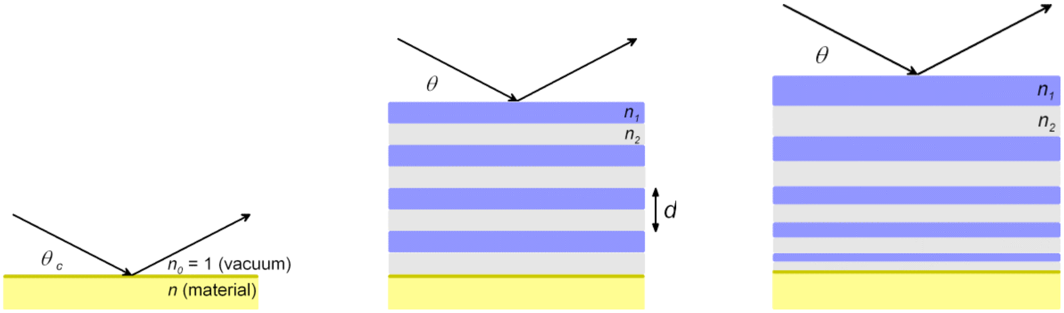

(a) single mirror **(b)** multilayer **(c)** supermirror

Figure 3.6: Neutron mirrors with various layer structures. The multilayer design enables Bragg scattering of one neutron wavelength, and the supermirror enables Bragg scattering of a range of neutron wavelengths. Figure courtesy of T. Chupp.

so that it matches the index of refraction of vacuum. The alternating layers need to have an equal optical thickness d, so the physical thickness that is deposited is adjusted for the indexes of refraction of the layer materials. This multilayer mirror, illustrated in Fig.3.6b, reflects neutrons like an artificial crystal lattice [25] and will improve the reflectivity of a simply neutron mirror for one neutron wavelength.

By varying the thickness of the layers, the Bragg relation will be satisfied for several wavelengths creating a supermirror [26], as illustrated in Fig.3.6c, that has a critical angle greater than that of a single-layer neutron mirror. A multilayer supermirror is characterized by its m-value, $m = \frac{\theta_{mirror}}{\theta_{Ni}}$, where θ_{mirror} is the critical angle of the supermirror and θ_{Ni} is the critical angle of a single layer Ni mirror Fig.3.6a. A graphical representation of the reflectivity of neutrons versus the m-value is shown in Fig. 3.7.

The performance of a supermirror is better when the thinner layers are evaporated onto the substrate first. Firstly, the absorption of neutrons with a smaller incident angle, which the thicker layers reflect, is greater for a fixed mirror depth, so they should be near the surface. Secondly, it is more important that the thinnest layers be more uniform, and this is more easily accomplished closer to the substrate [27]. In practice, the best performance is achieved by randomizing the layer thickness to some degree, rather than merely increasing them

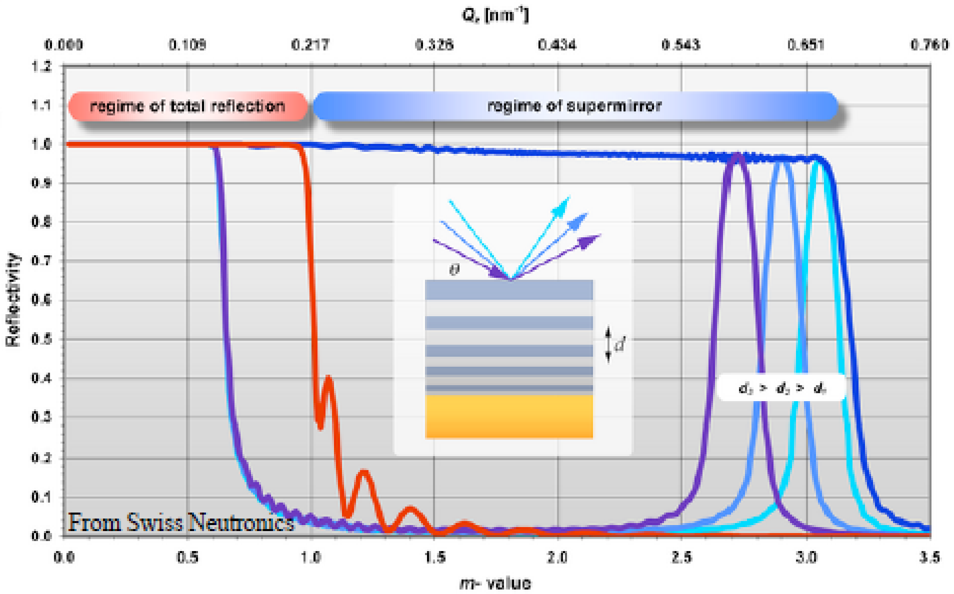

Figure 3.7: The reflectivity of neutrons plotted versus neutron energy and neutron mirror m-value. The red curve represents the reflectivity of a Ni mirror, characterized by a maximum m-value of 1.0. The violet, light blue, and cyan curves represent the reflectivity of neutron mirrors with layers of uniform thickness, which Bragg scatter neutrons at a specific energy determined by the layer thickness. The blue curve represents the reflectivity of a supermirror with a m-value of 3.0. Figure courtesy of Swiss Neutronics.

incrementally. While uniform layers would increase the reflectivity at the Bragg condition, the reflected neutrons would have a narrow linewidth. The random layers broaden the linewidth of the reflected neutron wavelengths, increasing the total proportion of reflected neutrons.

3.2.2 Choppers

Beamline 13 has two neutron choppers located 5.5 m and 7.5 m downstream of the moderator [28]. The choppers are disks with wedges cut out for specific angular cross sections and a radii of ∼0.3 m. The chopper disks are coated with ^{10}B to absorb neutrons of undesired wavelengths, and they rotate at 60 Hz on low friction magnetic bearings in a vacuum of ∼35 microns of Hg. The angular opening of the first chopper is 132°, of the second 167°. The openings of the choppers coincide with the beamline after a specific time offset relative to the timing of the SNS's proton pulses. The angular openings and time offset are chosen to minimize the presence of neutrons from earlier pulses entering the NPDGamma experimental apparatus. The chopping of the frame-overlap neutrons is necessary because they are not uniformly flipped by the RFSF and they reduce the energy resolution of the neutron beam.

3.3 Beam Monitors

Two neutrons monitors are installed upstream and downstream of the supermirror polarizer, referred to as M1 and M2 respectively. They are used to determine the stability of the neutron beam flux during the experiment so that an asymmetry is not measured because of skipped accelerator pulses or nonlinearities in the neutron beam flux. The voltage signals detected in M1 from 5,000 neutron pulses are plotted in Fig. 3.8. The spread in the beam monitor signals correspond to fluctuations in the proton beam power, which is directly proportional to the neutron beam flux.

Both neutron monitors are multi-wire proportional chambers that create current signals proportional to the incident neutron flux. An illustration of their conceptual design is shown in Fig. 3.9. The chambers are made of aluminum with 1 mm thick windows. Inside the monitors are three sets of wires positioned in parallel planes. The outer planes are HV wires at $\sim$1000V, powered by a battery that is enclosed in a Coulomb shield to reduce electromagnetic interference; the inner signal wires are connected to a low noise preamplifier read by the DAQ. The wires are spaced 0.5" apart and are soldered to a PEEK (poly ether ether ketone) plastic frame. The PEEK frame keeps the HV and signal wires electrically isolated from the aluminum chamber. The monitors are grounded and electrically isolated from the beamline.

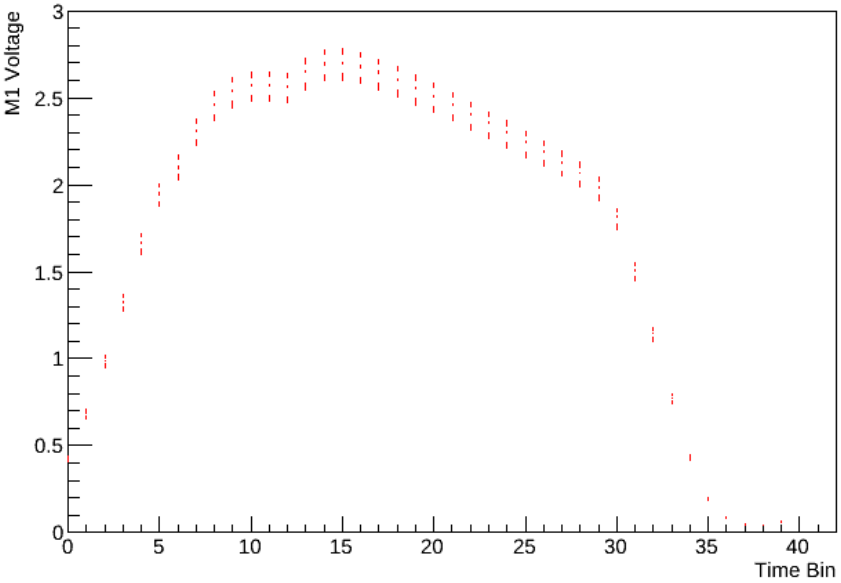

Figure 3.8: Beam monitor M1 voltage signals from 5,000 neutron pulses simultaneously plotted across 40 time bins.

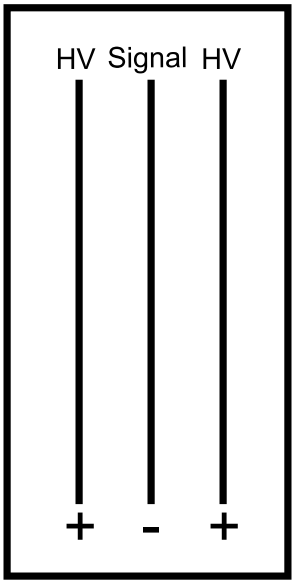

Figure 3.9: Schematic of a multi-wire proportional chamber.

Both monitors are filled with 10-15 Torr of ^{3}He and ~750 Torr of N_2. The neutrons capture on ^{3}He in the monitor and form a triton and proton by the reaction $^3He + n \rightarrow p +^3 H+$ 764 keV. The triton and the proton ionize the nitrogen gas and produce electrons and N^+ ions. The N^+ ions drift towards the HV wires; the electrons drift towards the signal wires and produce a current proportional to the captured neutron flux. The monitors have an active area between the two HV electrodes, in which electrons are repulsed by the HV wires and captured on the signal wires. The area between the HV electrodes and the chamber walls is a dead space that does not produce a signal from ionized N_2.

The transmission through M1 was tested at the High Flux Isotope Reactor at Oak Ridge National Laboratory on beamline HB-D2, a monochromatic beamline with 4.5 meV neutrons. The transmission through M1 is 0.957±0.5% for 4.5 meV neutrons; the transmission loss is caused by a combination of scattering and capture on the aluminum windows and the ^{3}He fill gas [29]. M2 is expected to have a comparable neutron transmission. These reductions in the neutron flux are within expectable limits for the experiment.

In addition to beam monitors M1 and M2, there is a beam monitor, referred to as M4, after the para-hydrogen target. M4 is used to determine to ratio of para- to ortho-hydrogen in the target and for neutron polarimetry measurements. M4 is a ^{3}He filled proportional chamber, similar to M1 and M2, and it also produces a current signal proportional to the incident neutron flux. However, since neutron capture in M4 does not need to be minimized, M4 is a thick neutron monitor with a ^{3}He density of 0.91 amagat [30], and it contains parallel plate electrodes as opposed to the parallel planes of wires in M1 and M2.

The current signals from the beam monitors are averaged into 40 time bins for each neutron pulse, and since the neutron beam is pulsed at 60 Hz, the 40 time bins span 16.67 ms of neutron transmission data. The neutron wavelengths corresponding to each time bin depend on the beam monitors' distance from the neutron moderator, and thus they differ for each monitor.

3.4 Super Mirror Polarizer

The neutron beam is spin filtered by a supermirror polarizer, which is a supermirror coated in alternating layers of a ferromagnetic and a nonmagnetic material. The supermirror polarizer operates in a magnetic field that saturates the magnetization of the ferromagnetic material so that the index of refraction of the magnetized layer for one neutron spin state is approximately equal to the index of refraction of the nonmagnetic layer. Thus one spin state sees a uniform index of refraction, and the other sees a periodic structure resembling a crystal lattice and reflects because the Bragg condition is met [26, 27, 31]. The index of refractions of the supermirror polarizer materials are determined from the sum of the nuclear and magnetic scattering potentials such that

$$n\left(\vec{r}\right) = \sqrt{1 - \frac{V_{nuc}\left(\vec{r}\right) \pm \vec{\mu}\cdot\vec{B}}{E}}, \tag{3.8}$$

and the sign of the magnetic scattering potential is determined from the neutron spin direction. The supermirror polarizer only spin filters neutrons that reflect via Bragg diffraction. Neutrons with an incident angle less than the critical angle (Eq. 3.6) for a Ni surface are reflected for both spin states.

The supermirror polarizer consists of 45 channels of uniformly spaced, curved supermirror panes. A supermirror coating is evaporated onto both sides of a thin borosilicate glass substrate to make each supermirror pane; the double-sided coating increasings the neutron transmission compared to a one-sided coating by improving the angle of acceptance. Because the angular divergences from each channel overlap, the neutron polarization varies with the position of the transmitted neutron beam, and the experiment is positioned to optimized the incident average neutron polarization.

The supermirror polarizer is 40 cm long and has a radius of curvature of 14.8 m [32]. The boron in the glass substrates absorbs the neutrons of the undesired spin state when they scatter through the supermirror panes. The supermirror polarizer is inside a 350 Gauss magnetic field created by permanent magnets to saturate the magnetization of the ferromagnetic Ni layers in the supermirror polarizer and create the spin dependent refractive index in the ferromagnetic layer.

Gradients in the portion of the magnetic field outside the supermirror polarizer can cause Stern-Gerlach steering of the polarized neutrons, so the entire supermirror polarizer apparatus is placed in a compensation magnet that adiabatically reduces that portion of the magnetic field to ∼9.4 Gauss, in order to reduce the field gradients experienced by the neutrons as they move from the supermirror polarizer to the guide field containing the rest of the experimental apparatus. The magnetic fields from both the supermirror polarizer and the compensation magnet appear as approximately equal and opposite dipole magnetic fields, so they both disappear much faster than $\frac{1}{r^3}$ with the distance from the supermirror polarizer.

3.5 Magnetic Guide Field

A magnetic guide field maintains the polarization of the neutrons as they travel from the supermirror polarizer to the parahydrogen target. The guide field is created by four rectangular coils depicted in Fig.3.2. The strength of the magnetic field is tuned periodically during the commissioning and running of the experiment, in order to optimize the efficiency of the RFSF by matching the Larmor frequency associated with the guide field to the fixed resonance frequency of the RFSF; the optimal magnetic field was found to be about 9.4 Gauss. The magnetic field is tuned by adjusting the current from a Danfysik power supply, which supplies about 23 Amps of current to 18 windings in the two middle coils and 39 windings in the top and bottom coils. There are 12 auxiliary windings in each of the four coils, powered by 3.3 Amps from a BK Precision power supply. The second power supply, with coils of a different windings ratio, allows fine adjustment of the ratio of current through the middle and outer sets of coils. The walls, floor, and ceiling of the experimental cave are lined with low carbon steel to shield the experiment from extraneous magnetic fields and to improve the guide field uniformity by creating a flux return for the guide field. The guide coils also contain shim coils to reduce field non-uniformities within the experiment in the transverse directions [33]. Two flux gate magnetometers are mounted above and below the RFSF to monitor the field.

3.5.1 Stern-Gerlach Steering

The neutron magnetic moment has been measured at -1.91μ_N, where μ_N is the nuclear magneton [34]. In an inhomogeneous magnetic field, the neutron's magnetic moment causes it to experience a force given by

$$\vec{F} = -\vec{\mu} \cdot \nabla \vec{B}. \tag{3.9}$$

The direction of the force changes with the neutron magnetic moment when it is flipped by the RFSF, so deflection caused by field gradients in the vertical direction $\hat{y}$ between the RFSF and the center of the parahydrogen target creates a false asymmetry. The vertical deflection of a neutron for a uniform gradient can be determined from the force on the magnetic moment and the time of flight after being flipped by the RFSF, d/v, where d is the distance from the RFSF center to the detector center. Since the NPDGamma experiment is measuring an asymmetry in the $\hat{y}$ direction and the neutrons are traveling in the $\hat{z}$ direction, the NPDGamma experiment is only sensitive to the $\frac{\partial B_y}{\partial z}$ component of the gradient, which can be calculated from

$$\Delta y = \frac{1}{2} a t^2 = \frac{-1}{2m_n} \left(\mu \frac{\partial B_y}{\partial z} \right) \left(\frac{d}{v} \right)^2 . \tag{3.10}$$

The false asymmetry is calculated as a function of the vertical deflection and the distance from target center to detector array y, by

$$A_{false} = \frac{\Omega_{up} - \Omega_{down}}{\Omega_{up} + \Omega_{down}} = \frac{2\Delta y}{y}. \tag{3.11}$$

If a false asymmetry of less than 10^{-9} is desired, the geometry of the experiment constrains the allowable field gradient. Using conservative estimates of the dimensions, d=0.75 m and y=0.25 m, and a neutron velocity of v=565 m/s, an allowable limit on the magnetic field gradient in the vertical direction is 2.5 mG/cm.

3.5.2 Detector and Field Alignment

There is a parity-allowed left-right asymmetry with a magnitude of $|A_{lr}| < 5.3 \times 10^{-7}$ that can mix with the parity-violating up-down asymmetry if the detector is misaligned with the magnetic field $A_{false} = A_{lr} \sin(\theta)$, or if there is a large horizontal component to the magnetic field $A_{false} = A_{lr} \frac{|B_x|}{|B_y|}$. If a false asymmetry of less than 10^{-9} is desired, the angle of misalignment must be less than 2 mrad and $|B_x| < 0.02$ Gauss.

3.5.3 Model of the Guide Field

The magnetic field inside of the supermirror polarizer and the guide coils is calculated in TOSCA, an analysis package for the electromagnetic design analysis and simulation software OPERA [35]. The magnetic field was calculated in a grid of points separated by 0.5 cm. The magnetic field calculated in TOSCA is used to calculated the depolarization of the neutron beam from the exit of the supermirror polarizer to 1.9 m downstream of the supermirror polarizer. The results are plotted in Fig. 3.10. The depolarization of the neutron beam due to magnetic field gradients is negligible for the NPDGamma experiment [36].

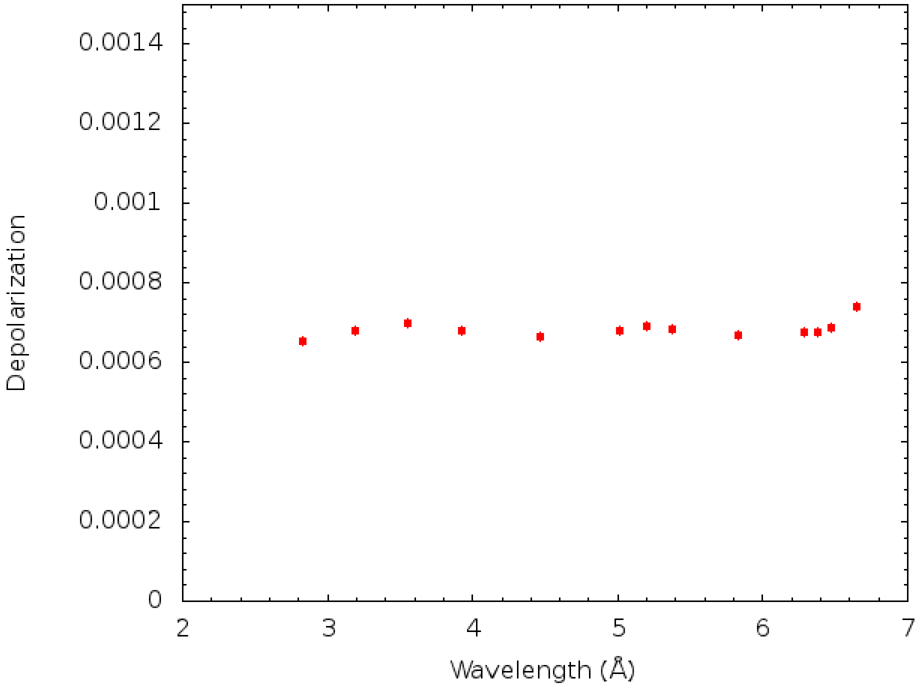

Figure 3.10: The average depolarization of the neutrons from the exit of the supermirror polarizer to 1.9 m downstream of the center of the supermirror polarizer.

3.6 RF Spin Flipper

The precision required for the NPDGamma experiment is not achievable by measuring the γ-ray asymmetry from the capture of only one neutron spin direction with two opposing detectors because the positions and gains of the detectors and the alignment of the neutron beam cannot be adjusted to the precision necessary to make a 10^{-8} measurement. This challenge is solved by measuring the γ-ray asymmetry for opposing neutron spin directions, so that the asymmetry inherent in the experimental apparatus can be removed by averaging the γ-ray asymmetry for each spin direction. Flipping the neutron's spin with the RFSF also reduces the effects of several systematic errors including fluctuations in the neutron beam's intensity and the time varying efficiencies of the detectors caused by temperature changes and crystal activation.

The NPDGamma experiment uses a resonant RF spin flipper (RFSF) [37] to flip the spins of the neutrons by 180°. The magnetic field inside the RFSF is the sum of two orthogonal fields. First, there is a static magnetic field $\vec{B}_0$ created by the guide coils, to which the neutron spins are initially parallel when they enter the RFSF. Second, there is an RF magnetic field $\vec{B}_{RF} = B_{RF}\cos(\omega_R F t)\hat{z}$ created by the RFSF that is parallel to the neutron guide and on resonance. The resonance condition is met when the frequency of the RF magnetic field ω_{RF} is equal to the Larmor frequency of the neutrons in the guide field $\omega_0 = \gamma_n B_0$. The oscillating field can be interpreted as the sum of two counter-rotating fields of equal magnitude, with one rotating at the Larmor frequency and the other far off resonance such that

$$\vec{B}_{RF} = \vec{B}^{+}_{RF} + \vec{B}^{-}_{RF} \tag{3.12}$$

$$\vec{B}_{RF} = \frac{B_{RF}}{2}(\cos(\omega t)\hat{z} + \sin(\omega t)\hat{x}) + \frac{B_{RF}}{2}(\cos(\omega t)\hat{z} - \sin(\omega t)\hat{x}). \tag{3.13}$$

The counter-rotating field is off resonance by twice the Larmor frequency and has a negligible effect on the neutron spin. At resonance in the rotating reference frame of the neutron magnetic moment, the constant guide field disappears and the component of the RF field rotating with the the neutron magnetic moment appears constant. While the neutron is in the RFSF, the magnetic moment of the neutron precesses about the rotating field $\vec{B}^{+}_{RF}$ with a frequency of $\omega_1 = \gamma_n B^{+}_{RF}$. If we define the constant $a = \sqrt{(\omega_0 - \omega_{RF})^2 + \omega_1^2}$, the probability of a transition between neutron spin states (defined as the spin-flip efficiency) is dependent on the resonant condition and the time spent in the RFSF t_{sf} such that

$$\epsilon_{sf} = \frac{\omega_1^2}{a^2}\sin^2\left(\frac{a t_{sf}}{2}\right). \tag{3.14}$$

The RFSF is a quantum mechanical device, but this classical interpretation is valid because its result is equivalent to the expectation value of the quantum description of the

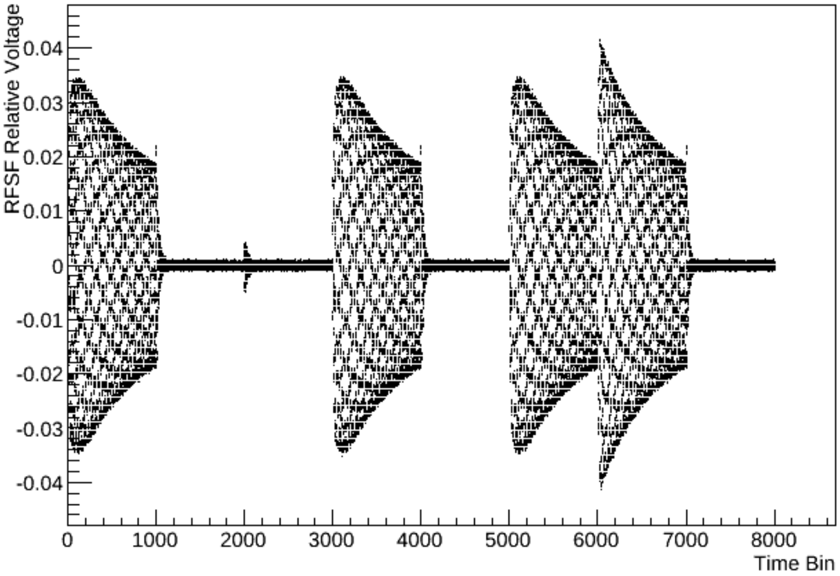

Figure 3.11: The current to the RFSF is measured with a small wire coil by measuring the induced voltage when the driving current passes through the coil. The voltage signal from the coil is plotted for eight beam pulses and shows the eight step spin-sequence (↑↓↓↑↓↑↑↓) used with the RFSF.

RFSF. A quantum mechanical description of the RFSF used by the NPDGamma experiment is published by P. Seo [37], and a quantum mechanical derivation of the resonance condition of a Rabi coil is available in [38].

The angle of rotation of the neutron spin is dependent on the magnitude of the RF field B_{RF} and the time-of-flight through the RFSF t_{sf}. The physical size of the RFSF is fixed, so the time t_{sf} is dependent on the velocity of the neutron, which is characterized by its time-of-flight from the moderator t_{tof}. The RF field amplitude varies as a function of t_{tof} such that $B_{RF} \propto \frac{1}{t_{tof}}$, as shown in Fig. 3.11, so that all neutrons that pass through the RFSF are rotated by 180°.

The RFSF is a 30 cm long solenoid with a radius of 15 cm made of 18 gauge copper wire. The solenoid is inside an aluminum cylinder whose eddy currents shield the RF field and minimize the magnetic field gradients outside of the RFSF. The neutron spins are flipped with the sequence of spin reversal ↑↓↓↑↓↑↑↓ to control linear and quadratic systematic effects. The RFSF efficiency was measured with polarized ^{3}He as part of the polarimetry measurements, and the results are discussed in Sec. 5.3.

3.7 Para-Hydrogen Target

A 16 L liquid para-hydrogen target cooled to ∼17 K is used for the capture of polarized neutrons on protons [39]. A diagram of the para-hydrogen target is shown in Fig. 3.12. When a neutron captures on a proton in the reaction $\vec{n} + p \rightarrow d + \gamma$, they form a deuteron in an excited state that emits a 2.2 MeV γ-ray. Measuring the spatial distribution of these emitted γ-rays is how the NPDGamma experiment determines the parity-violating asymmetry caused by the hadronic weak interaction.

In addition to being captured, neutrons can also scatter off protons coherently, which conserves the neutron spin, or incoherently, which allows spin exchange. Incoherent scattering of the neutrons leads to the depolarization of the neutron beam; therefore, it needs to be minimized. The hydrogen molecule has two spin isomers: para-hydrogen and ortho-hydrogen. In para-hydrogen, the ground state, the proton spins are anti-aligned, which causes the molecular energy of para-hydrogen to be 15 meV less than ortho-hydrogen where the proton spins are aligned. Ortho-hydrogen has a large spin-incoherent cross section for neutron scattering, so its presence in the target quickly depolarizes the neutron beam. However, neutrons with energies less than 15 meV cannot scatter incoherently with para-hydrogen because they do not have enough energy to convert para- to ortho-hydrogen; therefore, only coherent scattering can occur. The neutrons used in the NPDGamma experiment are slow neutrons with energies of ∼5 meV, and the target is para-hydrogen at 17 K, so the polarization of the neutron beam is maintained when the neutrons scatter

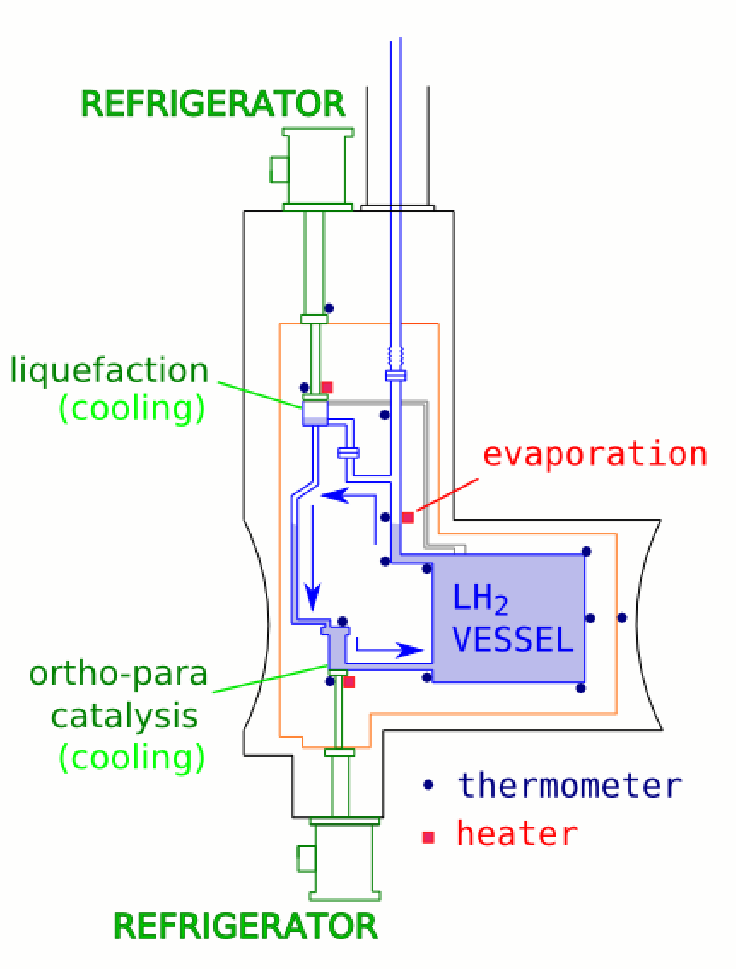

Figure 3.12: The para-hydrogen target contains 16 L of liquid hydrogen in an Al vessel. The liquid hydrogen is cooled by a pair of refrigeration units attached to the liquefaction chamber and the ortho-para converter. Figure courtesy of C. Gillis.

and capture in the target.

At 17 K the equilibrium concentration of para-hydrogen is expected to be 99.96%. The equilibrium concentration is achieved by circulating the liquid hydrogen through an iron-oxide ortho-para converter [40], which increases the rate of conversion of ortho- to para-hydrogen to the equilibrium value. The iron-oxide works well as a converter because it has very large field gradients localized around the individual ferromagnetic grains. Neutron depolarization in the para-hydrogen target is expected to be below 2%.

The mean-free path λ for 4 meV neutrons in liquid para-hydrogen is about 9 cm, and the average number of collisions before capture is about 2.5. This is calculated from $N = \sigma_s/\sigma_c$ where σ_s is the scattering cross section and σ_c is the capture cross section. A rough estimate of the mean distance before capture, ignoring the angular dependence of the scattering and energy transfer, is approximately $\lambda\sqrt{N}$ $\approx$13 cm. By designing a cylindrical target with a length about twice the mean capture distance, and a radius equal to the mean capture distance, about 60% of the neutron beam is expected to be absorbed in the para-hydrogen target.

The target is cooled with three mechanical refrigerators that couple to the target with copper cold heads. The cold heads are located at the fill line, the liquefaction chamber, and the ortho-para converter. Electrical heaters are also coupled to the target at these locations, to provide finer control of the temperature of the target. The target is shielded with lithium flouride to reduce background from neutrons scattered out of the target and into the CsI(Tl) detectors. There is a 1.75 cm diameter opening in the ^{6}Li shielding behind the target to allow the neutron beam to exit the target so that the conversion to para-hydrogen can be monitored and the neutron polarization can be measured with the target installed.

3.8 Other Capture Targets

In addition to para-hydrogen, several other neutron capture targets are placed inside of the CsI(Tl) detector array to measure the emitted γ-rays, including carbon tetrachloride (CCl_4), aluminum, boron carbide (B_4C), and water. Neutron capture on CCl_4 has a large parity-violating γ-ray distribution previously measured to be $[-29.1 \pm 6.7] \times 10^{-6}$ [41] and $[-21.2 \pm 1.7] \times 10^{-6}$ [42]. The γ-ray asymmetry from capture on CCl_4 can be measured in a few hours on the FNPB, and correctly measuring the asymmetry provides a confirmation that the experimental apparatus is operating properly. When collecting data on the para-hydrogen asymmetry, the largest source of background comes from the capture of neutrons on aluminum, so the aluminum γ-ray asymmetry is measured on an aluminum target to an uncertainty consistent with the uncertainty of the para-hydrogen γ-ray asymmetry measurement. A B_4C plate is placed inside the detector with the full cross section of the neutron beam incident on it; boron is a strong neutron absorber and will capture essentially the entire neutron beam, so the B_4C target provides a measurement of the total neutron flux. Water is used as a target during commissioning of the experiment to provide an estimate of the signal size from the para-hydrogen target since the signal from water is mostly from neutron capture on hydrogen.

3.9 CsI(Tl) Detector Array

The emitted γ-rays from the capture targets are detected by an array of 48 CsI(Tl) detectors [43]. Two CsI(Tl) crystals are paired in a cube shaped detector with a vacuum photo-diode to detect the scintillation light. Vacuum photo-diodes are used because the magnetic guide field would affect the gain of a photo-multiplier tube. These detectors are arranged in 4 rings with 12 detectors each surrounding the para-hydrogen target, as illustrated in Fig. 3.13. The γ-ray asymmetry could in principle be measured by a single detector aligned with the neutron polarization, by measuring the number of γ-rays detected for the two neutron spin states. By using an array of detectors, spatial and angular resolution can be determined and a larger cross section of emitted γ-rays can be detected. Together the 48 detectors cover a solid angle of about 3π. The error in the γ-ray asymmetry as well as the spatial resolution improves slowly by using a greater number of smaller detectors. Thus a detector size is chosen that balances the benefit of increased resolution and the disadvantage of increased noise caused by γ-ray energy being shared between detectors. The detectors are cubes with sides of 15.2 cm. These dimensions were chosen because the mean free path of 2.2 MeV γ-rays in CsI is about 5.5 cm. With these dimensions each crystal absorbs 84% of the γ-rays incident on them.

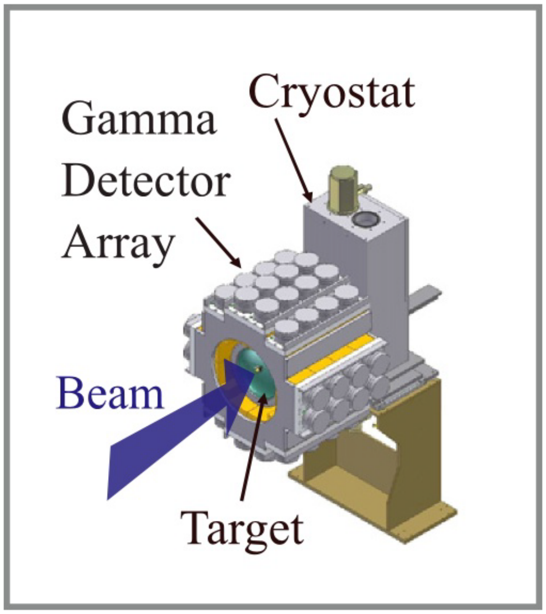

Figure 3.13: The detector array consists of 48 CsI(Tl) detectors arranged in 4 rings around the target vessel, covering a solid angle of about 3π. Figure courtesy of the NPDGamma collaboration.

The properties of CsI(Tl) and its use as a scintillation material are well documented [44]. The γ-rays interact with matter through photo-electric absorption, Compton scattering, and pair production. In photo-electric absorption, a γ-ray is absorbed by an atom, which then ejects an electron. Since the binding energy of the electron is several orders of magnitude less than the kinetic energy of the γ-ray, the electron's kinetic energy is approximately equal to the energy of the γ-ray. The emitted electron then scatters through the material, exciting atoms that then decays by emitting photons. In Compton scattering, the γ-ray scatters off several electrons instead of being absorbed. The γ-ray transfers a portion of its energy to each electron, which are ejected from their atoms. These emitted electrons scatter through the material and excite atoms just like the electrons emitted by photo-electric absorption. Compton scattering is the primary method of energy transfer from the γ-rays to the CsI(Tl) crystals in the NPDGamma experiment. Pair production can occur because the 2.2 MeV γ-rays are energetically allowed to form a positron-electron pair that annihilates itself, forming two 0.511 MeV γ-rays. These γ-rays then transfer the rest of their energy to the CsI(Tl) crystal through photo-electric absorption and Compton scattering. The time for an energetic γ-ray or electron to scatter through the CsI(Tl) crystal and excite various atoms in the crystal is significantly shorter then the decay time of the excited atoms, which is on the order of 1 μs. This means that all of the excited atoms are essentially formed at the same time and decay at the same time, creating a burst of visible photons with a spread proportional to the excited atoms' half-life.

The scintillation light from the CsI(Tl) crystals is converted into current signals by vacuum photo-diodes, and the current signals are converted into voltages and amplified by low-noise solid state preamplifiers. Counting statistics appear as shot noise in the signal detected from the vacuum photo-diode, because of the finite number of γ-rays incident on the CsI(Tl) detectors. The precision of the γ-ray asymmetry measurement is dependent on counting statistics, so it is important that electronic noise be negligible compared to shot noise. The vacuum photo-diodes and preamplifiers are chosen to make the signal gain uniform and the electronic noise minimal. The current signals from the CsI(Tl) detectors are averaged into 40 time bins containing 16.67 ms of data by the data acquisition system, and they are recorded in groups of eight beam pulses corresponding to the eight step spin sequence of the RFSF.

Chapter 4

Polarized 3He Cells

^{3}He is an isotope of helium with only one neutron that has several useful properties for studying neutrons. ^{3}He has a very large spin-dependent neutron capture cross section in the reaction $^3He + n \rightarrow p + {}^3H$. Neutrons usually capture on ^{3}He into an excited state of ^{4}He that decays strongly into a triton and proton, instead of radiatively into the ground state of ^{4}He, because it is energetically allowed and the probability of decay couples to the strength of the associated force [45]. The large capture cross section and the spin dependence mean that polarized ^{3}He can be used to selectively capture one neutron spin state. Moreover, it is possible to polarize ^{3}He gas with spin exchange optical pumping (SEOP) by polarizing an alkali vapor with a pumping laser and then transferring the spin state of the alkali atoms' valence electrons to the ^{3}He nuclei by the hyperfine interaction. By utilizing these properties, glass cells filled with ^{3}He can be polarized and transported to a beamline where they can either be used as neutron polarizers or analyzers to determine the neutron polarization. Other useful characteristics of polarized ^{3}He cells are that they can be built to have an area large enough to encompass a neutron beam, that the process of neutron capture on ^{3}He does not produce gamma rays, and that the polarization of ^{3}He can be maintained in a magnetic field for several hours or continuously if polarized *in situ*.

4.1 Neutron Transmission Through 3He

For a beam of neutrons transmitted through a differentially-thin volume of ^{3}He, the ratio of the neutrons captured on ^{3}He to the initial neutron transmission is equal to the ratio of the cross section of all the ^{3}He nuclei in the volume $N\sigma$ to the total cross sectional area of the neutron beam A. The differential change in the neutron transmission is equal to the negative of the number of captured neutrons. With this information, a differential equation for the neutron transmission through ^{3}He can be obtained:

$$\frac{dT}{T} = \frac{-N\sigma}{A}. \tag{4.1}$$

After making the substitutions $Adx = dV$ and $n_- = \frac{N_-}{dV}$, the equation reduces to

$$\frac{dT}{T} = -n\sigma dx, \tag{4.2}$$

which can be integrated from 0 to l, where l is the length of the ^{3}He cell, arriving at

$$T = T_0 e^{-n\sigma l}, \tag{4.3}$$

where T_0 is the initial neutron intensity. This is the equation for the neutron transmission through an unpolarized ^{3}He cell.

The neutron capture cross section of ^{3}He is proportional to the neutron wavelength because of the $\frac{1}{v}$ dependence of the capture cross section at low energies, and so the neutron transmission through an unpolarized ^{3}He cell can be determined at any neutron wavelength from a known cross section at a reference wavelength, such that

$$T(\lambda) = T_0(\lambda) e^{-\chi\lambda}, \tag{4.4}$$

where the value χ, henceforth called the ^{3}He thickness, is defined here as

$$\chi = \frac{n\sigma_0 l}{\lambda_0}, \tag{4.5}$$

with the corresponding reference values $\sigma_0 = 5316$ bn and $\lambda_0 = 1.798$ Å [46]. The ^{3}He thickness χ is a value intrinsic to the ^{3}He cell, and it will be useful for discussion of the transmission of a pulsed neutron beam.

The neutron transmission through a polarized ^{3}He cell can be determined by solving for the transmission of each neutron spin state separately and then summing them. The large spin dependence in the capture cross section means that the capture into the triplet state is negligible, and for these calculations the capture cross sections for the singlet and triplet states are $\sigma_- = 2\sigma$ and $\sigma_+ = 0$ respectively. The differential change in the number of spin up neutrons transmitted through polarized ^{3}He dT_+, normalized to the total number of spin up neutrons T_+, is equal to the number of spin down ^{3}He nuclei N_- multiplied by the capture cross section of spin up neutrons on spin down ^{3}He nuclei σ_- normalized to the total area of transmission A

$$\frac{dT_+}{T_+} = \frac{-N_-\sigma_-}{A}. \tag{4.6}$$

By making the substitutions $\sigma_- = 2\sigma$, $Adx = dV$, and $n_- = \frac{N_-}{dV}$, the equation reduces to

$$\frac{dT_+}{T_+} = -2n_-\sigma dx, \tag{4.7}$$

and can be integrated from 0 to l to obtain,

$$T_+ = T_{+,0}e^{-2n_-\sigma l}. \tag{4.8}$$

The ^{3}He polarization is defined by $P_{He} = \frac{n_+ - n_-}{n_+ + n_-}$. It can be shown that this implies $1 - P_{He} =$

$\frac{2n_-}{n}$, where $n = n_+ + n_-$, which can be substituted into the equation for the transmission of spin up neutrons, so that

$$T_+ = T_{+,0} e^{-n\sigma l(1-P_{He})}. \tag{4.9}$$

Using the same procedure, the transmitted spin down neutron flux is

$$T_- = T_{-,0} e^{-n\sigma l(1+P_{He})}. \tag{4.10}$$

For an unpolarized neutron beam, $T_{+,0} = T_{-,0} = \frac{1}{2}T_0$. The total transmission of an unpolarized neutron beam through polarized ^{3}He can be calculated from the sum of the transmissions of the two neutron spin states:

$$T = T_+ + T_- \tag{4.11}$$

$$T = \frac{1}{2}T_0 e^{-n\sigma l(1-P_{He})} + \frac{1}{2}T_0 e^{-n\sigma l(1+P_{He})} \tag{4.12}$$

$$T = T_0 e^{-n\sigma l} \cosh(n\sigma l P_{He}). \tag{4.13}$$

Using the ^{3}He thickness χ, the transmission expressed as a function of neutron wavelength is

$$T(\lambda) = T_0(\lambda) e^{-\chi\lambda} \cosh(\chi\lambda P_{He}). \tag{4.14}$$

The transmission of a neutron beam with a polarization of P_n through polarized ^{3}He can be calculated from Eqs. 4.9 and 4.10 by making the neutron polarization implicit in the initial transmission coefficients, so that

$$T_+ = T_0 \frac{1+P_n}{2} e^{-n\sigma l(1-P_{He})} \tag{4.15}$$

$$T_- = T_0 \frac{1-P_n}{2} e^{-n\sigma l(1+P_{He})}. \tag{4.16}$$

The total transmission of a polarized neutron beam through polarized ^{3}He is the sum of the transmission of these two spin states:

$$T = T_+ + T_- \tag{4.17}$$

$$T = T_0 \frac{1+P_n}{2} e^{-n\sigma l(1-P_{He})} + T_0 \frac{1-P_n}{2} e^{-n\sigma l(1+P_{He})} \tag{4.18}$$

$$T = T_0 e^{-n\sigma l} \cosh(n\sigma l P_{He}) \left[1 + P_n \tanh(n\sigma l P_{He})\right], \tag{4.19}$$

and the transmission as a function of neutron wavelength is

$$T(\lambda) = T_0(\lambda) e^{-\chi\lambda} \cosh(\chi P_{He}\lambda) \left[1 + P_n \tanh(\chi P_{He}\lambda)\right]. \tag{4.20}$$

If $P_n = 0$, the transmission of an unpolarized neutron beam from Eqs. 4.13 and 4.14 is returned. Moreover, by setting $P_{He} = 0$, the transmission through unpolarized ^{3}He is found to be independent of the neutron polarization.

4.2 Fabrication and Filling

^{3}He cells are made out of GE180 aluminosilicate glass. GE180 glass's chemical composition is tabulated in Tab. 4.1. GE180 glass is used because it is a "hard" glass through which ^{3}He atoms are slow to diffuse. One explanation for why GE180 glass cells have a longer spin relaxation lifetime than cells made with a diffusive glass is that ^{3}He is likely to spend more time within the lattice of a diffusive glass, and polarized ^{3}He will depolarize because of interactions within the glass. Another benefit of GE180 glass is the absence of Boron, which is a strong neutron absorber. The cell is cleaned with soap and deionized water and then rinsed with acetone, ethanol, and methanol in that order. The cell is then attached to the filling station, where it is evacuated to less than 10^{-8} Torr with a turbo pump, while it is being baked at 400 °C for at least five days. This pumping and baking procedure removes contaminates such as oxygen, which is paramagnetic and can limit the maximum ^{3}He polarization. A diagram of the ^{3}He filling station is shown in Fig. 4.1.

Table 4.1: The composition of GE180 glass.

Compound	Percentage
SiO_2	60.3%
BaO	18.2%
Al_2O_3	14.3%
CaO	6.5%
SrO	0.25%

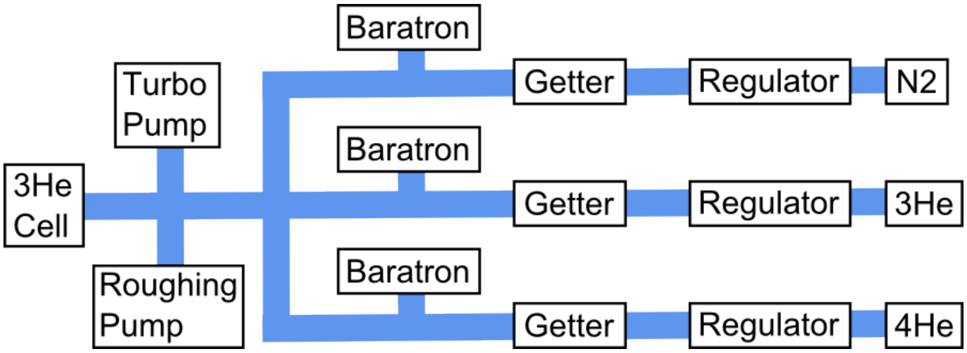

Figure 4.1: The ^{3}He cell filling station.

Small amounts of the alkali metals Rb and K, occupying a negligible fraction of the cell volume, are added to the cell to facilitate spin exchange optical pumping. Reservoirs of Rb and K attached to the glass cell manifold are also evacuated, but they are kept at room temperature while the cell is baking. After the cell has been evacuated and baked for several days, the Rb and K are driven into the cell by flame distillation with a propane torch. Equal partial pressures of Rb and K are desired during optical pumping, but they have different vapor pressures, so the cell needs to be filled with a ratio of approximately one part Rb to 25 parts K. Raoult's Law gives an approximation of the total vapor pressure of a mixture of liquids as the sum of the individual vapor pressures p_i weighted by the mole-fraction of each component χ_i

$$p_{tot} = \sum_i p_i \chi_i. \tag{4.21}$$

The appropriate Rb to K ratio is determined by heating the cell to ∼100 °C and measuring the absorption spectra of fluorescent light with a photodiode. The transition between the ground state and the first excited states of the alkali atoms corresponds to two photon wavelengths called the D1 and D2 wavelengths, which in spite of their names are not associated with the D orbital. These two wavelengths correspond to the fine splitting of the P orbital of the valence electron of the alkali atoms. The D1 and D2 wavelengths of Rb are 795 nm and 780 nm, and of K 770 nm and 767 nm. These absorption lines can be seen in Fig. 4.2. The nuclear spin causes hyperfine splitting of these wavelengths, but the hyperfine splitting is small compared to the linewidths of the lasers used to polarize the alkali.

After baking, the cell is filled with N_2 and ^{3}He to partial pressures of about 0.1 bar N_2 and 1 bar ^{3}He. The filling manifold is continuously baked and pumped, and the N_2 and ^{3}He gases are passed through a set of getters to prevent impurities from entering the ^{3}He cell. The cell is then tipped off with a propane torch while immersed in liquid N_2. The liquid N_2 cools the cell to ∼70 K in order to lower the pressure inside to below atmospheric pressure, so that the pressure difference will cause the molten glass to collapse and seal the ^{3}He cell. After tip off, the closed ^{3}He cell is an isolated system, which can be polarized for use at the neutron beamline. The process of tipping off the cell results in a ^{3}He pressure different from the pressure measured during filling at room temperature. However, the ^{3}He pressure and thus density can be determined with neutron transmission measurements, which is done in Sec. 5.5.1.

Figure 4.2: D1 (770 nm) and D2 (767 nm) absorption lines of K, and the D2 (780 nm) absorption line of Rb.

4.3 Spin Exchange Optical Pumping

^{3}He is polarized with spin-exchange optical pumping (SEOP) by polarizing an alkali vapor with circularly polarized laser light and then letting the alkali polarize the ^{3}He through hyperfine interactions [7–9, 47]. During SEOP the ^{3}He cell is heated to between 190-200 °C to increase the vapor pressure of the alkali, and circularly polarized light at the D1 resonance of Rb, 795 nm, or K, 770 nm, is incident on the alkali vapor. The process of polarizing the alkali atoms is illustrated in Fig.4.3. The two substates in the $S_{1/2}$ orbital are given by $m_s = \pm\frac{1}{2}$. Circularly polarized light with a magnetic projection of +1 can only be absorbed by the $m_s = -\frac{1}{2}$ substate. This absorption excites the alkali atom to the $P_{1/2}$ orbital with $m_s = +\frac{1}{2}$. The excited state decays to either $S_{1/2}$ substate, but since the $S_{1/2}$, $m_s = -\frac{1}{2}$ substate is continuously being excited, the vaporized alkali atoms eventually become polarized in the $S_{1/2}$, $m_s = +\frac{1}{2}$ substate. During SEOP, if only Rb or K is being

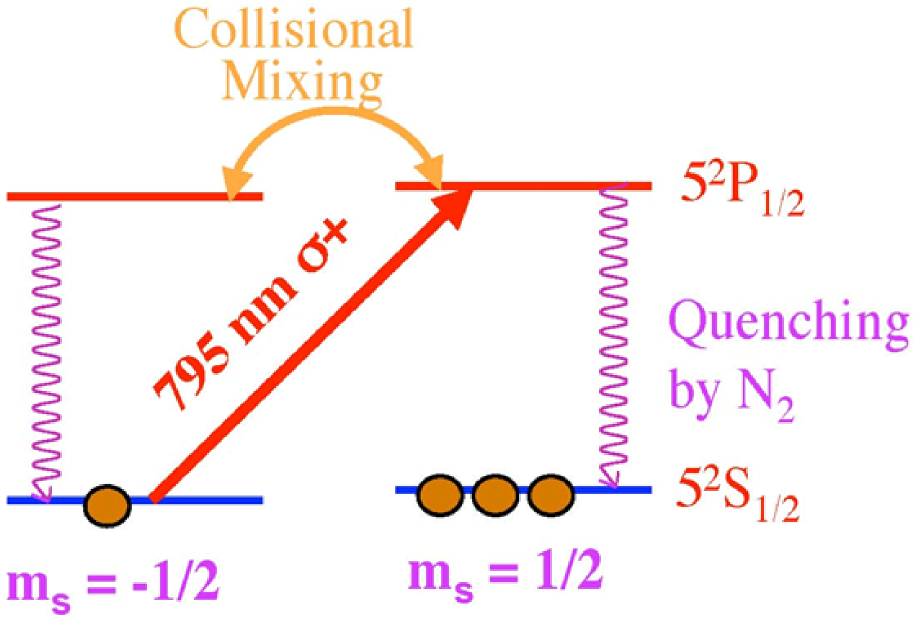

Figure 4.3: During spin exchange optical pumping, circularly polarized light is absorbed by one magnetic substate into an excited state that decays by quenching with N_2 into both substates states, polarizing the alkali vapor. Figure courtesy of NIST.

optically pumped at its D1 resonance, then the other will become polarized through spin-exchange collisions via the fine interaction. The rate of spin exchange between Rb and K is much faster than spin exchange with ^{3}He, so the alkali polarization will stay saturated as the ^{3}He polarizes.

The N_2 in the ^{3}He cell serves two important functions. Collisions between N_2 and Rb or K in the $P_{1/2}$ excited state mixes the two $P_{1/2}$ substates so that the decay rates to each magnetic substate of the $S_{1/2}$ ground state are equal, increasing the maximum polarization of the alkali atoms. Otherwise, there is a higher relative decay rate to the $S_{1/2}$, $m_s = -\frac{1}{2}$ substate equal to that decay path's Clebsch-Gordan coefficient of $\frac{2}{3}$. Moreover, radiative decay from the $P_{1/2}$ state can lead to radiation trapping, which limits the ability to optically pump the alkali vapor. When Rb or K in the $P_{1/2}$ excited state radiatively decay, they scatter unpolarized photons into the vapor at their D1 resonance wavelengths. This unpolarized light has a short scattering length, so it becomes trapped in the alkali vapor and depolarizes the alkali. A modest pressure of N_2 in the ^{3}He cell causes most of the excited alkali to nonradiatively decay via atomic collisions with N_2.

The ^{3}He nuclei are polarized by the hyperfine interaction during spin-exchange collisions with the valence electrons of Rb and K atoms. The spin-exchange rate γ_{SE} is

$$\gamma_{SE} = \langle \sigma_{SE} \nu \rangle [A], \tag{4.22}$$

where $\langle \sigma_{SE} \nu \rangle$ is the velocity-averaged rate constant and [A] is the alkali number density, and the ^{3}He polarization during pumping is

$$P_{He} = \frac{\gamma_{SE} P_A}{\gamma_{SE} + \Gamma} \left(1 - e^{-(\gamma_{SE} + \Lambda)t} \right), \tag{4.23}$$

where P_A is the alkali vapor polarization, and Γ is the relaxation rate of the ^{3}He polarization without contributions from collisions with the alkali vapor [8]. The ^{3}He polarization is maximized when $P_A \approx 1$ and $\gamma_{SE} \gg \Gamma$. Eq. 4.23 shows that the ^{3}He polarization is proportional to the alkali polarization, which can be improved by maximizing the laser polarization, reducing the laser divergence to minimize skew light [48], and increasing the laser power. The relaxation rate Γ mainly depends on spin-lattice relaxation from interactions of the ^{3}He with the cell walls; the lifetime of a polarized ^{3}He cell is maximized through the cell fabrication process described in Sec. 4.2. The rate of polarizing ^{3}He and thus the maximum attainable ^{3}He polarization can be increased by increasing the partial pressure of the alkali vapor, which can be done by raising the ^{3}He cell temperature during SEOP; however, this would also increase the optical thickness of the alkali vapor and would necessitate a corresponding increase in the laser power to polarize the alkali within the full volume of the ^{3}He cell [49]. The choice of alkali also affects the spin-exchange rate; the partial pressure of Rb is greater than the partial pressure of K at the same temperature, and at typical operating conditions, the probability of spin exchange is ∼2% for Rb$-^3$He collisions and ∼23% for K$-^3$He collisions. The ^{3}He polarization can be optimized with a hybrid cell that benefits from the properties of both Rb and K.

The polarization time constant for the alkali vapor is on the order of a few milliseconds, while that for ^{3}He is on the order of 1 to 10 hours. Depolarization of the alkali due to spin exchange with ^{3}He is thus negligible, and the alkali polarization stays nearly saturated as long as it is being optically pumped. Once optical pumping stops, the alkali vapor depolarizes rapidly by spin exchange collisions between the alkali atoms. Allowing the cell to cool and the alkali vapor to condense before stopping the optical pumping reduces the ^{3}He polarization loss from collisions with the depolarized alkali vapor.

4.4 NMR with Polarized 3He

In a static magnetic field $\vec{B}$, the energy levels of a spin $\frac{1}{2}$ particle lose their degeneracy, and the splitting of the energy levels associated with the different spin states is given by

$$\Delta E = 2\mu B, \tag{4.24}$$

where μ is the magnetic moment of the spin $\frac{1}{2}$ particle. Nuclear transitions between these states can be induced with electromagnetic radiation at a resonance frequency typically in the RF range for fields produced in a laboratory. The absorption and associated response of nuclei to radiation at the resonance frequency is known as Nuclear Magnetic Resonance (NMR).

The magnetization $\vec{M}$ of a system of nuclei in a static magnetic field $\vec{B}$ has a thermodynamic equilibrium value that is parallel to the field and related to the system's temperature T and the field $\vec{B}$ by its Boltzmann factor, such that

$$M \propto e^{\mu B_{\perp}/kT}. \tag{4.25}$$

This is the equilibrium longitudinal magnetization. A transverse magnetization will precess around the $\vec{B}$ field at the Larmor frequency such that the average equilibrium transverse magnetization in a static magnetic field is zero. The magnetization of a non-equilibrium system of nuclei in a magnetic field decays to its thermodynamic equilibrium magnetization in the longitudinal direction and to zero in the transverse direction. This decay of the magnetization is known as spin relaxation. The thermodynamic equilibrium magnetization of ^{3}He and alkali vapor is negligible in the range of magnetic field strengths and temperatures used for SEOP.

Three NMR techniques are used both to characterize the polarized ^{3}He cell and manipulate the ^{3}He polarization during optical pumping. These NMR techniques are free induction decay (FID), adiabatic fast passage (AFP), and electron paramagnetic resonance (EPR).

4.4.1 Spin Relaxation

After the ^{3}He has been polarized within its magnetic holding field, the ^{3}He is in a non-equilibrium state. Over time the magnetization of the ^{3}He decays exponentially to its equilibrium state. The decay of the longitudinal magnetization corresponds to a transition between energy levels, and the rate of spontaneous transition between spins states is very slow, with a time constant of $\sim 10^{20}$ s; consequently, this relaxation is usually mediated by the exchange of energy and angular momentum with other degrees of freedom referred to as the lattice, a terminology taken from condensed matter physics. Hence, the longitudinal relaxation of the magnetization is often called the spin-lattice relaxation, and its relaxation time is designated T_1. For polarized ^{3}He cells, these other degrees of freedom include the alkali vapor, the glass wall of the cell, and gradients of the magnetic field in the longitudinal direction. The relation between T_1 and magnetic field gradients is expressed by

$$\frac{1}{T_1} \propto \frac{|\nabla B_x|^2 + |\nabla B_y|^2}{B_0^2}, \tag{4.26}$$

where ∇B_x and ∇B_y are magnetic field gradients in the longitudinal directions and B_0 is the magnitude of the total magnetic field [47]. When a polarized ^{3}He cell is not being optically pumped, the ^{3}He will depolarize from spin-lattice interactions following an exponential decay with a time constant of T_1. The value of T_1 for a ^{3}He cell is typically on the order of tens or hundreds of hours, but it is dependent on the glass cell and the uniformity of the magnetic holding field.

The relaxation in the transverse direction does not require an exchange of energy and is usually much quicker. It is caused by a dephasing of the magnetic moments of the nuclei as they precess at different angular speeds because of different local magnetic field strengths caused by the magnetic moments of other nuclei. This transverse relaxation is called spin-spin relaxation, and its time constant is designated T_2. Additionally, inhomogeneities in the magnetic field can also cause a dephasing of a transverse magnetization, and in most cases this form of dephasing is the dominate cause of transverse relaxation. Relaxation caused by both spin-spin interactions and magnetic field inhomogeneities is designated by T_2^*, and when a transverse magnetization is induced in the bulk magnetization of a polarized ^{3}He cell, T_2^* is the time constant for the exponential decay of the transverse component of the bulk magnetization. For a ^{3}He cell, T_2^* is typically on the order of milliseconds, but similar to T_1, it depends on the characteristics of the magnetic holding field.

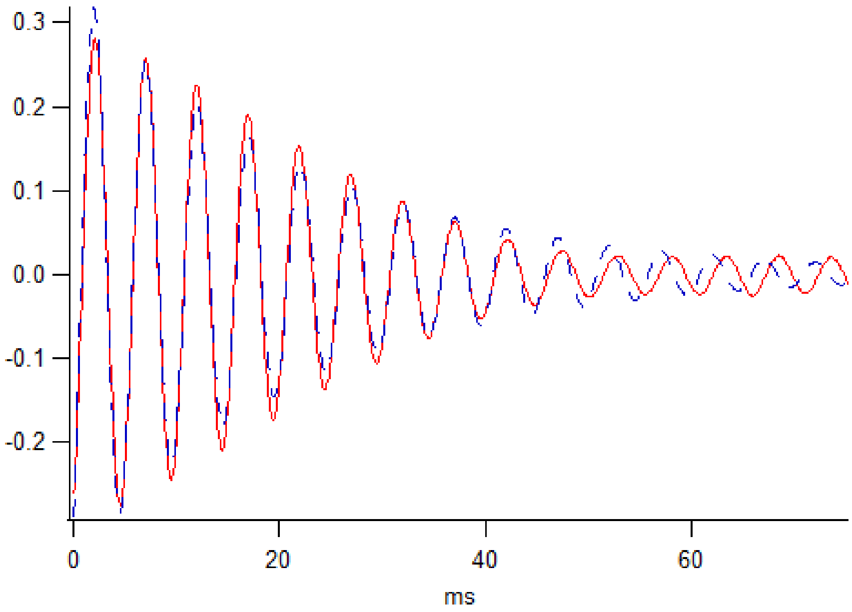

Figure 4.4: The FID signal of a polarized ^{3}He cell (red line) and the computational fit (blue line).

4.4.2 Free Induction Decay

FID measurements are made with a small coil of wire, about 1 cm in diameter and with 150 loops, that is taped to the side of the ^{3}He cell at an orientation orthogonal to the guide field. The FID loop is used both to transmit a RF pulse and to measure the induced resonance signal. The RF pulse from the FID coil perturbs the magnetization of the ^{3}He to create a transverse component of the magnetization that precesses in the guide field at the Larmor frequency. The FID signal is then measured as the transverse magnetization decays exponentially at the T_2^* relaxation time. An example of a FID signal is shown in Figure 4.4.

Typically FID measurements are done to extract information from the resonance frequency or the relaxation rate. For NPDGamma polarimetry, the amplitude of the FID signal is used to determine the relative ^{3}He polarization. The amplitude of the FID signal is dependent on several factors, such as the strength of the guide field, the orientation of the

FID coil, the sampling window of the FID signal, and the characteristics of the ^{3}He cell, so it is not a practical method of determining the absolute ^{3}He polarization. However, successive FID measurements of a polarized ^{3}He cell in a static configuration can be used to determine the change in ^{3}He polarization over time. When the ^{3}He cell is being optically pumped, the amplitude of several FID signals are used to measure the pump-up rate and to determine when the ^{3}He polarization is saturated. At room temperature, when the ^{3}He cell is not being optically pumped, maximum amplitude of several FID signals is fit to an exponential decay to determine the spin-lattice relaxation time T_1.

4.4.3 Adiabatic Fast Passage

Adiabatic fast passage is an NMR technique used for population inversion of the ^{3}He spins. In AFP, the entire polarized ^{3}He cell is exposed to an intense RF field whose frequency is swept across the Larmor frequency of the ^{3}He magnetic moments. In the rotating frame of the ^{3}He magnetic moments, the magnitude of the holding field B_0 in the positive $\hat{z}$ direction decreases as the RF frequency approaches the ^{3}He Larmor frequency reaching a minimum at the resonance frequency. After the RF frequency sweeps across the ^{3}He Larmor frequency, the holding field B_0 will appear to increase in magnitude in the negative $\hat{z}$ direction. This phenomenon causes an effective magnetic field that rotates from the positive $\hat{z}$ direction to the negative $\hat{z}$. The bulk magnetization of the ^{3}He precesses about the effective magnetic field and follows it to the negative $\hat{z}$ direction, reversing the spins of the ^{3}He nuclei. A conceptual illustraion of spin reversal by AFP is shown in Fig. 4.5.

The sweep rate must be slow enough for the ^{3}He magnetization to follow the rotation of the effective magnetic field adiabatically; if it is not, the spins of the ^{3}He will not flip. It must also be fast compared to the relaxation time T_2^*, or else the transverse component of the ^{3}He magnetization will decay away while the ^{3}He spins are swept through resonance. The transmission time for an AFP signal is greater than the relaxation time T_2^*; however,

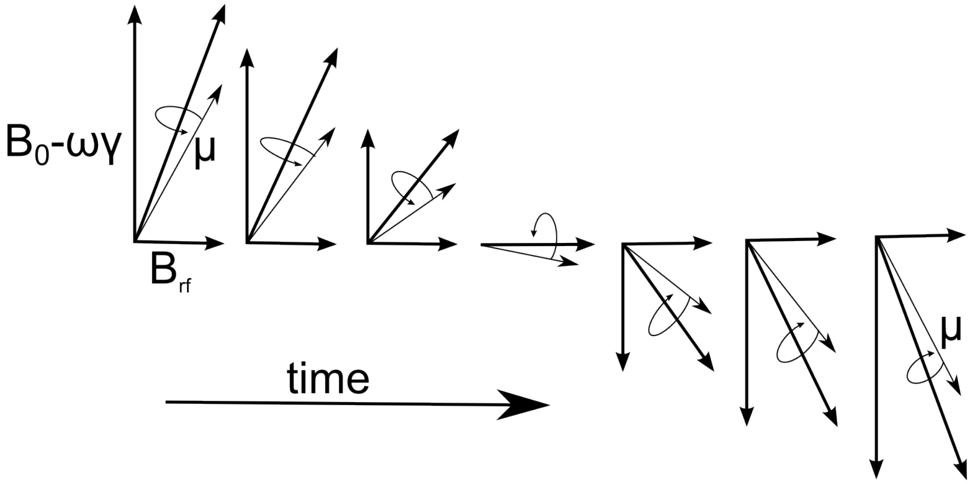

Figure 4.5: During spin reversal by AFP, an RF field B_{rf} with a time varying frequency ω is created orthogonal to a static field B_0. In the rotating reference frame of the magnetic moment μ, the effective field appears to rotate 180° as the frequency of the RF field increases.

the magnitude of the guide field is much greater than the magnetic RF field produced by the AFP coils, and the time that the RF field is near the resonance frequency is less than the relaxation time T_2^*, so there is little loss of the ^{3}He magnetization.

Since the RF field is swept across many frequencies, all the ^{3}He spins are swept across resonance regardless of differing resonance frequencies caused by magnetic field variations. This property makes AFP very effective at flipping the ^{3}He spins, with an efficiency of nearly 100%. An AFP spin flip reverses the phase of the ^{3}He FID signal, so a FID signal can be used to determine if an AFP spin flip is successful.

4.4.4 Electron Paramagnetic Resonance

The Rb electron paramagnetic resonance (EPR), or Zeeman resonance, is used to measure the ^{3}He polarization in the optical pumping station [50]. The ^{3}He polarization determined with EPR is an absolute polarization compared to the relative polarization determined from FID measurements. The Rb EPR frequency in the guide field is shifted by the ^{3}He magnetization and Rb$-^3$He spin-exchange interactions. The frequency shifts from both contributions are proportional to the ^{3}He polarization and density, such that

$$\Delta\nu = \kappa_{eff}[He]P_{He}, \tag{4.27}$$

where κ_{eff} is a dimensionless constant that depends on the temperature and the physical shape of the cell. The ^{3}He density is determined separately from neutron transmission measurements, and κ_{eff} is calculated. Thus a measurement of the change in the EPR frequency of Rb when the ^{3}He polarization is reversed can determine the ^{3}He polarization.

EPR measurements are performed during SEOP because the process of pumping the Rb vapor is an integral part of the measurement. During an EPR measurement, an RF field that sweeps across the transition frequency between the F=3, m=3 and F=3, m=2 states of the Rb atom is applied to the ^{3}He cell with a pair of coils orthogonal to the guide field, and the RF field reverses the spins of the Rb at the resonance frequency. The EPR coils are not oriented as Helmholtz coils because it is not necessary that they provide a uniform RF field; the EPR signal quickly sweeps across a range of frequencies in such a way that all the Rb atoms in the sampling region experience the resonance condition. Before the spin reversal, the Rb polarization was nearly 100% and there was little absorption and subsequent decay of the Rb atoms, but afterwards there is a significant amount of absorption by the Rb vapor. Most Rb atoms decay by quenching with N_2, but 3-5% decay by emitting a fluorescence photon at either the D1 or D2 wavelength, 795 nm and 780 nm respectively. The 780 nm decay photons are detected by a photodiode, and since the rate at which the Rb is optically pumped is fast compared to the sweep rate of the RF field, a peak in emission will determine the EPR frequency of the Rb. Photodiode signals from EPR measurements with two different ^{3}He polarizations are shown in Fig. 4.6. EPR measurements are done with Rb because the large difference between the D1 and D2 wavelengths enables the use of

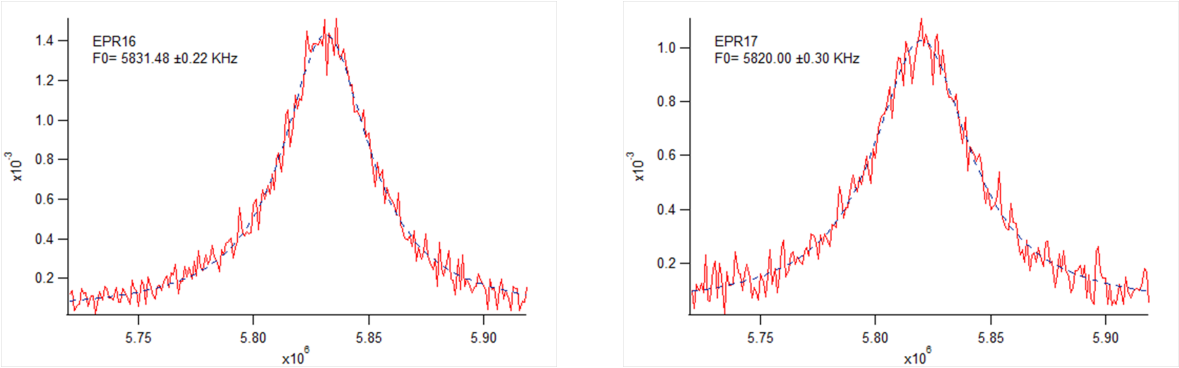

(d) **(e)**

Figure 4.6: EPR signals of a polarized ^{3}He cell for both directions of the ^{3}He polarization. The x-axis is the frequency of the time-varying RF field, and the y-axis is the voltage signal from the photodiode.

an optical filter to block photons at the Rb D1 wavelength, which is the wavelength of the pumping laser, because scattered laser light would saturate the photodiode. The difference between the D1 and D2 wavelengths for K is only 3 nm, which is too small for currently available optical filters.

After the first EPR measurement, the ^{3}He polarization is reversed with an AFP spin flip and a second EPR measurements is take to determine the change in the EPR frequency. Then the ^{3}He polarization is reversed again to return the ^{3}He polarization to the direction the lasers are pumping. In the $\sim$12 Gauss guide field used during SEOP, the EPR frequency of Rb is 5800 kHz and the change in the EPR frequency at a maximum ^{3}He polarization is usually on the order of 10 kHz, so the effect is small and the guide field needs to be stable to not obscure it.

4.5 Optical Pumping Station

The polarized ^{3}He cells used for neutron polarimetry during the NPDGamma experiment are polarized at an optical pumping station utilizing SEOP. A schematic of the optical pumping station is shown in Fig. 4.7. At the optical pumping station, the ^{3}He cell is placed in a static magnetic field of 12 Gauss to maintain the Rb, K, and ^{3}He polarizations. The 12 Gauss field is created by a pair of Helmholtz coils connected to an Agilent power supply operating in constant current mode. Nonmagnetic materials were used for the construction of the optical pumping station to minimize depolarization of the ^{3}He caused by magnetic field gradients. The structural supports of the Helmholtz coils, NMR coils, and oven are made of garolite, the base of the optical pumping station is constructed from an 80/20 aluminum erector set, and all the fasteners are brass. The ^{3}He cell is placed in an oven with a Teflon base and borosilicate glass walls on the sides and top, which are supported by alumina ceramic columns. The glass walls are necessary for the transmission of the laser light and the detection of fluorescent light with a photodiode for EPR. All of the materials of the oven are able to tolerate operating temperatures of over 200 °C, and are nonmagnetic. Sections of the oven walls that do not need to be transparent are further isolated by Fiberfrax isolation. The oven is heated by pressurized air that passes through a 120 Volt air heater at the bottom of the optical pumping station and enters the oven from an inlet in the center of its base. As hot air enters the oven, air in the oven seeps out between the glass panes of the walls, preventing over pressurization. The ^{3}He cell is secured to a Teflon block with Kapton tape above the hot air inlet. This protects the ^{3}He cell from direct contact with the hot air stream and positions it in the center of the oven. The interior volume of the oven is a cube with 7 inch sides. This relatively small size was chosen to reduce both the heat gradients in the oven and the time and power required to heat the ^{3}He cell.

The temperature of the optical pumping station's oven is maintained to within one degree Celsius by a custom-designed temperature controller. The temperature controller has five Omega process controllers to monitor the oven. Three process controllers monitor the air temperature at the outlet of the air heater and at top and bottom corners inside the oven with resistance temperature detectors (RTD). The other two monitor the air heater temperature

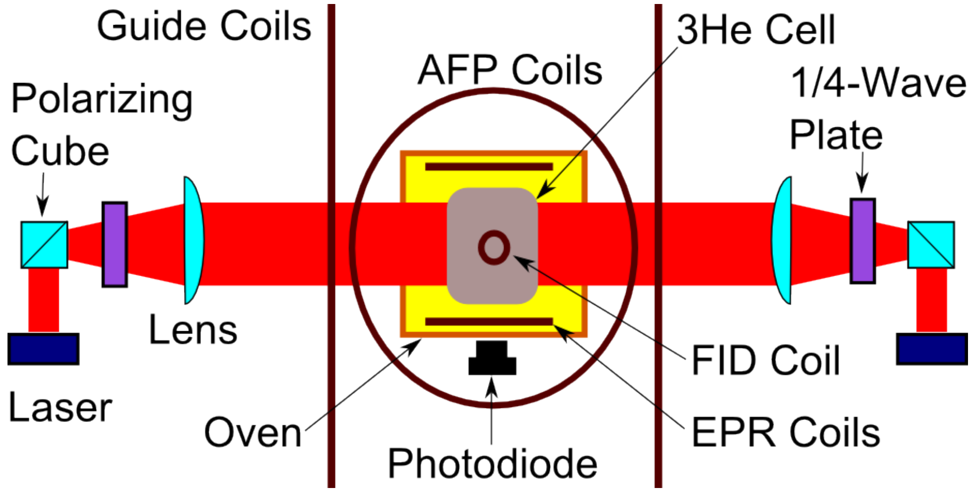

Figure 4.7: Schematic of the optical pumping station used to polarize ^{3}He cells.

close to its intake with a thermocouple and the flow rate into the air heater with an air flow meter. The Omega process controller that monitors the temperature at the top of the oven is configured as a PID controller, which keeps the temperature stable at a programmable set point. The set point temperature is 195 °C for ^{3}He cells used during neutron polarimetry. The rest of the Omega controllers are configured as on/off controllers that shut off the current to the air heater if the monitored temperatures or air flow rate are outside of safe operating values. The temperature controller allows the optical pumping station to be safely operated unsupervised.

The laser used to polarize the Rb vapor is a class IV, 250 Watt, diode array laser with a narrow bandwidth of ∼1 nm and a peak wavelength of 795 nm at the D1 resonance wavelength of Rb. The spectrum of the laser through a pumping ^{3}He cell is shown in Fig. 4.8. The laser is powered by a 60 Amp high voltage power supply. The laser is water cooled by a chiller that recirculates water at between 1.5 and 2 gallons per minute to maintain the laser's optimal operating temperature. The flow rate of the chiller is monitored by an interlock system that shuts off power to the laser to protect it from over heating. The linearly polarized 795 nm light is reflected by a polarizing cube to improve the linear polarization

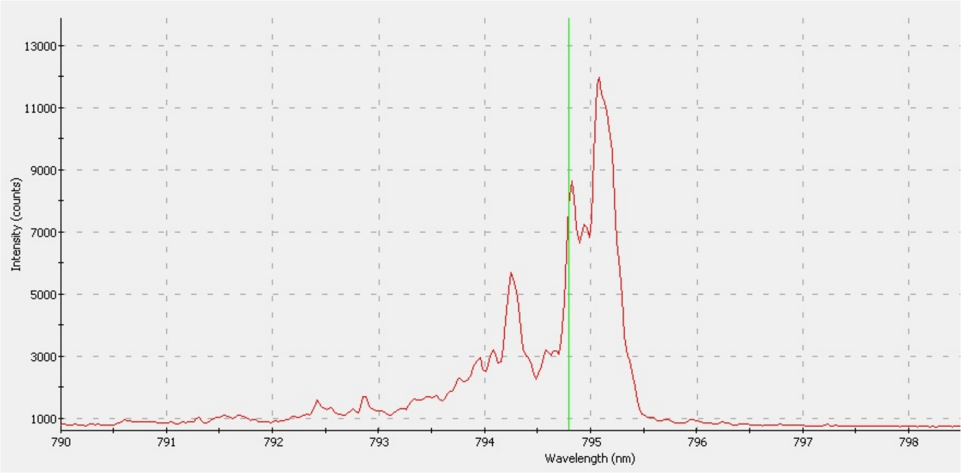

Figure 4.8: The spectrum of the diode array laser was measured through a ^{3}He cell in the optical pumping station. The dip in the spectrum at 795 nm is caused by absorption in Rb vapor.

and is then circularly polarized by a liquid crystal quarter-wave plate. The light emitted from a diode array laser diverges quickly compared to the distance from the laser to the ^{3}He cell, so the laser light is focused by a series of lens to improve coherency and power incident on the ^{3}He cell.

^{3}He polarizations of greater than 40% were routinely achieved with this optically pumping station during commissioning of the NPDGamma experiment. When a second laser was later installed that pumped K at its D1 resonance wavelength of 770 nm, the performance of the optical pumping station increased and ^{3}He cells were polarized to greater than 60%.

Chapter 5

Neutron Polarimetry

The main purpose of the neutron polarimetry measurements is to determine the neutron polarization P_n and spin-flip efficiency ϵ_{sf} of the neutrons captured on the aluminum, chlorine, and para-hydrogen targets. The neutron polarization and spin-flip efficiency are multiplicative corrections to the observed γ-ray asymmetry $A_{\gamma,obs}$. The physical asymmetry $A_{\gamma,phys}$ is calculated by

$$A_{\gamma,phys} = \frac{A_{\gamma,obs}}{P_n \epsilon_{sf}}. \tag{5.1}$$

The NPDGamma experiment has the goal of measuring the observed γ-ray asymmetry to a precision of 1×10^{-8}; this could correspond to a 5% statistical uncertainty if the γ-ray asymmetry measured is as high as the current experimental limit of 2×10^{-7}. Therefore, the goal of the neutron polarimetry measurements is to determine the neutron polarization and spin-flip efficiency captured on the para-hydrogen target to an uncertainty of less than 2%, so that the systematic uncertainty does not greatly contribute to the overall uncertainty of the NPDGamma experiment. In fact, an uncertainty of less than 1% was obtained.

The neutron polarization and spin-flip efficiency are determined from transmission measurements through a polarized ^{3}He cell, which utilizes the large spin-dependent neutron capture cross section of polarized ^{3}He. Neutron polarimetry with polarized ^{3}He is possible for the NPDGamma experiment because the pulsed neutron beam at the SNS enables transmission measurements to be taken at individual neutron wavelengths. The transmission of polarized neutrons through unpolarized and polarized ^{3}He as a function of wavelength is given by Eqs. 4.4 and 4.20 respectively, and these transmission functions can be solved for the neutron polarization and spin-flip efficiency.

The NPDGamma experiment requires a high-flux neutron beam to reach a statistical uncertainty of 1×10^{-8} because the statistical uncertainty scales as $\frac{1}{\sqrt{N}}$, where N is the total number of neutron captures. Therefore, the neutron beam has a large cross sectional area. It is not possible to measure the transmission of the entire neutron beam through a ^{3}He cell, so several measurements are taken at different locations in the beam, and the results of these measurements are weighted by the neutron flux at each location and averaged to determine the neutron polarization and spin-flip efficiency of the entire neutron beam as a function of wavelength. Then the total neutron polarization and spin-flip efficiency of the neutron beam captured on the various targets can be calculated to correct the corresponding observed γ-ray asymmetry.

This chapter will cover various aspects of neutron polarimetry done for the NPDGamma experiment. The method of performing neutron polarimetry with polarized ^{3}He will be discussed. The neutron polarization and spin-flip efficiency are determined from transmission measurements, and the results are compared to models of the FNPB, supermirror polarizer, and RFSF. The weighted averages of the polarimetry results and their uncertainties are calculated.

5.1 Neutron Polarimetry Measurements

5.1.1 Polarized ^{3}He Cell Transport

The cell is polarized at the optical pumping station described in Sec. 4.5 and transported to the FNPB in a transport coil. The transport coil provides a uniform magnetic field to maintain the ^{3}He polarization while the polarized ^{3}He cell is moved from the guide field of the optical pumping station to the guide field of the NPDGamma experiment. The transport coil is a solenoid with a 36 inch length and 10 inch diameter that is wrapped in 18 gauge copper wire. The magnetic field in the transport coil is between 12-15 Gauss, and it is created by a direct current from an Agilent power supply operating in constant current mode. During transport, the ^{3}He cell passes through several magnetic field gradients that have the potential to depolarize the ^{3}He; however, the gradients are over a large enough distance that the adiabatic condition is met while the ^{3}He cell is moved through them. The amount of ^{3}He depolarization during transport is small enough that ^{3}He polarizations between 60% and 70% have been available on the beamline. This is near the polarization limit of the optical pumping station.

5.1.2 Polarimetry Apparatus

Polarized ^{3}He transmission measurements are taken on an apparatus installed downstream of the CsI(Tl) detector array. The polarimetry apparatus, without the ^{3}He cell, is shown in Fig. 5.1. During neutron polarimetry measurements, a polarized ^{3}He cell is placed in the beamline in front of the neutron monitor M4. The ^{3}He cell is centered within a pair of AFP coils that can be used to reverse the ^{3}He polarization. A set of ^{6}Li collimators defines a beam so that all transmitted neutrons pass through the ^{3}He cell, and thus the neutron monitor measures the transmission through the ^{3}He cell.

The ^{3}He cell used for polarimetry is a hybrid K and Rb cell called “Hedy Lamarr”, following the Instrument Development Group’s convention of naming ^{3}He cells after notable scientists. The ^{3}He cell is cylindrical with an outside diameter of 7.5 cm that varies by less than 1 mm and a maximum length of 10.3 cm, measured from the center of the circular faces. The length decreases towards the edge of the ^{3}He cell because the circular faces have curvature as a result of the fabrication process. The edge of the neutron beam defined by the ^{6}Li collimators intersects the ^{3}He cell $\sim$1 cm from the cylindrical sides of the ^{3}He cell, and at this location the length of the ^{3}He cell is between 9.8 cm and 10.0 cm. The partial pressure of the ^{3}He at 295 K is 1.31 ± 0.03 bars. The ^{3}He cell is supported on an acrylic V-block in the center of the polarimetry apparatus, and it is secured with Kapton tape.

The structural components of the polarimetry apparatus are aluminum, garolite, and acrylic, and they are secured with brass and Teflon fasteners. Nonmagnetic materials are used to minimize magnetic field gradients that can increase the depolarization rate of the ^{3}He polarization. Moreover, nonconductive materials are used closer to the ^{3}He cell to prevent eddy currents induced during an AFP-flip of the ^{3}He polarization from creating AC magnetic field gradients.

After polarized ^{3}He transmission measurements, the ^{3}He cell is depolarized by a NdFeB magnet, which is held close to the ^{3}He cell and slowly moved over its surface. The local magnetic field produced by the NdFeB magnet is much greater than the $\sim$9.4 Gauss guide field, and it creates large magnetic field gradients in the ^{3}He cell that reduce the spin-lattice relaxation time T_1 from over 200 hours to less than a few seconds according to the relation in Eq. 4.26. After waving the NdFeB magnet over the ^{3}He cell for several seconds, a FID measurement of the ^{3}He cell is used to verify that the ^{3}He is unpolarized before measuring the unpolarized neutron transmission. The ratio of the transmission signals through polarized ^{3}He with the RFSF on and off will be unity if the ^{3}He is unpolarized, and this ratio is calculated to confirm that the ^{3}He is unpolarized.

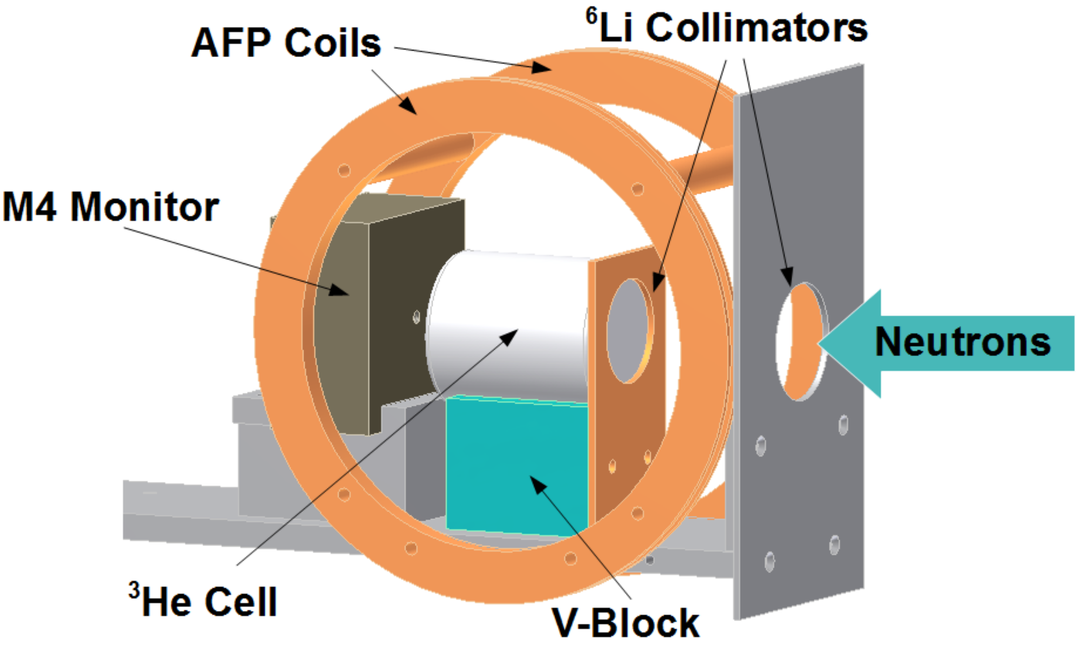

Figure 5.1: The polarimetry apparatus with the M4 monitor positioned directly behind the ^{3}He cell.

The polarimetry apparatus was installed in several positions and mounting configurations for the various polarimetry measurements taken during commissioning and running of the NPDGamma experiment. Before the installation of the para-hydrogen target, the polarimetry apparatus could be scanned horizontally and vertically in a 3-by-3 grid with a 4 cm separation between each grid point. Measurements taken with this scannable configuration are used to determine the beam-average neutron polarization and RFSF efficiency. During polarimetry measurements after the para-hydrogen target was installed, the polarimetry apparatus was mounted in a fixed position at the center of the neutron beam behind a 1.75 cm opening in the ^{6}Li shielding at the back of the para-hydrogen target; these measurements were used to verify that the current to the guide coils remained optimized and to measure the neutron polarization during the running of the NPDGamma experiment.

5.1.3 Neutron Monitor Signals

Data for the NPDGamma experiment is collected in sequences of eight beam pulses, and for polarimetry measurements between 200 to 500 sequences of eight pulses are collected for each ^{3}He transmission measurement. Thus, the neutron monitor M4 collects voltage signals for 1600 to 4000 neutron pulses for each ^{3}He transmission measurement. Voltage signals from M4 are recorded into 40 time bins for each neutron pulse, and neutron pulses occur every 16.67 ms for a 60 Hz pulsed beam.

Analysis of polarimetry measurements is performed with the data analysis program ROOT [51]. During analysis, cuts on the M4 data quality remove eight pulse sequences with corrupted data. Moreover, the accelerator periodically skips proton pulses to the mercury target once every 10 minutes for diagnostic purposes. During a skipped accelerator pulse, the only neutrons detected in M4 are slow neutrons from previous pulses that the choppers did not block. Eight-pulse sequences with a skipped pulse are also cut from analysis. Data cuts for skipped pulses utilize the signal from monitor M1 because M1 is unaffected by the polarimetry apparatus configuration, ^{3}He polarization, or RFSF state. The voltage signals from neutron pulses that pass the data quality cuts are averaged for further analysis.

The M4 signals need to be corrected for an electronic pedestal (dependent on the gain of the monitor) during analysis. The M4 signal with the secondary shutter closed is used to measure the electronic pedestal, whenever polarimetry measurements are taken for the NPDGamma experiment. The transmission through polarized and unpolarized ^{3}He measured by M4 with the pedestal subtracted are shown in Fig. 5.2. For some configurations of the polarimetry apparatus, there is also a room neutron background in the M4 signals when the secondary shutter is open that cannot be determined with the pedestal measurements, and it is discussed in detail in Sec. 5.6.2.

The neutron monitor signals are recorded after a time offset t_{off}, which is the time difference between the creation of the neutron pulse in the spallation target and the arrival

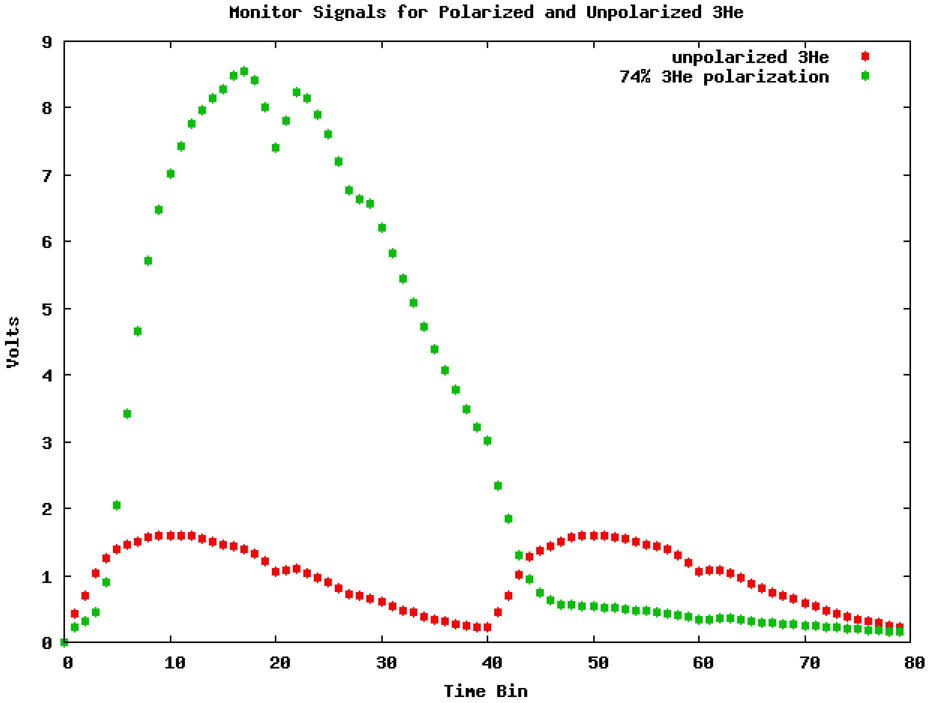

Figure 5.2: Transmission signals through a polarized and unpolarized ^{3}He cell for both neutron spin states. The edges in the plots at time bins 20 and 27 (60 and 67 for the second pulse) are caused by Bragg scattering in aluminum.

of the neutron pulse at the para-hydrogen target. With a pulsed source, the neutron wavelengths can be determined with the time-of-flight from the moderator. The average wavelength of the neutrons in each time bin is determined from the neutrons' time-of-flight in ms by

$$\lambda = \frac{h}{m_n d}\left(\frac{16.67}{40}tb - t_{off}\right)10^7, \tag{5.2}$$

where h is Planck's constant, m_n is the neutron mass, d is the distance from the moderator to M4, and tb is number of the time bin. Therefore, the distance from the moderator to M4 determines the wavelength of transmitted neutrons measured in each time bin. The distance from the moderator to M4 can be determined from the as built drawings as well as from edges in the transmission signal caused by Bragg scattering in aluminum components of the neutron beamline because aluminum metal has a crystalline structure that causes Bragg scattering of neutrons with a maximum wavelength of 4.05 Å and 4.68 Å, corresponding to a velocity of 976.9 m/s and 846.0 m/s respectively.

When M4 was in the polarimetry configuration used before the installation of the para-hydrogen target, the time offset was 10.685 ms, and the aluminum Bragg edges were visible in the transmission signal of M4 at time bins corresponding to time-of-flights of 18.39 ms and 21.31 ms. For these two time-of-flights, the neutrons' flightpath distance from the moderator to M4 is calculated using Eq. 5.2 to be 17.97 m for 4.05 Å and 18.03 m for 4.68 Å, for an average of 18.0 m. The uncertainty in the flightpath distance is dependent on the 0.42 ms width of the time bins and is found to be 0.14 m.

Measurements from the as built drawing of the FNPB and the NPDGamma experiment specify the distance from the moderator to the start of the supermirror polarizer as 15.30 m, and the distance from the start of the supermirror polarizer to the end of the CsI(Tl) detector array as 2.64 m. The distance from the front surface of the Li collimator on M4 to the back of the CsI(Tl) detector array was 0.08 m during polarimetry measurements before the installation of the para-hydrogen target. The sum of these distances give the distance from the moderator to M4 to be 18.01 m, which agrees with the distance found with the aluminum Bragg edges to within the uncertainty of 0.14 m.

At a distance of 18.0 m from the moderator, the range of the neutron wavelengths detected by the neutron monitor M4 is calculated with Eq.5.2 to be 2.35 Å 5.92 Å. The uncertainty of the neutron monitor position results in a multiplicative uncertainty in the wavelength of $\Delta\lambda = \frac{\Delta d}{d}\lambda = 0.008\lambda$. The opening and closing of the chopper windows and the ramping of the RFSF current limit the useful wavelength range to 3.7 Å to 5.8 Å for neutron polarimetry measurements.

5.1.4 AFP Coils

The ^{3}He polarization can be reversed by AFP (Sec. 4.4.3), which allows the determination of the transmission through a polarized ^{3}He cell with the neutron and ^{3}He spins aligned and antialigned, without reversing the neutron polarization with the RFSF. Measuring the transmission of both neutron spins states is necessary to determine the efficiency of the RFSF and to determine the neutron polarization independent of the RFSF. The AFP coils are configured as Helmholtz coils with a diameter of 9.5 inches (24.13 cm) and are made of 25 windings of 18 gauge copper wire on a garolite support. When the ^{3}He polarization is reversed, a function generator is manually triggered to create an oscillating signal that sweeps from 20 kHz to 60 kHz in 2 s, with a peak-to-peak amplitude of 0.8 V. An RF amplifier amplifies the output from the function generator by a factor of 100, and the output of the RF amplifier then goes to the AFP coils.

Each AFP reversal of the ^{3}He polarization (henceforth called an AFP-flip) partially depolarizes the ^{3}He, so it is necessary to measure the efficiency of an AFP-flip before calculating the RFSF efficiency. The AFP efficiency can be determined from FID signals, which are proportional to the ^{3}He polarization, or from the ^{3}He polarization measured with neutron transmission signals using the relations

$$S_n = \epsilon_{AFP}^n S_0 \tag{5.3}$$

$$\epsilon_{AFP} = \left(\frac{S_n}{S_0}\right)^{\frac{1}{n}}, \tag{5.4}$$

where ϵ_{AFP} is the efficiency of a single AFP-flip, and the variables S_0 and S_n represent either the FID signals or the measured ^{3}He polarizations before and after n AFP-flips respectively.

When the AFP efficiency is calculated with FID signals, it is assumed that there is no loss in ^{3}He polarization when the FID signals are induced. This assumption is reasonable because the depolarization due to an FID measurement was found to be 0.00039±0.00079 from a

Table 5.1: Comparison of the AFP efficiency determined by FID signals and ^{3}He depolarization.

Number of AFP-flips	He Depolarization	FID AFP Efficiency
2	0.9675	0.9652
6	0.9698	0.9668
2	0.9690	0.9691
10	0.9747	0.9750
2	0.9653	0.9698
10	09763	0.9758
2	0.9757	0.9715
2	0.9753	0.9732

sample of 5 FID measurements. The results of 8 measurements of the AFP efficiency are compared in Table 5.1, which lists the number of AFP-flips between each measurements and the AFP efficiency calculated using either the decrease in the FID signal or the depolarization of ^{3}He. The two methods are independent measurements of the AFP efficiency, and they obtained consistent results. The average AFP efficiency is 0.9721±0.0035 using FID signals and 0.9717±0.0040 by determining the ^{3}He depolarization for a combined AFP efficiency of $\epsilon_{AFP} = 0.972 \pm 0.004$.

5.1.5 ^{6}Li Shielding

^{6}Li has a large neutron capture cross section via the reaction $^6Li + n \rightarrow \alpha + {}^3H$ and is commonly used for neutron shielding. There are no γ-rays emitted during neutron capture on ^{6}Li, which makes ^{6}Li an ideal neutron shielding material for the NPDGamma experiment. Three collimators made of ^{6}Li suspended in plastic are used to capture the neutron beam that does not pass through the ^{3}He cell. The first collimator is 3.75 inches (9.53 cm) upstream of the ^{3}He cell and 2.25 inches (5.72 cm) in diameter; the second is positioned directly in front of the ^{3}He cell and is 2.0 inches (5.08 cm) in diameter; and the third is attached to the surface of the neutron monitor and is also 2.25 inches (5.72 cm) in diameter. The position

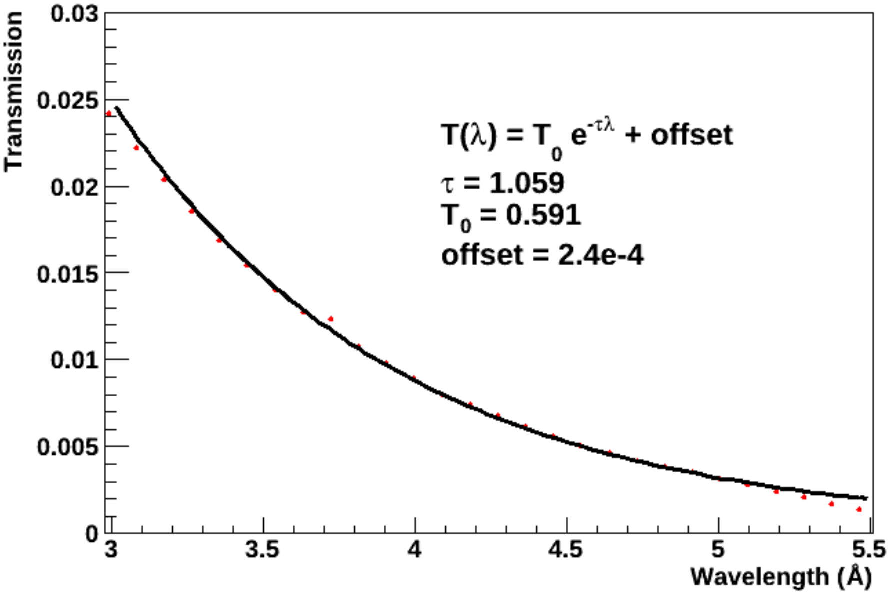

Figure 5.3: The measured neutron transmission through ^{6}Li shielding (red points), and the exponential fit (black line).

of the neutron monitor relative to the ^{3}He cell depends on the mounting configuration of the polarimetry apparatus.

The transmission through the ^{6}Li shielding is determined from measurements with and without the shielding placed directly behind the RSFS; the ratio of the pedestal-subtracted signals are then fitted to an exponential function. The results of the fit are shown in Fig. 5.3, and they are consistent with other measurements made of the transmission through the ^{6}Li shielding [52]. It is necessary for the neutron beam to also be transmitted through the ^{3}He cell, because the unattenuated neutron flux from the supermirror polarizer saturates the neutron monitor M4. The expected transmission signal without ^{6}Li shielding or a ^{3}He cell in the beam can then be determined from the measurement of transmission through ^{6}Li by correcting for the exponential attenuation of the ^{6}Li.

5.2 Computational Models

Monte Carlo computer models that simulate the neutronic characteristics of FNPB, supermirror polarizer, and RFSF were created to predict their performance before the assembly of the NPDGamma experiment. The models demonstrate the physical understanding of the various components of the NPDGamma experiment that can effect the properties of the neutron beam. Thus, the models are used to simulate the neutron beam when information cannot be measured and to test the plausibility of results measured with neutron transmission through ^{3}He.

5.2.1 Beamline and Supermirror Polarizer Models

The FNPB from the moderator downstream to the supermirror polarizer is modeled with the neutron simulation package McStas [53, 54]. McStas simulates neutron instrumentation with Monte Carlo geometrical ray-tracing techniques, where neutron beamlines and spectrometers are modeled as a series of simpler components, and each component has a set of definition parameters that describes how it modifies the neutron beam characteristics (e.g. divergence, wavelength spread, spatial, and time distributions). The neutron properties that are simulated by McStas are position (x,y,z), velocity (v_x,v_y,v_z), spin (s), time (t), and a weight factor (p). McStas adjusts these properties for each simulated neutron according to the effect of each component. The purpose of the weight factor is to simulate the effect of components with an analytical transmission function by adjusting the weight factor (neutrons with a very small weight factor are discarded).

The beamline model produced by McStas includes the effects of several sections of neutron guide and the two neutron choppers, and the output consists of a large set of neutrons with their position, velocity, weight, wavelength (function of velocity), and chopper cut (function of position and time) at the end of the beamline [28]. In the beamline model, the x, y, and z axes are defined as beam-left, vertical, and parallel to the neutron beam respectively. The output of the beamline model is used as the input of a separate McStas model of the supermirror polarizer, in which a simulated set of neutrons at the end of the supermirror polarizer also includes a polarization factor [32]. After the supermirror polarizer, neutron positions are extrapolated by assuming that the neutrons travel in a straight line without any further interactions. The neutron positions in the xy-plane are calculated at a distance d from the supermirror polarizer using the neutron positions at the exit of the supermirror polarizer and the x, y, and z components of their velocities according to the relations

$$x(d) = x_{smp} + \frac{v_x}{v_z} d \tag{5.5}$$

$$y(d) = y_{smp} + \frac{v_y}{v_z} d. \tag{5.6}$$

The neutron flux is simulated for various collimators and neutron wavelengths by placing requirements on the simulated neutrons' position, wavelength, and chopper acceptance, and then summing the weight factors of each simulated neutron that meets these requirements. The neutron polarization can also be simulated for various collimators and neutron wavelengths by averaging the simulated neutron's polarization weighted by their weight factor.

The simulated total neutron flux through a cross section of the neutron beam 2.3 m downstream of the supermirror polarizer is shown in Fig. 5.4, while Fig 5.5 displays the simulated neutron flux versus wavelength through a 5 cm diameter collimator in the center of the neutron beam 2.3 m downstream of the supermirror polarizer. Unfortunately, the beamline and supermirror polarizer models do not simulate Al Bragg scattering. The effect of Al Bragg scattering can be seen in all the CsI(Tl) detector and neutron monitor signals as two edges at 4.05 Å and 4.68 Å and is visible in Fig. 5.2.

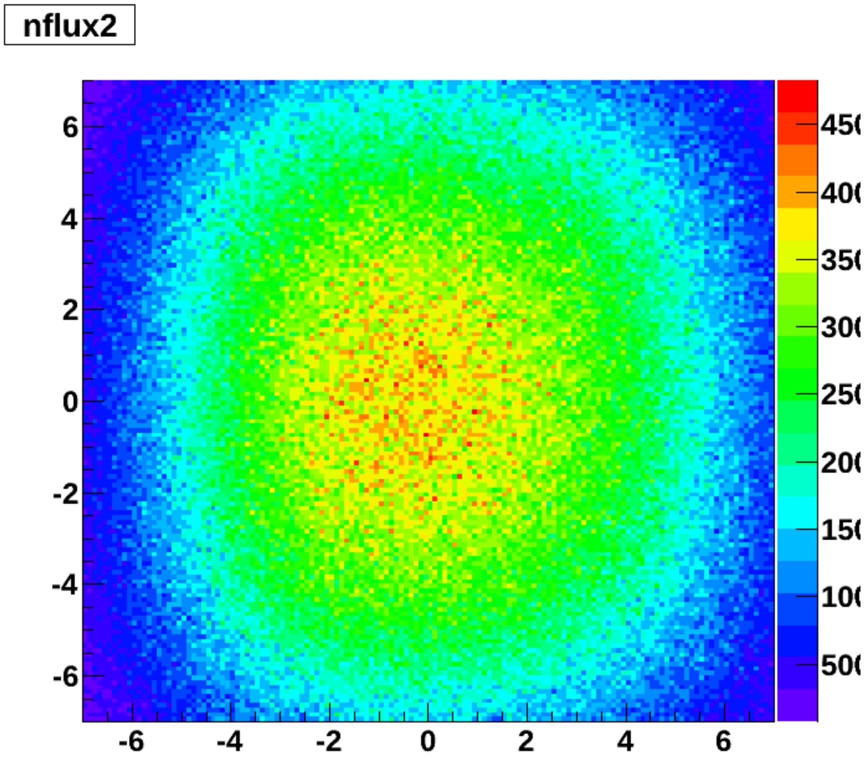

Figure 5.4: Simulation of the neutron flux through a 14 cm by 14 cm cross section of the neutron beam 2.3 m downstream of the supermirror polarizer.

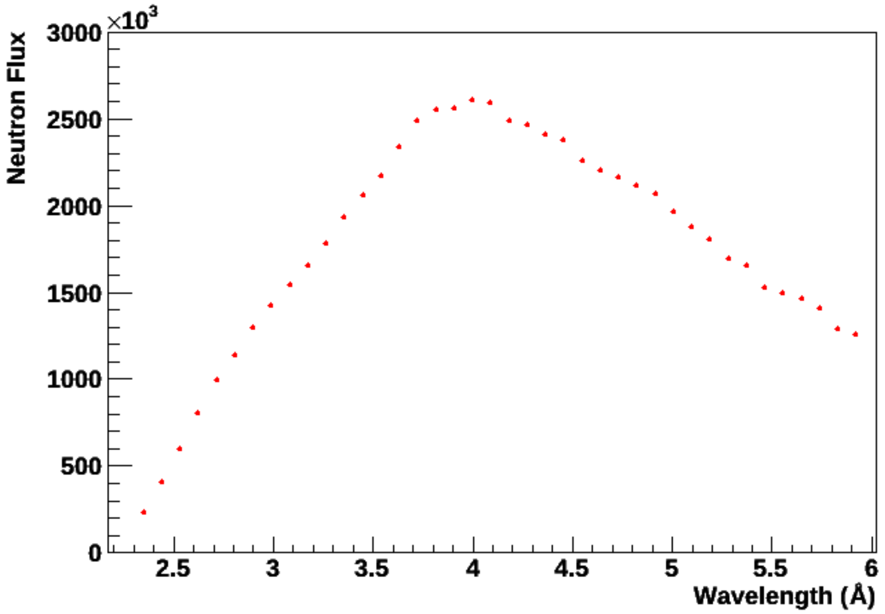

Figure 5.5: Simulated neutron flux versus wavelength 2.3 m downstream of the supermirror polarizer.

5.2.2 RFSF Model

The RF field in the RFSF is calculated from the magnetic potential $B(r,z) = -\nabla\phi(r,z)$ with the boundary condition that the component of the magnetic field normal to the surface of the Al cylinder vanishes. The Al cylinder is a conductor, so the eddy currents in the Al caused by the oscillating RF field cancel the components of the magnetic field normal to them. The solutions of the RF field in the RFSF are modified Bessel functions, and the solutions to the spin equations of motion of the neutrons in the RF field are solved numerically as the neutrons traverse through the RFSF in a straight line path [37].

The RFSF model gives a position-dependent neutron spin-flip efficiency in a 20 cm by 20 cm grid in the xy-plane at points spaced every 2 cm in the x and y direction. The grid corresponds to positions in the center of the RFSF because the probability of a neutron spin flip can be closely approximated (even without knowing the exact neutron trajectory) from

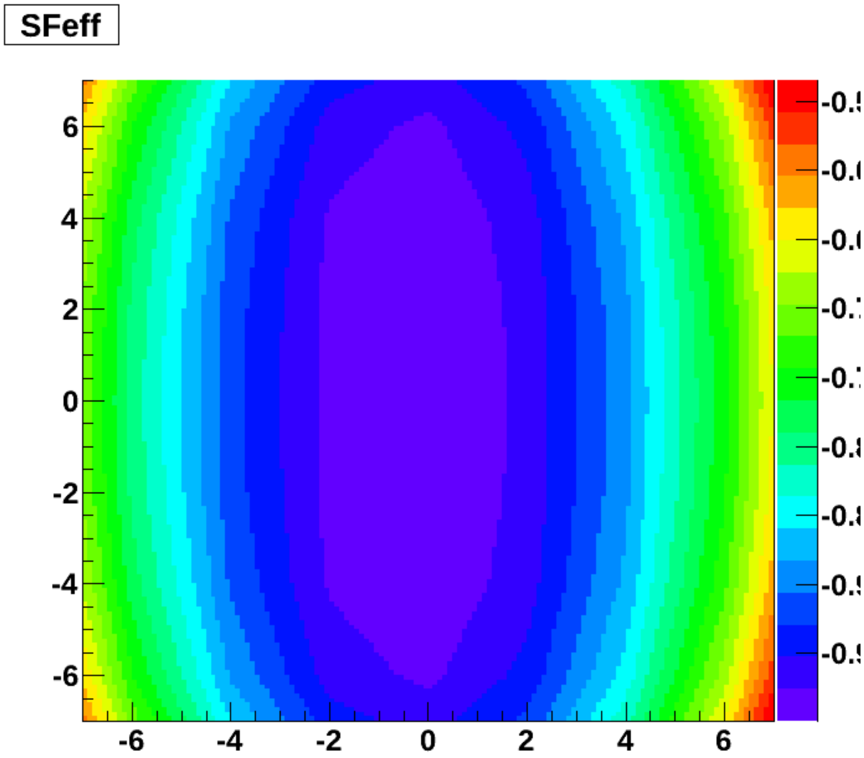

Figure 5.6: Simulation of the spin-flip efficiency through a 14 cm by 14 cm cross section of the neutron beam 2.3 m downstream of the supermirror polarizer.

a neutron's position in the xy-plane at the center of the RFSF. Neutron spin-flip efficiencies between grid points are linearly interpolated from adjacent points. The average spin-flip efficiency of the neutron beam by the RFSF is determined by assigning each simulated neutron from the supermirror polarizer model a spin-flip efficiency based on its position in the xy-plane at the center of the RFSF (1.3 m downstream of the supermirror polarizer). The location-dependent spin-flip efficiency of the simulated neutron flux 2.3 m downstream of the supermirror polarizer is shown in Fig. 5.6.

5.3 Spin-Flip Efficiency

The RFSF rotates the neutron spins 180° with an efficiency $\epsilon_{sf} \leq 1$, and when the RFSF is powered, the neutron polarization transmitted through it is equal to $(1 - 2\epsilon_{sf})P_n$. The transmission through a polarized ^{3}He cell with neutron polarization flipped by the RFSF can be calculated by following the same procedure used to determine the transmission without the RFSF in Eq. 4.20 and using as input the effective polarization $(1 - 2\epsilon_{sf})P_n$. The transmission with the neutron polarization flipped by the RFSF is given by

$$T_{sf}(\lambda) = T_0(\lambda)e^{-\chi\lambda}\cosh(\chi P_{He}\lambda)\left[1 + (1 - 2\epsilon_{sf})P_n \tanh(\chi P_{He}\lambda)\right]. \tag{5.7}$$

The spin-flip efficiency of the RFSF is calculated from Eq. 3.14 and is dependent on the resonance frequency of the RFSF, the neutron's Larmor frequency in the guide field, and the Larmor frequency in the RF field. The spin-flip efficiency is optimized by tuning the currents generating the guide field and the RF field, so that the ratio of the transmission signals through polarized ^{3}He with the RFSF on and off (referred to as the flipping-ratio) is maximized.

The guide field needs to meet the resonance condition that the neutron's Larmor frequency in the guide field equals the resonance frequency of the RFSF, which is set by hardware. The flipping-ratio is calculated for different current settings of the Danfysik power supply that powers the guide field. After at least three transmission measurements, the flipping-ratios are fitted to a parabola and the current setting of the Danfysik power supply is set to its optimal value. The flipping-ratio for three Danfysik current settings is shown in Fig. 5.7a, and the fit of current setting is shown in Fig. 5.7b.

The amplitude of the RF field generated in the RFSF also has to be adjusted so that the spins of neutrons transmitted through it are rotated 180°. The amplitude of the RF current is a time-varying function of the neutron time-of-flight that is scaled by a constant

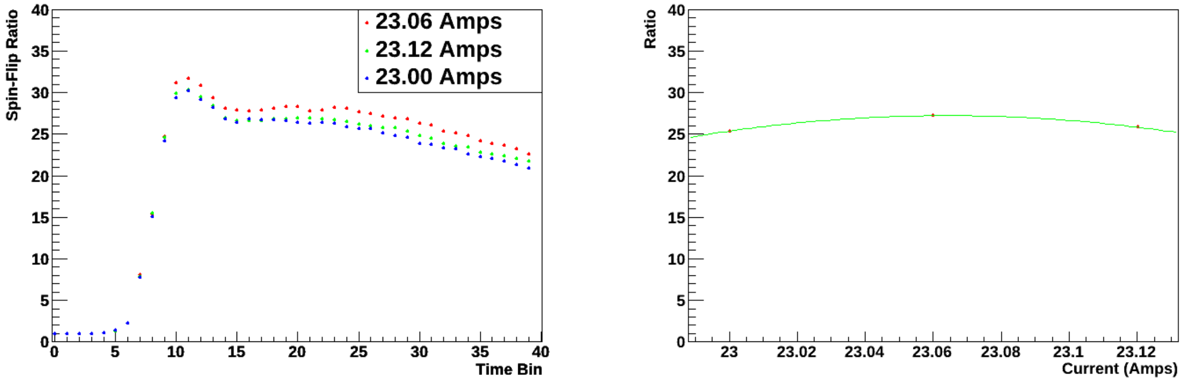

(a) **(b)**

Figure 5.7: The flipping-ratios for different setting of the Danfysik power supply (a), and the parabolic fit of the flipping-ratios (b).

of proportionality in the function generator. To optimize the spin-flip efficiency, the scaling constant is tuned by the same procedure as the guide field current.

After the spin-flip efficiency has been optimized, it can be calculated from four transmission measurements: two measured with the initial neutron spin state for both ^{3}He polarization states, T and T^{afp}, and another two measured with the neutron spins flipped by the RFSF, T_{sf} and T_{sf}^{afp}. The ^{3}He polarization is reversed with an AFP-flip. Two ratios are determined from these transmission measurements:

$$R_{sf} = \frac{T_{sf}^{afp} - T_{sf}}{T_{sf}^{afp} + T_{sf}} = (1 - 2\epsilon_{sf}) P_n \tanh\left(\chi \lambda P_{He}\right) \tag{5.8}$$

$$R_0 = \frac{T^{afp} - T}{T^{afp} + T} = P_n \tanh\left(\chi \lambda P_{He}\right). \tag{5.9}$$

The ratios R_{sf} and R_0 are equal to the neutron polarization after transmission through the supermirror polarizer and the polarized ^{3}He cell with the RFSF switched on and off respectively. The spin-flip efficiency can be calculated from the ratios R_{sf} and R_0 as

$$\epsilon_{sf} = \frac{1}{2}\left(1 - \frac{R_{sf}}{R_0}\right). \tag{5.10}$$

After the polarized ^{3}He transmission measurements are taken, the pedestal and (if necessary) neutron room background are subtracted from the M4 signals and the results are normalized to the signal from M1 to correct for fluctuations in the beam flux. To correct for the ^{3}He depolarization from an AFP-flip, three transmission measurements are taken and the ^{3}He polarization is reversed in between each; then the first and third transmission signals are averaged, after normalization, to give a transmission measurement that approximates the same ^{3}He polarization as after only one AFP-flip, which is valid for $\epsilon_{AFP} \approx 1$ such that $\epsilon_{AFP} \approx \frac{1+\epsilon_{AFP}^2}{2}$. For an AFP-flip efficiency of $\epsilon_{AFP} = 0.972 \pm 0.004$, the effect of the depolarization from an AFP-flip on the spin-flip efficiency is less than 0.01%, which is considered negligible. Then the spin-flip efficiency is calculated with Eqs. 5.8-5.10 for each time bin of the transmission measurements.

5.4 Neutron Polarization

The neutron polarization P_n can be calculated from three transmission measurements: the transmission through polarized ^{3}He for one neutron spin state (T given by Eq. 4.20), for the second spin state (T_{sf} given by Eq. 5.7), and the transmission through unpolarized ^{3}He (T_0 given by Eq. 4.4). The ratios of the neutron transmissions through polarized and unpolarized ^{3}He with the RFSF off and on are represented by R_1 and R_2 respectively, such that

$$
\begin{aligned}
R_1 &= \frac{T}{T_0} = \cosh(\chi\lambda P_{He})\left[1 + P_n \tanh(\chi\lambda P_{He})\right] && (5.11)\\
R_2 &= \frac{T_{sf}}{T_0} = \cosh(\chi\lambda P_{He})\left[1 + (1-2\epsilon_{sf})P_n \tanh(\chi\lambda P_{He})\right]. && (5.12)
\end{aligned}
$$

The hyperbolic identity $1 - \tanh^2 x = \mathrm{sech}^2 x$ with the substitution $x = \chi\lambda P_{He}$ gives the result

$$\tanh(\chi\lambda P_{He}) = \frac{1}{\cosh(\chi\lambda P_{He})}\sqrt{\cosh^2(\chi\lambda P_{He}) - 1}.$$

Therefore, the ratios R_1 and R_2 can be modified to depend on only the hyperbolic function $\cosh(\chi\lambda P_{He})$. Using Eqs. 5.11 & 5.12, $\cosh(\chi\lambda P_{He})$ can be solved for in terms of R_1 and R_2, such that

$$\cosh(\chi\lambda P_{He}) = \frac{1}{2\epsilon_{sf}}\left[R_2 - (1-2\epsilon_{sf})\,R_1\right]. \tag{5.13}$$

Then by making the substitutions with Eqs. 5.4 & 5.13, the ratios R_1 and R_2 can be expressed as

$$
\begin{aligned}
R_1 &= \frac{1}{2\epsilon_{sf}}\left[R_2 - (1-2\epsilon_{sf})\,R_1\right] + P_n\sqrt{\left[\frac{1}{2\epsilon_{sf}}\left[R_2 - (1-2\epsilon_{sf})\,R_1\right]\right]^2 - 1} && (5.14)\\
R_2 &= \frac{1}{2\epsilon_{sf}}\left[R_2 - (1-2\epsilon_{sf})\,R_1\right] + (1-2\epsilon_{sf})P_n\sqrt{\left[\frac{1}{2\epsilon_{sf}}\left[R_2 - (1-2\epsilon_{sf})\,R_1\right]\right]^2 - 1}, && (5.15)
\end{aligned}
$$

and from these expressions, the neutron polarization P_n can be solved for as a function of the ^{3}He transmission ratios, R_1 and R_2, and the spin-flip efficiency ϵ_{sf}, so that

$$P_n = \frac{R_1 - R_2}{\sqrt{\left[(2\epsilon_{sf}-1)R_1 + R_2\right]^2 - 4\epsilon_{sf}^2}}. \tag{5.16}$$

An important aspect of neutron polarimetry with polarized ^{3}He and a pulsed neutron beam apparent from Eq. 5.16 is that the ^{3}He polarization and the physical properties of the ^{3}He cell do not need to be known to determine the neutron polarization.

5.5 ^{3}He Cell Properties

The neutron transmission through the ^{3}He cell is dependent on several properties of the ^{3}He cell including the attenuation through the GE180 glass, the length of the ^{3}He cell, the ^{3}He number density, and the ^{3}He polarization. The techniques described earlier for characterizing the neutron beam polarization and spin-flip efficiency are independent of the properties of the ^{3}He cell because the neutron beam is pulsed and the techniques depend only on the ratios of transmission measurements at a given neutron wavelength. Nonetheless, the properties of the ^{3}He cell can also be determined from neutron transmissions measured during polarimetry measurements.

5.5.1 ^{3}He Thickness and Pressure

The ^{3}He cell thickness, $\chi \equiv \frac{n\sigma_0 l}{\lambda_0}$ from Eq. 4.5, is a constant value that incorporates several properties of the ^{3}He cell so that the neutron transmission through the unpolarized cell can be expressed as a function of the neutron wavelength by

$$T(\lambda) = T_{glass}(\lambda)e^{-\chi\lambda}, \tag{5.17}$$

where $\mathrm{T}_{glass}(\lambda)$ is the wavelength-dependent transmission through the glass of an empty cell. The thickness χ can be calculated at each wavelength with

$$\chi = \frac{1}{\lambda}\ln\left(\frac{T_{glass}(\lambda)}{T(\lambda})\right). \tag{5.18}$$

The transmission through an empty cell made of GE180 glass is approximated by correcting the transmission without a ^{3}He cell in the neutron beam by the attenuation

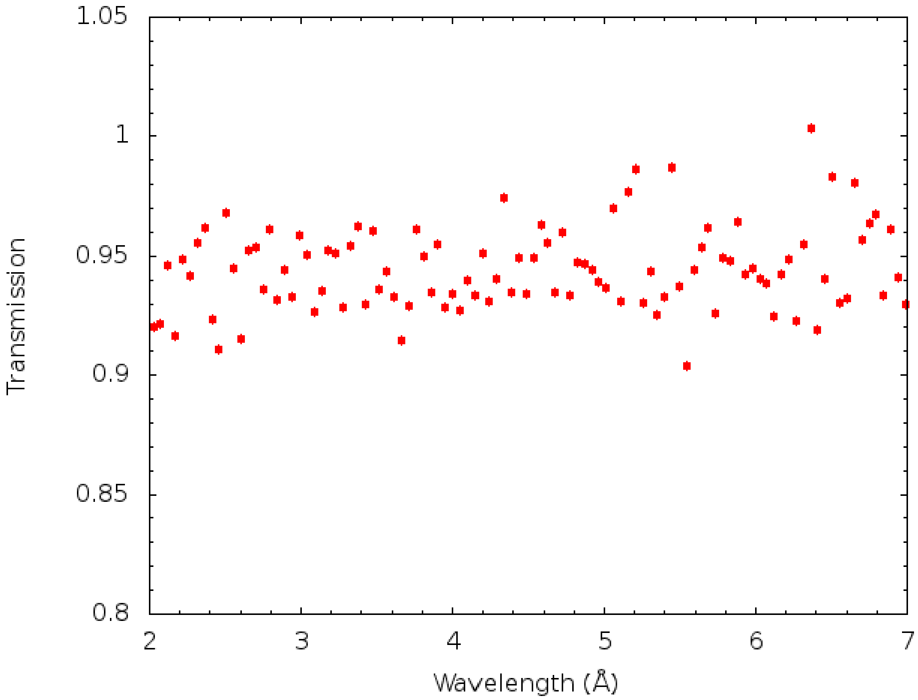

Figure 5.8: The neutron transmission through 3.175 mm of GE180 glass.

through an equivalent amount of GE180 glass. Neutron transmission of GE180 glass was measured at beamline CG-1d at HFIR through the side of a tube of 1/16 inch thick unworked GE180 glass, which equates to a total of 3.175 mm of glass. The attenuation through the glass tube is plotted in Fig. 5.8 and is relatively independent of wavelength, with a mean transmission of 0.94 ± 0.02. This result is consistent with a previous measurement of neutron transmission through GE-180 glass [55]. The walls of the ^{3}He cell are about 1.5 mm thick, so the transmission without a glass cell is corrected by a factor of 0.94.

The neutron monitor M4 is saturated without any attenuation of the neutron beam. To reduce the neutron flux on M4, the transmission measurement without the ^{3}He cell in the beamline is taken with one sheet of ^{6}Li placed directly behind the RFSF inside of the CsI detector array. The transmission measurement with the unpolarized ^{3}He cell is also taken with the ^{6}Li shielding so that the energy dependence in the neutron absorption in ^{6}Li is

Table 5.2: Uncertainties of the ^{3}He thickness.

Neutron wavelength	0.0076
GE-180 glass attenuation	0.0070
Statistical uncertainty	0.0073
Total	0.013

canceled by the ratio of the transmission measurements. The ^{6}Li shielding behind the RFSF also makes the neutron room background negligible. Moreover, the ramping of the RFSF current does not affect measurements through unpolarized ^{3}He, so the ^{3}He cell thickness can be calculated for nearly all 40 time bins.

The ^{3}He thickness has to be calculated with smaller neutron wavelengths because the transmission signal for larger wavelengths through the ^{6}Li shielding and ^{3}He cell is so small that it is comparable in size to the electronic pedestal, and there is an electronic noise in the pedestal signal that oscillates at 240 Hz. The M4 signals for transmission through ^{6}Li and ^{3}He and the pedestal are compared in Fig. 5.9. The ^{3}He cell thickness is plotted versus wavelength in Fig. 5.10, and the nonlinearities from the 240 Hz noise can be seen above 4 Å. The ^{3}He thickness of ^{3}He cell Hedy Lamarr is calculated to be 0.98 ± 0.01 Å^{-1} by averaging over wavelengths 2.7 Å to 3.4 Å. The uncertainty is due to the variance of the ^{3}He thickness at different wavelengths and the uncertainties of the GE-180 glass attenuation (0.94 ± 0.02) and neutron wavelength ($\Delta\lambda = 0.008\lambda$). The contributions of these uncertainties are given in Tab. 5.2.

The ^{3}He number density is one of the ^{3}He cell properties incorporated into the ^{3}He thickness constant, χ. The partial pressure of the ^{3}He inside the ^{3}He cell can be determined using the definition of the ^{3}He thickness (Eq. 4.5) and the ideal gas law, PV=NkT, such that

$$\mathcal{P} = \frac{kT\lambda_0\chi}{\sigma_0 l}. \tag{5.19}$$

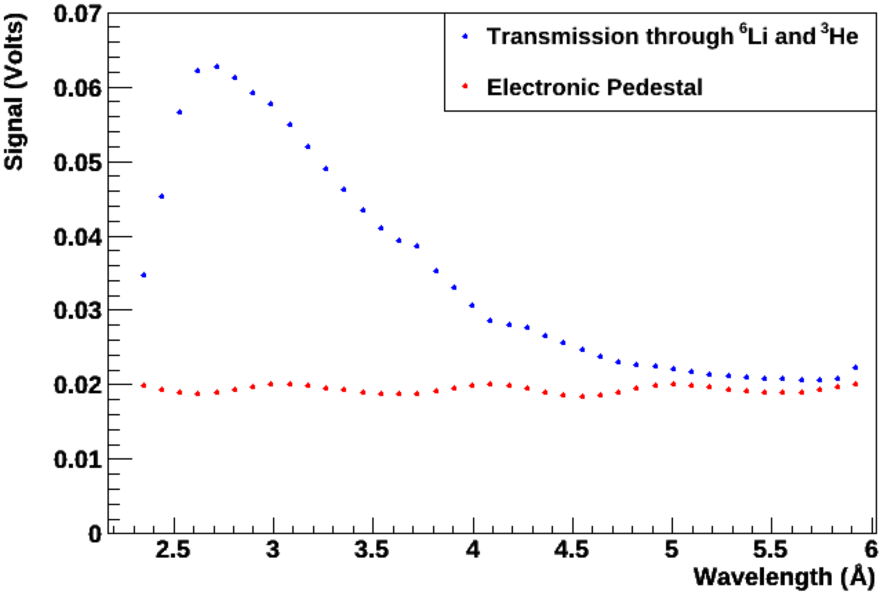

Figure 5.9: The signals from neutron monitor M4 for transmission through ^{6}Li shielding and the ^{3}He cell and the electronic pedestal.

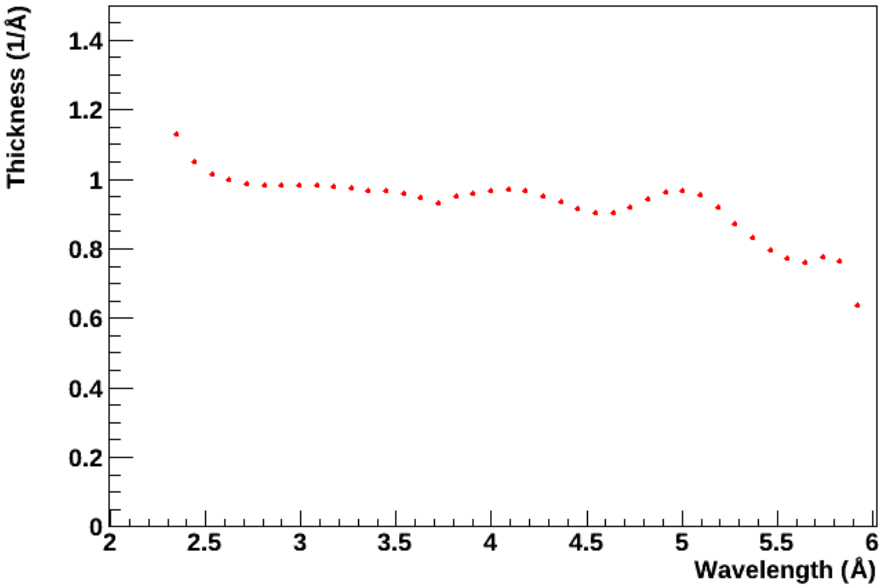

Figure 5.10: The measured ^{3}He thickness of the ^{3}He cell Hedy Lamarr versus transmitted neutron wavelength. The ^{3}He thickness should ideally be constant at every neutron wavelength; however, 240 Hz noise in the electronic pedestal causes variations in the measured ^{3}He thickness. Data points given in Tab. A.1.

The interior length of the cell is 10.2 ± 0.2 cm. Therefore at a temperature of 293 K, the ^{3}He partial pressure of the ^{3}He cell Hedy Lamarr is 1.31 ±0.03 bar.

5.5.2 ^{3}He Polarization

The ^{3}He polarization is not necessary for determining the neutron polarization or the spin-flip efficiency. However, measuring the ^{3}He polarization is a useful diagnostic for troubleshooting problems during polarimetry measurements and a method of checking the optical pumping station performance. The transmission of unpolarized neutrons through a polarized ^{3}He cell is derived from Eqs. 5.17 & 4.14, such that

$$T_{pol}(\lambda) = T_{unp}(\lambda)\cosh(\chi\lambda P_{He}), \tag{5.20}$$

where T_{pol} and T_{unp} are the transmission measurements through polarized and unpolarized ^{3}He respectively. From these two transmission measurements, the ^{3}He polarization P_{He} can be calculated by

$$P_{He} = \frac{1}{\chi\lambda}\cosh^{-1}\left(\frac{T_{pol}}{T_{unp}}\right), \tag{5.21}$$

and since the ^{3}He polarization is independent of wavelength, the variance of the ^{3}He polarizations measured at each wavelength with a pulsed neutron beam will provide the statistical uncertainty of the measurement.

The NPDGamma experiment uses a polarized neutron beam, so the transmission of an unpolarized neutron beam is approximated by averaging the M4 signals from both neutron spin states. Ideally, the average of the two neutron spin states would be corrected for the spin-flip efficiency of the RFSF, but this correction is impractical because of the many different configurations of the RFSF and the position-dependent spin-flip efficiency. Therefore, the approximation of the polarized-^{3}He transmission of unpolarized neutrons has a multiplicative

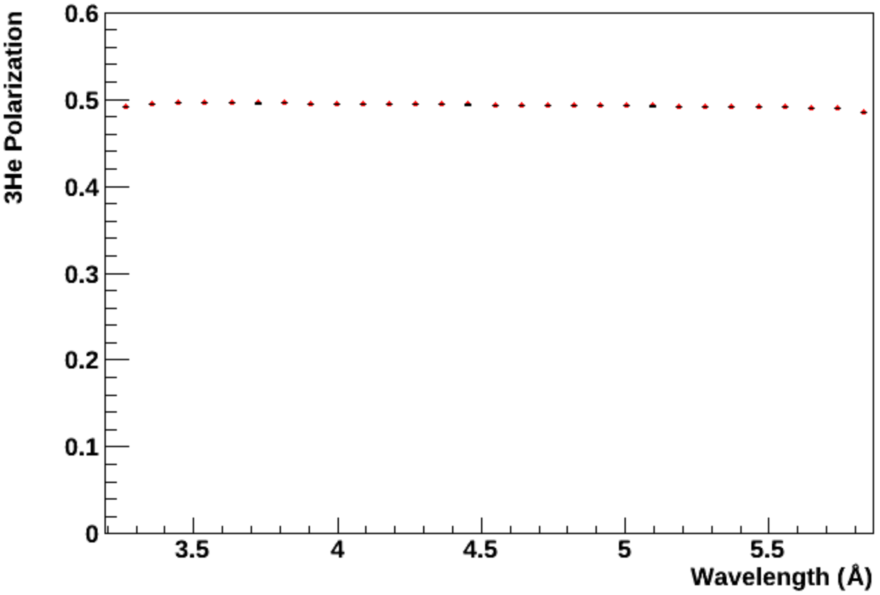

Figure 5.11: The ^{3}He polarization measured during neutron polarimetry measurements.

uncertainty of

$$\Delta T_{pol} = (1 - \epsilon_{sf}) P_n \tanh(\chi P_{He} \lambda) T_{pol}. \tag{5.22}$$

The uncertainty ΔT_{pol} is maximized with a small spin-flip efficiency and a large neutron wavelength and ^{3}He polarization, so an upper limit to the uncertainty of the polarized-^{3}He transmission in the center of the neutron beam using ϵ_{sf}=0.975, 6.5 Å neutrons, and 65% ^{3}He polarization is calculated to be $\Delta T_{pol} = 0.025 T_{pol}$. ΔT_{pol} will be larger at the edges of the neutron beam where the spin-flip efficiency is smaller. The two other significant contributions to the systematic uncertainty of the ^{3}He polarization are from the ^{3}He thickness ($\chi = 0.98 \pm 0.01$ Å^{-1}) and the neutron wavelength ($\Delta\lambda = 0.008\lambda$). During the polarimetry measurements performed to determine the beam-average neutron polarization, the maximum ^{3}He polarization is P$_{He}$=0.493 ± 0.012 averaged from 3.2-5.8 Å. The plot of ^{3}He polarization versus neutron wavelength is shown in Fig. 5.11.

5.6 Polarimetry Measurements of the Neutron Beam

Before the para-hydrogen target was installed in the NPDGamma experiment, several transmission measurements were performed with polarized ^{3}He to determine the average neutron polarization and spin-flip efficiency of the neutron beam incident on the para-hydrogen, aluminum, and chlorine capture targets. The neutron beam exiting the supermirror polarizer has a rectangular cross section 12 cm high by 10 cm wide, and the neutron beam begins to diverge downstream of the supermirror polarizer. Therefore, it is not practical to measure the transmission of the entire neutron beam through a ^{3}He cell. Instead the transmission was measured at nine positions across the neutron beam with a $\sim$5 cm diameter ^{6}Li collimator. The average polarization of the neutron beam can then be extracted by averaging the neutron polarization measured at each location weighted by the corresponding neutron flux at that location.

Transmission measurements were taken with the polarimetry apparatus mounted behind the CsI(Tl) detector array and M4 located 2.3 m downstream of the supermirror polarizer. In this configuration, the polarimetry apparatus could be mounted into several fixed positions in the neutron beam by bolting the polarimetry apparatus to a grid of bolt holes separated horizontally and vertically by 4 cm. The neutron transmission was measured at nine locations in a 3-by-3 grid with the ^{3}He cell polarized and unpolarized. In the center of the grid, additional transmission measurements were taken with multiple ^{3}He polarizations and the ^{3}He polarization flipped by AFP. The M4 signals used to determine the beam-average neutron polarization and spin-flip efficiency are corrected for the pedestal and neutron room background. Then they are normalized to the signal from M1 to correct for fluctuations in the beam flux.

5.6.1 Spin-Flip Efficiency of the RFSF

The spin-flip efficiency was measured three times at the center of the neutron beam and once 4 cm beam-right of center. The measurements in the center of the beam were performed with three different ^{3}He polarizations. The measurements of the spin-flip efficiency in these two positions are used to validate the model of the RFSF efficiency. Transmission measurements were not taken in additional locations because the performance of the RFSF is well understood and the necessary AFP-flips to determine the spin-flip efficiency depolarize the ^{3}He. The measured spin-flip efficiencies are plotted in Figs. 5.12a & 5.12b along with the expected spin-flip efficiencies at each position determined from the models of the beamline and RFSF.

The spin-flip efficiency is expected to be constant across wavelengths, so the variation in the measured spin-flip efficiency at each neutron wavelength is incorporated into the uncertainty of the spin-flip efficiency. Moreover, the uncertainty of the spin-flip efficiency determined by the model of the RFSF at positions in the neutron beam where it was not measured is approximated as the variance between the measured and simulated spin-flip efficiency at these two positions. The average spin-flip efficiency measured with a $\sim$5 cm diameter collimator is 0.995 ± 0.001 at the center of the neutron beam and 0.968 ± 0.002 beam-right of center in the wavelength range 3.5-5.8 Å.

5.6.2 Polarimetry at Multiple ^{3}He Polarizations and the Neutron Background

The neutron polarization was measured in the center of the neutron beam with the ^{3}He cell at several polarizations to confirm the measurement and diagnose possible problems, since the method of determining the neutron polarization is independent of the ^{3}He polarization. When the M4 signals for the transmission through ^{3}He are only corrected

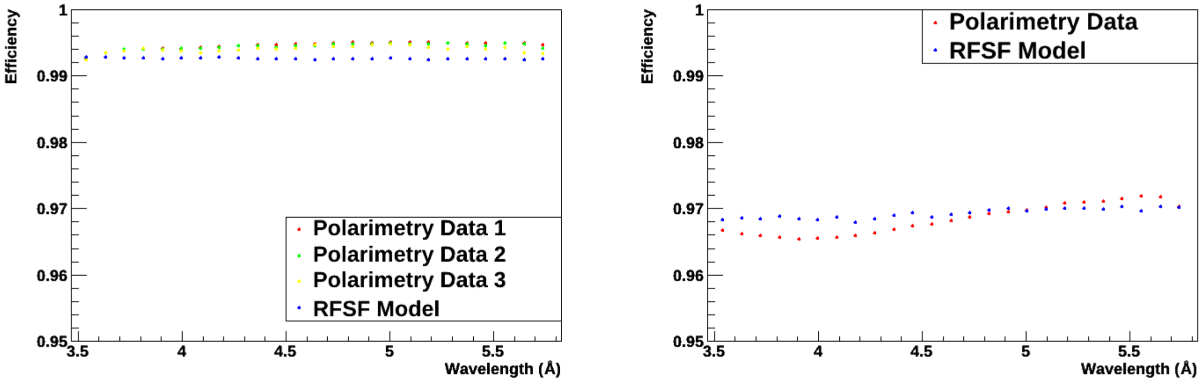

(a) (b)

Figure 5.12: The measured spin-flip efficiency compared to the RFSF and beamline models at the center of the neutron beam (a) and 4 cm beam-right of center (b). Data points given in Tabs. A.2 and A.3.

for the pedestal signal, which is measured with the secondary shutter closed, the measured neutron polarizations appear to have a dependence on the ^{3}He polarization, as shown in Fig. 5.13a. This phenomenon is consistent with a neutron room background that is only present when the secondary shutter is open. The background in the M4 signals was not discovered until after the para-hydrogen target had been installed, so it is deduced by minimizing the variance in the neutron polarizations measured with different ^{3}He polarizations. Since the spin-flip efficiency is needed to determine the neutron polarization and the M4 signals need to be corrected by the background in order to determine the spin-flip efficiency, the background is calculated until the spin-flip efficiency converged to a stable value, which required two iterations. The background is plotted against wavelength in Fig. 5.14.

After correcting the M4 signals for the background, the neutron polarizations determined with multiple ^{3}He polarizations are in agreement to within 1%, as shown in Fig. 5.13b. Transmission measurements at off-center locations in the neutron beam were only taken with one ^{3}He polarization, so it is necessary to assume that the background does not vary with the position of the polarimetry apparatus. This assumption is acceptable because the

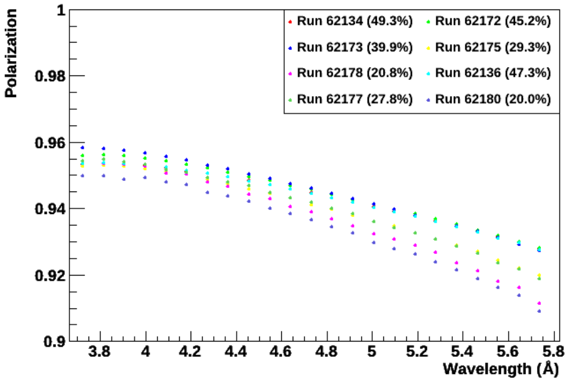

(a) **(b)**

Figure 5.13: The neutron polarization measured in the center of the neutron beam with multiple ^{3}He polarizations before (a) and after (b) background subtraction.

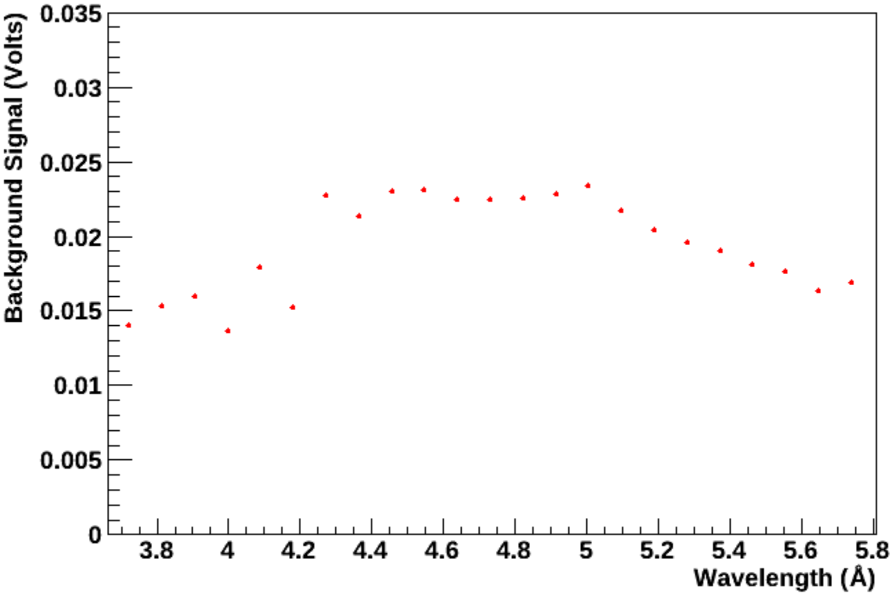

Figure 5.14: The neutron room background when polarimetry measurements were performed to determine the beam average polarization. Data points given in Tab. A.4.

neutron polarization off-center is determined from transmission through a relatively high ^{3}He polarization and is less sensitive to the background. During polarimetry measurements with the para-hydrogen target installed, the background is negligible, as the target captures most of the beam.

The measurement noise is much greater than the shot noise of counting statistics, so the uncertainty is not limited by the neutron flux; thus, the variance of the neutron polarization measurements in the center of the neutron beam is used to determine the uncertainty of the neutron polarization.

5.6.3 Neutron Polarization Measured with AFP

An equivalent method of determining the neutron polarization is to reverse the ^{3}He polarization and measure the transmission of one neutron spin state through both ^{3}He polarizations. The ^{3}He polarization is flipped by using the AFP coils on the polarimetry apparatus. Measuring the neutron polarization by reversing the ^{3}He polarization with AFP will verify the measured spin-flip efficiency of the RFSF. The effect of depolarization of ^{3}He by an AFP-flip is minimized by taking three transmission measurements with the ^{3}He polarization flipped in between each measurement and averaging the first and third transmissions as discussed in Sec. 5.3. For an AFP-flip efficiency of $\epsilon_{AFP} = 0.972 \pm 0.004$, the correction to the neutron polarization is less than 0.01%, which is considered negligible.

The neutron polarizations determined by either flipping the neutron or ^{3}He spins are shown in Fig. 5.15, and the success of determining the polarization with AFP confirms both the measured neutron polarization and spin-flip efficiency. The variance between the neutron polarizations found using these two methods, along with the results at multiple ^{3}He polarizations, is used to determine the uncertainty of the neutron polarization.

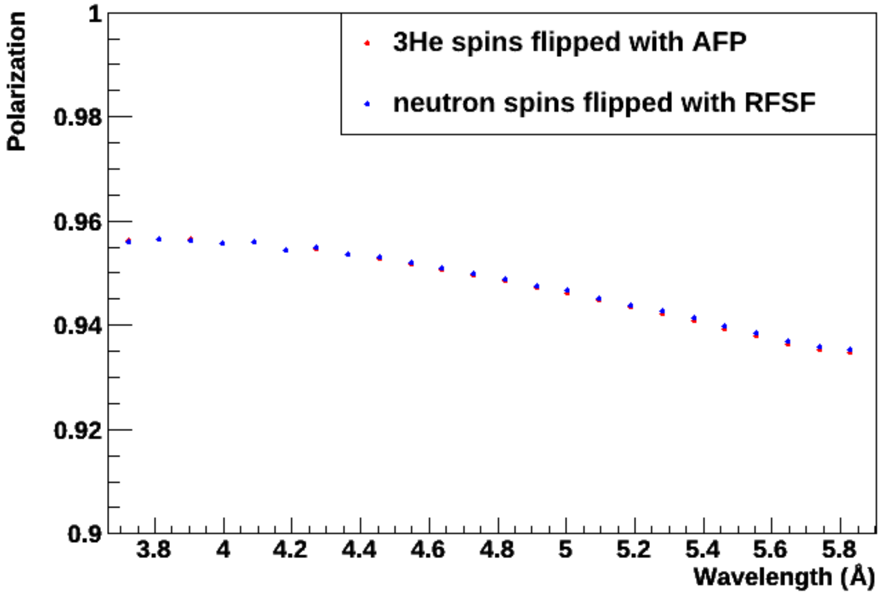

Figure 5.15: The neutron polarization determined by either flipping the neutron spins with the RFSF or the ^{3}He spins with AFP.

5.6.4 Polarimetry Measurements at Multiple Beam Positions

The neutron polarization was measured at nine positions in a 3-by-3 grid in the neutron beam, so that the beam-average polarization can be determined from a weighted average of the nine polarization measurements. The nine neutron polarizations measured are plotted in Figs. 5.16, with each plot containing the polarization measured in the same horizontal position. The neutron polarization measured on the beam-left side is lower than in the center and beam-right sections of the beam because the supermirror polarizer bends the neutron beam in the beam-right direction and neutrons that reflect at an angle less than the critical angle (expressed in Eq. 3.6) are not polarized. The critical angle increases with wavelength, so the difference in the measured polarizations is greater at large wavelengths. The neutron flux from the 45 channels of the supermirror polarizer are superimposed on each other 2.6 m downstream of the supermirror polarizer, where M4 is positioned, so the polarization observed is a composite effect of the angular-dependence of the polarization from each channel. The polarizations measured at the same horizontal position generally have the same wavelength dependence due to the approximate vertical symmetry of the supermirror polarizer. However, the manufacturing process of the supermirror polarizer does create positional variations in its performance.

The neutron polarization measured at the top beam-left position is an unphysical result produced by an anomalous transmission measurement through polarized ^{3}He. The transmission through the unpolarized ^{3}He cell resembles the transmission measured at the other beam-left locations, the only difference being a multiplicative constant. However, the polarized ^{3}He transmission is lower than expected for both neutron spin directions, especially at small wavelengths. Three measurements were taken at this position, and the anomaly was present in all of them. The cause of the anomalous transmission measurement could not be ascertained, but several possibilities have been ruled out.

The polarimetry apparatus was inspected between two of the measurements, and no abnormalities were found with the apparatus. The M1 signal shows that the beam was stable during this data run. Physical damage to the supermirror polarizer would have uniformly reduced the transmission through polarized and unpolarized ^{3}He. A poor spin-flip efficiency would have increased the transmission when the neutron and ^{3}He spins were anti-parallel rather than decrease it. A neutron absorber in the beam would have reduced the transmission signal more at larger wavelengths, but the anomaly occurs at smaller wavelengths. One possible cause that would produce the observed effect is if the polarimetry apparatus was positioned too far beam-left for the three transmission measurements at this location. The polarized neutron flux decreases away from the beam center, but there are more low-energy, unpolarized neutrons on the beam-left side because neutrons at this beam position are reflected in the supermirror polarizer at a smaller angle. However, the diameter tolerance of

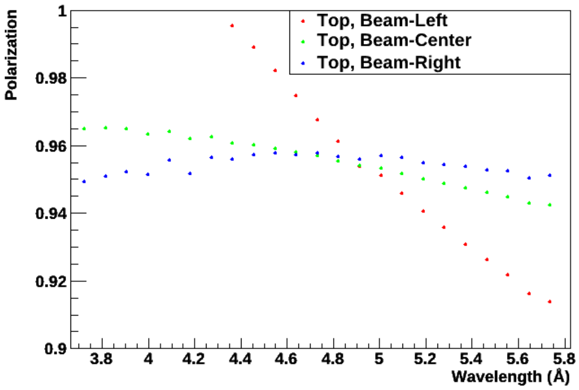

(a) Top

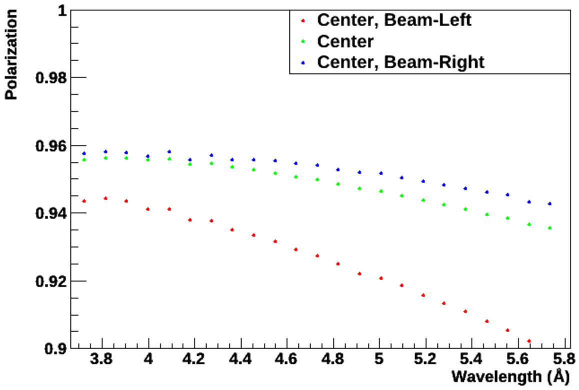

(b) Center

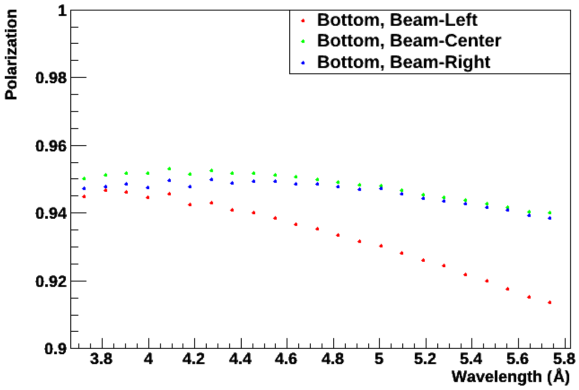

(c) Bottom

Figure 5.16: The neutron polarization measured at nine positions in the neutron beam and plotted for each vertical position. Data points given in Tabs. A.5, A.6, and A.7.

the mounting bolt holes is 0.041 cm, and simulations with the supermirror polarizer model to determine the change in neutron flux for this horizontal translation rule out the possibility the polarimetry apparatus was positioned too far beam-left. In order to determine the polarization at this beam position so that the beam-average polarization can be calculated, the results of transmission measurements performed a month earlier at the same position with a different polarimetry apparatus configuration are used and the uncertainty is adjusted accordingly.

There are two main sources of uncertainty of the neutron polarization measurements at each of the nine beam positions: the variance of multiple neutron polarization measurements and the effect of the uncertainty of the spin-flip efficiency on the neutron polarization. The standard deviation of the neutron polarization is calculated at each wavelength from eight measurements performed at several ^{3}He polarizations by either spin-flipping the neutrons with the RFSF or ^{3}He with AFP. An upper limit of the standard deviation at each wavelengths is 0.002, so it is used as a conservative estimate of the measurement uncertainty. For the upper beam-left position, the uncertainty is larger because the polarization was measured with a different polarimetry configuration. The uncertainty at that location is determined from the maximum variation between the polarization measured at two other beam positions with both configurations and is set at 0.008. The spin-flip efficiency is 0.995 ± 0.001 in the center, and 0.968 ± 0.002 beam right of center; the uncertainty of the spin-flip efficiency at all locations off-center is assumed to be equal to the uncertainty beam-right of center. The effect the uncertainty of the spin-flip efficiency has on the uncertainty of the neutron polarization is calculated via propagation of errors and ultimately leads to an uncertainty that is dependent on wavelength.

5.7 Systematic Effects

5.7.1 T_1 Relaxation Time of the ^{3}He Cell

The spin-lattice relaxation time T_1 (Sec. 4.4.1) of the ^{3}He cell in the guide field of the NPDGamma experiment is determined from the exponential fit of the amplitudes of a series of FID measurements that were taken every 30 minutes over an 18 hour time span at the FNPB. If there is no change in the ^{3}He polarization due to the FID signals, the T_1 relaxation time of the ^{3}He cell at the FNPB is 209.5 ± 5.4 hours. A plot of the FID signal amplitudes and the corresponding exponential fit is shown in Fig. 5.17. However, there is a small polarization loss due to the FID signal. The depolarization caused by the FID signals was measured with a series of five FID signals to be 0.00039 ± 0.00079; this depolarization is specific to the FID signal settings used to measure the T_1 relaxation time in the FNPB. After adjusting for a polarization loss of 0.00039 per FID signal, the T_1 relaxation time is 248.2 ± 7.6 hours. The small depolarization caused by the FID signal has a large effect on the T_1 relaxation time because the 30 minute time interval between FID signals is relatively short compared to the T_1 relaxation time. The T_1 relaxation time of 209.5 hours is used to determine the effect of relaxation of the ^{3}He polarization, since it will provide a worst case scenario and the measured depolarization from an FID signal is consistent with zero.

The time between transmission measurements of different neutron spins states when using the RFSF to flip the neutron spins is 16.67 ms, which is the time between successive neutron pulses. A T_1 relaxation time of 209.5 hours causes the ^{3}He to depolarize by a factor of 2.2×10^{-8} during the 16.67 ms time interval. The time between the successive transmission measurements varies when the ^{3}He spins are flipped by AFP but is usually less than 225 s, which causes the ^{3}He to depolarize by a factor of 3.0×10^{-4}. The effect of the T_1 relaxation time on the neutron polarization can be approximated by calculating the neutron transmissions given by Eqs. 4.4, 4.20, & 5.7 from appropriate parameters with one

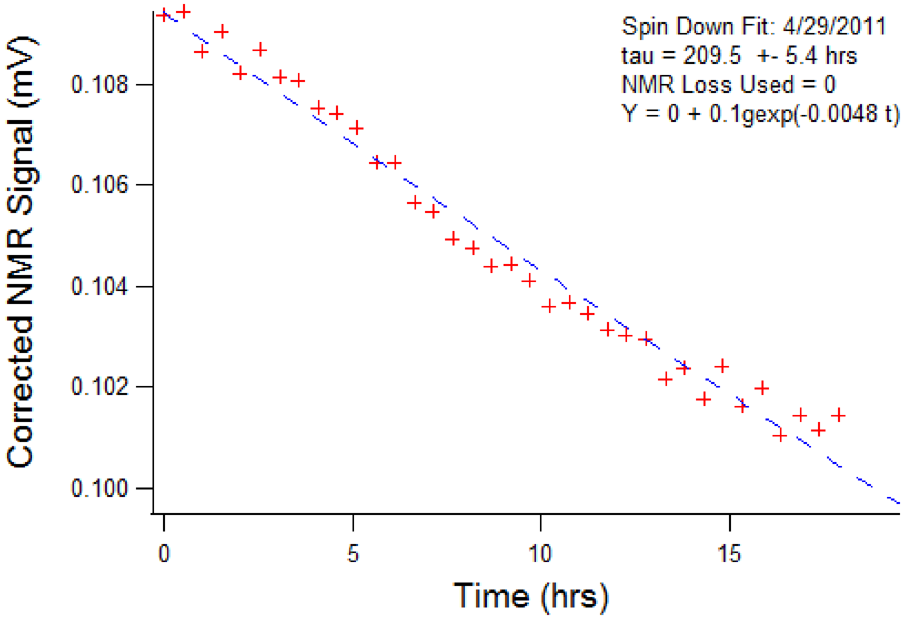

Figure 5.17: The T_1 relaxation time measured with 36 FID signals.

of the neutron transmissions through polarized ^{3}He corrected for the relaxation of the ^{3}He polarization such that

$$T(\lambda) = T_0(\lambda) e^{-\chi\lambda} \cosh\left(\chi e^{-\tau x} P_{He} \lambda\right) \left[1 + P_n \tanh\left(\chi e^{-\tau x} P_{He} \lambda\right)\right] \tag{5.23}$$

and then calculating the neutron polarization using Eq. 5.16. The effect of the T_1 relaxation time of the ^{3}He cell is an adjustment of less than 0.01% to the neutron polarization measured using either the RFSF to flip the neutron spins or AFP to flip the ^{3}He spins.

5.7.2 Incoherent Scattering on GE180 Glass

Measurements of the neutron polarization, spin-flip efficiency, and ^{3}He polarization are affected by incoherent scattering on the front wall of the ^{3}He cell because that type of scattering can flip the neutron spins before transmission through polarized ^{3}He. The glass walls of the ^{3}He cell used for polarimetry measurements are about 1.5 mm thick, and about

Table 5.3: The elemental composition of GE180 glass, and the neutron scattering cross sections in barns for those elements [56].

Element	σ_{coh}	σ_{inc}	Mass Ratio	Atomic Ratio
O	4.232	0.0008	0.431	0.639
Al	1.495	0.0082	0.076	0.238
Si	2.163	0.004	0.282	0.067
Ca	2.78	0.05	0.046	0.028
Sr	6.19	0.06	0.0021	0.027
Ba	3.23	0.15	0.163	0.00057

6% of the incident neutron beam scatters on the glass (Sec. 5.5.1). The scattering of the neutron beam on the glass cell can be approximated to first order as isotropic. The distance from the neutron monitor to the ^{3}He cell is 13 cm, and at this distance an upper limit on the ratio of scattered neutrons that are incident on the neutron monitor M2 to the total scattered neutrons is 0.009. The scattering cross sections and atomic ratios of the constituent elements of GE180 are displayed in table 5.3. The incoherent scattering cross section of the elements in GE180 glass is significantly less than the coherent scattering cross section. Because the proportion of detected scattered neutrons is small, the effect on the neutron polarization of neutrons scattering in the glass ^{3}He cell walls is less than 0.01%.

5.7.3 Neutron Scattering on ^{3}He and N_2

The ^{3}He cell contains 1.31 bar of ^{3}He and less than 0.1 bar of N_2. In addition to being captured by ^{3}He, neutrons can scatter off ^{3}He or N_2, and incoherent scattering in the ^{3}He and N_2 gases can depolarize the neutrons just like incoherent scattering in the glass walls of the ^{3}He cell. The cross section for ^{3}He and N_2 are shown in Tab. 5.4. The cross section for spin-flipping, incoherent scattering of neutrons on ^{3}He or N_2 is 0.01% of the neutron capture cross section on ^{3}He, and since the ratio of detected to total neutrons that are scattered is 0.009, the depolarization of neutrons from scattering with ^{3}He and N_2 is negligible.

Table 5.4: Neutron cross sections (expressed in barns) of ^{3}He and N_2 measured with 0.0253 eV neutrons [46, 56].

	σ_γ	σ_p	σ_s	σ_{coh}	σ_{inc}
^{3}He	3.1e-5	5316	3.1	2.48	0.62
N	0.07		10.03	9.60	0.45

5.7.4 Other Systematic Effects

The curved windows of the blown glass ^{3}He cell and coherent scattering of the neutrons in the GE180 glass, ^{3}He, and N_2 are systematic effects that do not affect the polarimetry measurements because the neutron polarization, spin-flip efficiency, and ^{3}He polarization are determined from ratios of transmission measurements through the ^{3}He cell, which cancels out the contributions of these systematic effects on the neutron transmissions. The curvature of the ^{3}He cell will affect the measurement of its ^{3}He thickness χ, which can cause a systematic correction to the ^{3}He polarization. The correction was calculated to be ~0.1% for a cylindrical ^{3}He cell with a greater curvature than the ^{3}He cell Hedy Lamarr [55]; therefore, it is a negligible effect to the measured ^{3}He thickness of Hedy Lamarr.

Neutron transmission is dependent on the ^{3}He number density (Eqs. 4.3 & 4.13), and when the ^{3}He cell is in the neutron beam, the ^{3}He number density is reduced over time as neutrons capture via the reaction $^3He + n \rightarrow p +^3 H+$ 764 keV. The quantity of ^{3}He atoms in the ^{3}He cell Hedy Lamarr is on the order of 10^{21}. The neutron flux is dependent on the proton beam power that generates the neutron pulses but is known to be on the order of 10^9 neutrons per second per cm^2, so the neutron flux through the ^{3}He cell is about 10^{10} neutrons per second. Therefore, the rate of ^{3}He removal by neutron capture has a negligible effect on neutron transmission measurements.

5.8 Beam-Average Neutron Polarization

The beam-average neutron polarization is the weighted average of the nine polarizations measured in a 3-by-3 grid in the beam and is calculated at each neutron wavelength using the expression

$$\overline{P}_n(\lambda) = \frac{\sum\limits_i w_i(\lambda) P_i(\lambda)}{\sum\limits_i w_i(\lambda)}. \tag{5.24}$$

The weights w$_i$ are proportional to the neutron flux at each position where the polarization was measured. For the beam-average polarization incident on the para-hydrogen target, the transmission measured through unpolarized ^{3}He is used as the weight because it is proportional to the neutron flux at a given wavelength. When neutron capture on the aluminum and chlorine targets was measured, a 3.5 inch diameter ^{6}Li collimator was installed in front of the RFSF (positioned 1.25 m downstream of the supermirror polarizer), so the neutron flux for each polarization measurement has to be simulated with the model of the supermirror polarizer. The main contributions to the uncertainty of the beam-average polarization come from the weights for each position, the effect of approximating the beam-average polarization with nine sample measurements, and the individual uncertainties of the measured polarization at each position. The beam-average polarization incident on the para-hydrogen target and the aluminum and chlorine targets is plotted against wavelength in Fig. 5.18 along with their uncertainties.

The McStas model of the supermirror polarizer is used to simulate the neutron flux through a 2 inch diameter collimator at each position where the neutron polarization is measured. The average weights from 4.2 to 5.8 Å determined by the simulation and the transmission through unpolarized ^{3}He are displayed in Tab. 5.5. Based on the differences between these weights, a conservative estimate of the uncertainty of the weights is set at 0.025. The effect the uncertainty of the weights has on the beam-average polarization is determined by varying the weights at each position by 0.025 and calculating the change

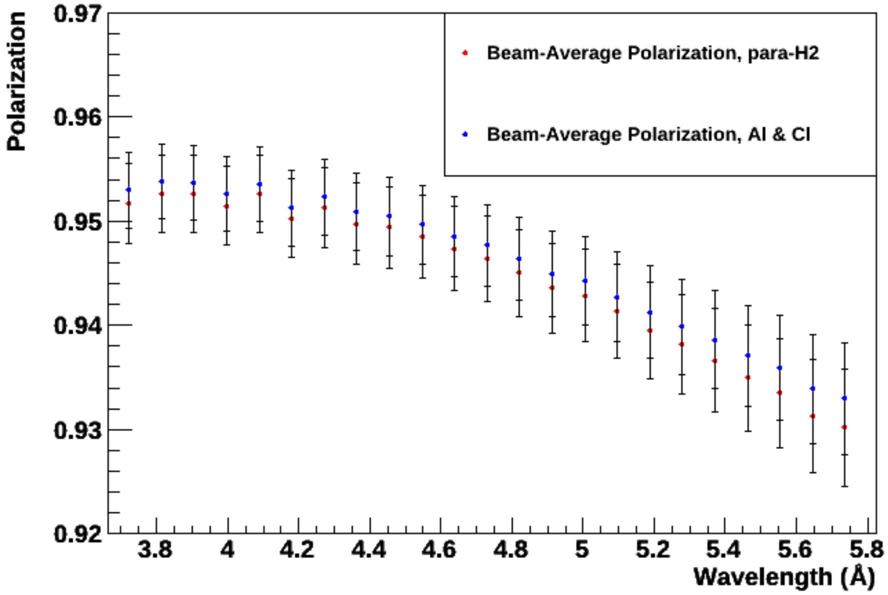

Figure 5.18: The beam-average neutron polarization incident on the para-hydrogen, aluminum, and chlorine targets. The uncertainties at each wavelength are correlated. Data points given in Tab. A.8.

in the beam-average polarization. The maximum effect on the beam-average polarization occurs when the three weights on the beam-left side are increased and beam-right side are decreased by the 0.025 uncertainty. The maximum change in the beam-average polarization is interpreted to be the uncertainty of the polarization due to the uncertainty of the weights.

Calculating the beam-average polarization from nine sampled regions in the beam is an approximation because the neutron polarization depends on position and the 2 inch diameter circular regions do not sample the entire beam area nor are they mutually exclusive. The model of the supermirror polarizer is used to simulate the neutron flux in nine rectangular sections of the beam, which represent the areas of the beam that the nine collimated measurements are sampling. Two beam-average polarizations are calculated by weighting with the simulated neutron flux in either nine 2 inch diameter circular regions or nine non-overlapping rectangular regions, and the difference is taken to be the uncertainty

Table 5.5: The weights for the neutron flux at each collimator position (averaged from 4.2 to 5.0 Å) determined from the modeled neutron flux and the measured unpolarized ^{3}He transmission, and their difference. Due to averaging, the sums of the weights do not necessarily equal 1.

Beam Position	Model Neutron Flux	Unp. ^{3}He Transmission	Difference
top, beam-left	0.09	0.07	0.02
top, beam-center	0.13	0.11	0.02
top, beam-right	0.08	0.05	0.03
center, beam-left	0.12	0.14	-0.02
center	0.17	0.19	-0.02
center, beam-right	0.11	0.12	-0.01
bottom, beam-left	0.09	0.10	-0.01
bottom, beam-center	0.13	0.14	-0.01
bottom, beam-right	0.08	0.09	-0.01

associated with approximating the total neutron polarization with nine measurements. For the aluminum and chlorine targets, both simulations incorporate the effect of the 3.5 inch collimator. This uncertainty estimate is valid because the polarization varies weakly across the neutron beam and Tab. 5.5 shows that the model of the supermirror polarizer can accurately predict the neutron flux.

Each of the nine polarization measurements has an associated uncertainty (discussed in Sec. 5.6.4) due to variations in polarization measurements and the uncertainty of the spin-flip efficiency. Because these uncertainties are produced by the same effects, they are highly correlated (correlation coefficient of ∼1), so the net uncertainty of the nine measured polarization uncertainties is their weighted average. The three uncertainties discussed above are added in quadrature to determine the total uncertainty of the beam-average polarization for each neutron wavelength.

5.9 Beam-Average Spin-Flip Efficiency

The beam-average spin-flip efficiency is the weighted average of the spin-flip efficiencies at the nine positions where the polarization was measured as determined by

$$\bar{\epsilon}_{sf}(\lambda) = \frac{\sum\limits_i w_i(\lambda) P_i(\lambda) \epsilon_i(\lambda)}{\sum\limits_i w_i(\lambda) P_i(\lambda)}. \tag{5.25}$$

The spin-flip efficiency was measured in two positions in the beam where the polarization was measured, and it is determined in the other positions using the models of the supermirror polarizer and RFSF. The spin-flip efficiency at each position is weighted by the corresponding relative neutron flux w_i and measured neutron polarization. Once again, the weight for the relative neutron flux is the transmission through unpolarized ^{3}He for the para-hydrogen target and the neutron flux simulated with the 3.5 inch collimator for the aluminum and chlorine targets. Similar to the beam-average polarization, the main contributions to the uncertainty of the beam-average spin-flip efficiency are the uncertainty of the weights for each position, the effect of approximating the beam-average spin-flip efficiency with nine samples, and the uncertainties of the spin-flip efficiency at each position. These contributions are determined by the same methods used with the beam-average polarization and added in quadrature. The uncertainty of the spin-flip efficiency measured at the center, beam-right position (determined in Sec. 5.6.1) is used as the uncertainty where the spin-flip efficiency is determined from the supermirror polarizer and RFSF models. The beam-average spin-flip efficiency for the para-hydrogen target and the aluminum and chlorine targets are plotted against wavelength in Fig. 5.19.

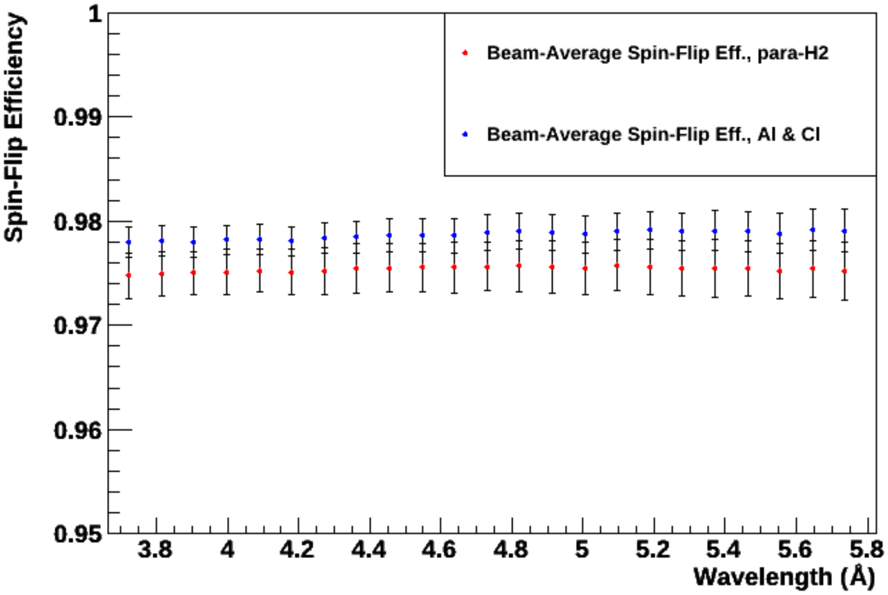

Figure 5.19: The beam-average spin-flip efficiency for the para-hydrogen, aluminum, and chlorine targets. The errors are correlated because the uncertainty of the spin-flip efficiency at each beam position is independent of wavelength. Therefore, any variation of the errors is due to uncertainties in the beam flux weights. Data points given in Tab. A.9.

5.10 Average Captured Neutron Polarization and Spin-Flip Efficiency

In order to correct the observed γ-ray asymmetry of each target (using Eq. 5.1), the average polarization and spin-flip efficiency need to be determined over the range of wavelengths of the neutrons captured. For each target the average polarization of the captured neutrons is determined by the weighted average

$$\overline{P}_n = \frac{\sum\limits_i w(\lambda_i)\sigma(\lambda_i)P_n(\lambda_i)}{\sum\limits_i w(\lambda_i)\sigma(\lambda_i)}, \tag{5.26}$$

and the average spin-flip efficiency by

$$\overline{\epsilon}_{sf} = \frac{\sum\limits_i w(\lambda_i)\sigma(\lambda_i)P_n(\lambda_i)\epsilon_{sf}(\lambda_i)}{\sum\limits_i w(\lambda_i)\sigma(\lambda_i)P_n(\lambda_i)}, \tag{5.27}$$

where $w(\lambda)$ is the neutron flux, $\sigma(\lambda)$ is the capture rate of the target, and $\mathrm{P}_n(\lambda)$ and $\epsilon_{sf}(\lambda)$ are the beam-average polarization and spin-flip efficiency of the neutron beam incident on the target. When the polarimetry measurements were performed, the opening of the chopper windows and the ramping of the RFSF current limited the range of wavelengths where a γ-ray asymmetry could be measured to 3.7 Å to 5.8 Å.

5.10.1 Target Capture Rates

The neutron polarization and spin-flip efficiency are weighted by the capture rate of the target because the observed γ-ray asymmetry depends on the polarization of the neutrons captured, not the polarization of the beam incident on the target. The capture rate is dependent on the capture cross section and geometry of the target as well as the properties of the surrounding experiment (e.g. CsI(Tl) detector array and ^{6}Li shielding). Therefore, the capture rates for the para-hydrogen, aluminum, and chlorine targets are simulated in a computational model of the NPDGamma experiment by counting the captures in the target per simulated source neutron over a range of neutron energies. The model was developed in MCNPX [57], a Monte Carlo software package that specializes in simulations of neutron transport, nuclear processes, and photon-matter interactions.

The capture rates are verified with the γ-ray signals measured in one of the CsI(Tl) detectors (i.e. detector 20 in the second ring) for neutron capture on the para-hydrogen, aluminum, chlorine, and boron targets. Because boron is a strong neutron absorber, the boron target captures essentially the entire beam, and the γ-ray signal from the boron target is proportional to the neutron flux. Thus, the ratio of the γ-ray signal for each asymmetry target to the boron capture signal is proportional to the capture rate as a function of wavelength. The voltage of the γ-ray signals for each target is dependent on the branching ratio of the neutron-capture reaction that produces a γ-ray and the energy of the emitted γ-ray, so the signal ratios are normalized to the simulated capture rates from 4.1 Å to 5.8 Å so that the capture rates and signal ratios can be compared. The simulated capture rates and the neutron-capture signal ratios are plotted against wavelength in Fig. 5.20.

The measured and simulated capture rates are consistent for the aluminum and chlorine targets. However, the para-hydrogen capture rates differ, and the simulated capture rate is greater than 1.0 at wavelengths greater than 5.2 Å, which is unphysical because the capture rate is normalized to the number of source neutrons at each wavelength. The anomaly in the simulated para-hydrogen capture rate is due to the MCNPX model tallying high energy neutrons that down-scatter before capture into low energy bins (Kyle Grammer, personal communication, March 2013). For the para-hydrogen target, the difference between the average polarization and spin-flip efficiency determined with and without weighting to the capture rate is incorporated into the uncertainty.

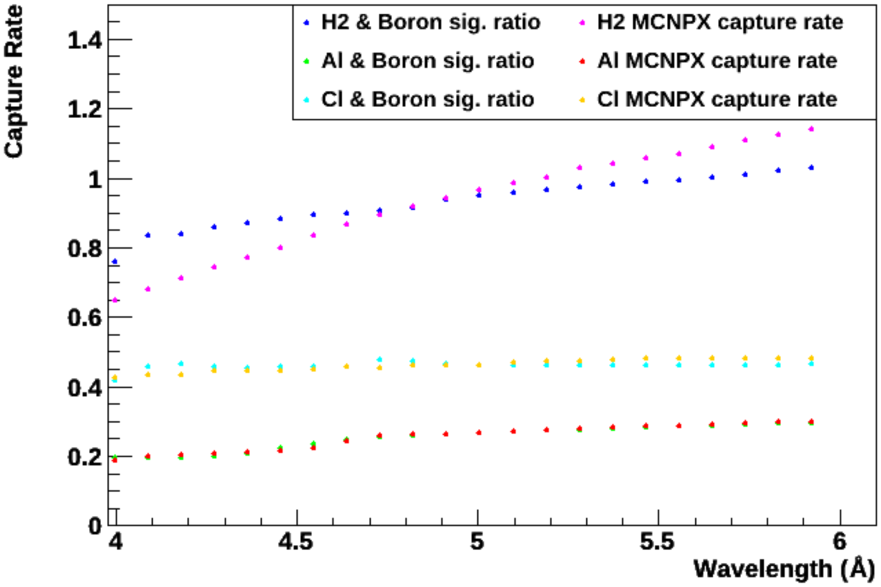

Figure 5.20: The simulated and measured capture rates of the para-hydrogen, aluminum, and chlorine targets. Data points given in Tab. A.10.

5.10.2 Neutron Flux

The neutron polarization and spin-flip efficiency are also weighted by the relative flux at each neutron wavelength where the transmission through ^{3}He was measured. Weights proportional to the neutron flux can be obtained from the McStas model of the supermirror polarizer, the γ-ray signal from neutron capture on the boron target, and the transmission through unpolarized ^{3}He measured at the nine beam positions. In order to determine the relative neutron flux at each wavelength from the transmission through unpolarized ^{3}He, the nine transmission measurements are summed and corrected for the neutron attenuation in the ^{3}He cell and efficiency of the neutron monitor M4. The neutron attenuation in the ^{3}He cell "Hedy Lamarr" is proportional to $e^{-\chi\lambda}$, where $\chi = 0.98 \pm 0.01$ Å^{-1}. M4 is 4 cm wide and has a 2 cm active region between two 1 cm dead layers, and M4 is filled with a ^{3}He density of 0.91 amagat [30]; thus, the efficiency of M4 is proportional to $e^{-\tau\lambda}(1 - e^{-2\tau\lambda})$,

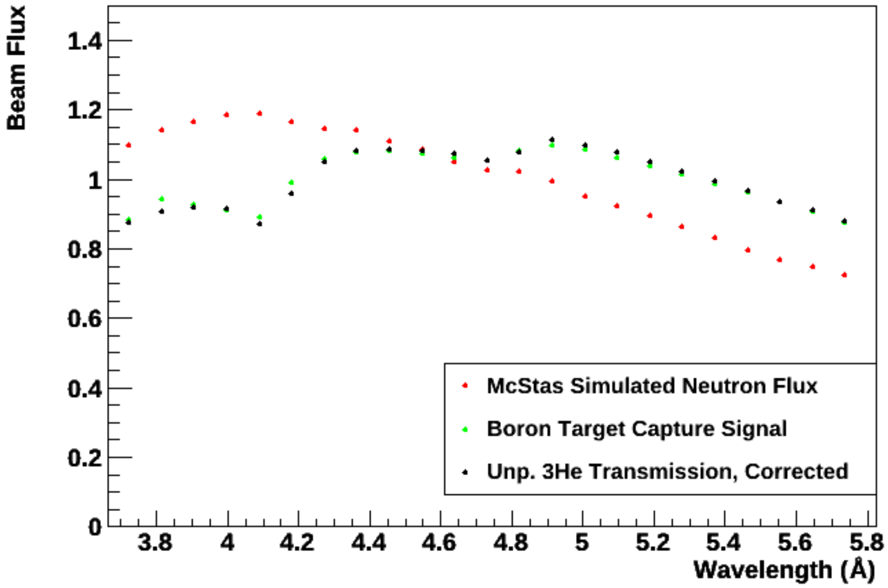

Figure 5.21: The beam-average neutron flux versus wavelength. So that each method can be compared, the flux is normalized to an average value of 1.0 within the plotted wavelength range of 3.7 Å to 5.8 Å. Data points given in Tab. A.11.

where $\tau = 0.080$ Å^{-1}. The results of each method of determining the relative neutron flux are normalized to 1.0 and plotted against wavelength in Fig. 5.21.

The measured neutron flux determined with the boron capture signals and beam-average transmission through unpolarized ^{3}He are consistent. However, the simulated neutron flux differs because the McStas model of the supermirror polarizer does not simulate aluminum Bragg scattering. The 3.5 inch ^{6}Li collimator (used with the aluminum and chlorine targets) ultimately has a negligible effect on the average polarization and spin-flip efficiency, so the same method of weighting the para-hydrogen target can be used. For each capture target, the neutron polarization and spin-flip efficiency are weighted by the neutron flux determined from transmission through unpolarized ^{3}He, and the change in the average polarization and spin-flip efficiency when weighted by the simulated neutron flux is incorporated into the uncertainty.

5.10.3 Results and Uncertainty

The average polarization and spin-flip efficiency of 3.7 Å to 5.8 Å neutrons captured on the para-hydrogen, aluminum, and chlorine targets are calculated with Eqs. 5.26 & 5.27 using the weights discussed above and are displayed in Tab. 5.6. The uncertainties of the beam-average polarization and spin-flip efficiency at each measured neutron wavelength are highly correlated because they are produced by the same effects, so their net uncertainty is their weighted average across wavelengths. The uncertainties due to the capture rate, neutron flux weight, and net uncertainty of the beam-average values are added in quadrature to get the total uncertainty of the polarization and spin-flip efficiency for each capture target, which are also displayed in Tab. 5.6.

Table 5.6: The average neutron polarization and spin-flip efficiency from 3.7-5.8 Å.

Capture Target	Neutron Polarization	Spin-Flip Efficiency
Para-Hydrogen	0.943 ± 0.004	0.975 ± 0.002
Aluminum	0.945 ± 0.004	0.979 ± 0.002
Chlorine	0.946 ± 0.004	0.979 ± 0.002

5.11 Additional Corrections for the Para-Hydrogen Target

5.11.1 Change in the Chopper Phases

After the para-hydrogen target was installed, the neutron chopper phases were changed to eliminate 13-15 Å neutrons that were leaking pass the choppers and capturing on the para-hydrogen target. Time delayed neutrons are not uniformly spin-flipped by the RFSF and create a background in the γ-ray asymmetry measurement. The change in the chopper phases caused a change in the range of wavelengths of the neutrons captured on the para-hydrogen target such that the γ-ray asymmetry is now measured with 4.1 Å to 6.8 Å neutrons. Therefore, the average polarization of the captured neutrons has to be recalculated for the new wavelength range. The spin-flip efficiency is relatively independent of the neutron wavelength and is assumed to be unaffected.

Another set of polarimetry measurements of the neutron beam could not be performed because the para-hydrogen target vessel had been installed in the experiment before the chopper phases were changed. Therefore, the beam-average polarization determined with the first set of chopper phases needs to be extrapolated to larger wavelengths. The extrapolation cannot be performed with the neutron polarization measured though the ~1.75 cm diameter neutron window in the para-hydrogen target because the M4 monitor is located too far behind the CsI(Tl) detector array to measure the whole wavelength range. The McStas model of the supermirror polarizer consistently predicts a neutron polarization larger than what is measured; however, it does accurately simulate the wavelength-dependence of the polarization. The difference between the measured and simulated polarization between 3.7 Å to 5.8 Å is fitted to a second-order polynomial with the result

$$P_{model}(\lambda) - P_{obs}(\lambda) = 0.055 - 0.012\lambda + 0.001\lambda^2. \tag{5.28}$$

Then the polarization at larger wavelengths is extrapolated by reducing the simulated polarization by the expected difference at each wavelength. The simulated, measured, and extrapolated neutron polarization incident on the para-hydrogen target are plotted against wavelength in Fig. 5.22 as well as the polarization measured through the window in the empty para-hydrogen target vessel on Jan. 2013 to verify some of the extrapolated values. The uncertainty of the polarization at each of the extrapolated values is estimated as the

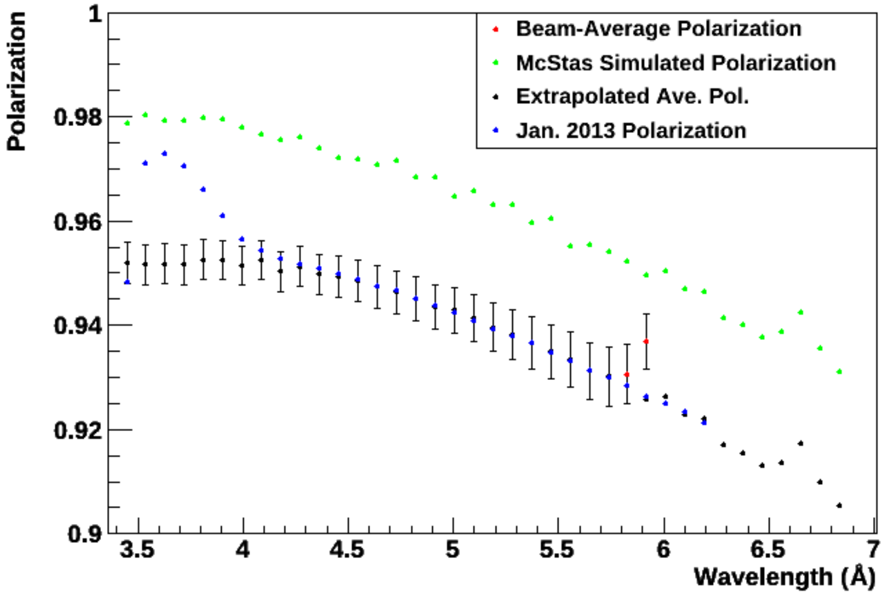

Figure 5.22: The measured beam-average polarization (red), the simulated polarization from the McStas (green), the beam-average polarization extrapolated out to 6.8 Å (black), and the polarization measured with the new chopper phases in Jan. 2013 (blue). Data points given in Tab. A.12.

maximum uncertainty of the measured polarization per wavelength added in quadrature with an uncertainty due to the extrapolation.

The average polarization of the neutrons captured from 4.1 Å to 6.8 Å is calculated using Eq. 5.26 to determine the weighted average. The relative neutron flux at each wavelength is extrapolated from the simulated neutron flux between 5.0 Å and 5.8 Å by the same procedure used to extrapolate the polarization. This extrapolation is done because the McStas model does not account for the change in neutron flux due to Al Bragg scattering, as can be seen in Fig. 5.21. The capture rates are determined from the MCNPX model of the experiment for the new wavelength range. The average polarization of neutrons captured in the para-hydrogen target with the newer chopper phases is 0.934 ± 0.005.

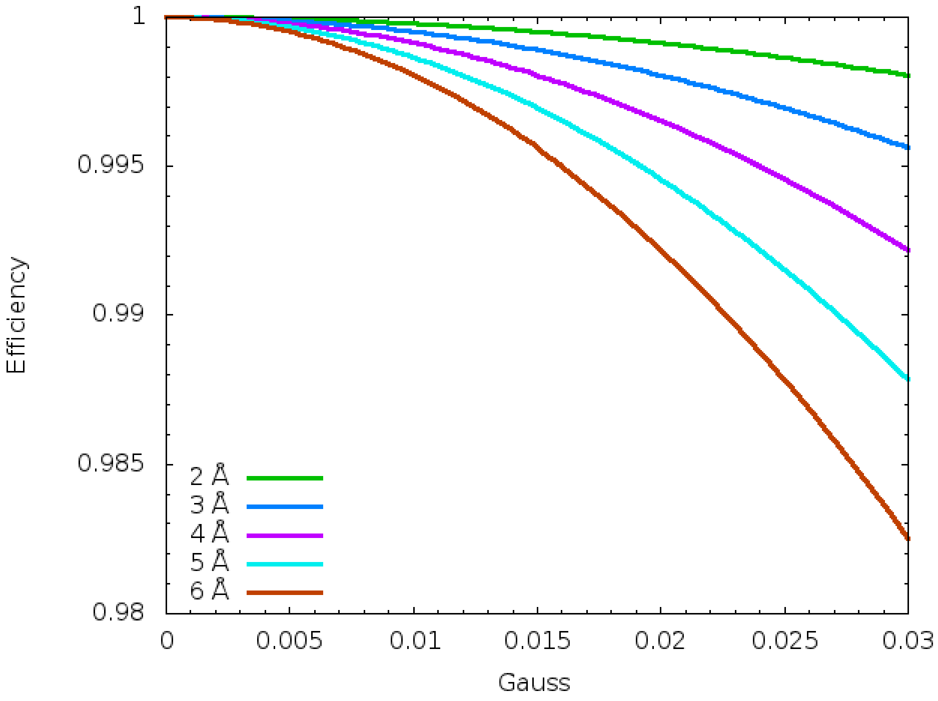

Figure 5.23: The spin-flip efficiency at different neutron wavelengths plotted against a change in the magnetic field away from resonance. This plot assumes an initially perfect spin-flip efficiency.

5.11.2 Magnetic Field Stability

The NPDGamma experiment relies on the RFSF to consistently reverse the neutron spins with a high efficiency during the runtime of the experiment. The probability of a neutron spin-flip is dependent on the magnitude of the guide field in the vertical direction, and the effect of the magnetic field being out of resonance with the RFSF is shown in Fig. 5.23 for several neutron wavelengths. This effect is calculated using Eq. 3.14. Therefore, the guide field is continuously monitored with two flux-gate magnetometers mounted above and below the RFSF to ensure that the guide field stays at the resonance value.

The magnetic field in the vertical direction measured over an eight month period is plotted in Fig. 5.24. The variations in the measured field strength are large enough that they can create significant variations in the spin-flip efficiency. However, the drifts in the measured magnetic field over time are inconsistent between the two magnetometers, so it is inferred that the gains of the magnetometers vary with time. Multiple polarimetry measurements to tune the guide field have confirmed that the magnetic field is always at or near the optimal current setting to achieve resonance, as shown in Tab. 5.7.

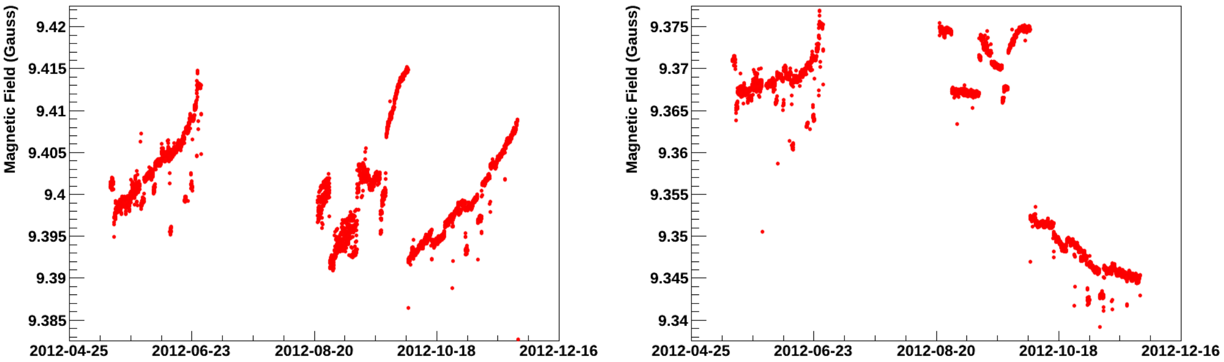

(a) Magnetometer 1

(b) Magnetometer 2

Figure 5.24: The guide field in the vertical direction from April to December 2012. The field is measured with the two magnetometers mounted on the RFSF.

Table 5.7: The results of polarimetry measurements to optimize the spin-flip efficiency by tuning the guide field.

Date	Danfysik Current (Amps)	Guide Field (Gauss)
2012/8/29	23.10	9.405
2013/1/8	23.08	9.398
2013/2/26	23.06	9.386
2013/4/12	23.06	9.377
2013/5/29	23.06	9.372
2013/8/13	23.05	9.368

There are occasionally sudden fluctuations in the guide field on the order of ∼0.01 Gauss, which are measured by both magnetometers, so the effect of a 0.01 Gauss deviation of the guide field away from resonance is calculated by a weighted average over the wavelengths 4.1 Å to 6.8 Å using Eq. 5.27. A 0.01 Gauss deviation in the guide field could change to average spin-flip efficiency by a factor of ∼0.995. After the effect of magnetic field stability is incorporated into the uncertainty, the spin-flip efficiency of the neutrons captured on the para-hydrogen target is 0.975 ± 0.003.

Chapter 6

Conclusion

The goal of the NPDGamma experiment is to measure the γ-ray asymmetry from the capture of cold neutrons on protons (via the reaction $\vec{n}+p \rightarrow d+\gamma$) to a precision of 1×10^{-8}. In order to minimize systematic uncertainties so that this precision can be achieved, the neutron polarization and spin-flip efficiency are measured to a precision significantly better than the expected statistical uncertainty of the NPDGamma experiment. The results of polarimetry measurements are shown in Tab. 5.6 for the para-hydrogen, aluminum, and chlorine targets, and they are within their goal uncertainty of 2%. For the γ-ray asymmetry of neutron capture on para-hydrogen, the sources of uncertainty in the measured neutron polarization and spin-flip efficiency are shown in Tab. 6.1.

The neutron polarization and spin-flip efficiency used to correct the observed γ-ray asymmetry will ultimately depend on the neutron wavelengths that are used to measure the γ-ray asymmetry. For neutron capture on para-hydrogen, it is expected that wavelengths between 4.1 Å and 6.8 Å will be used. For this range, the recommended neutron polarization and spin-flip efficiency are given in Tab. 6.2.

While the NPDGamma experiment is running, neutron polarimetry with polarized ^{3}He is routinely performed in order to verify that the supermirror polarizer and RFSF are operating

Table 6.1: Uncertainties of the beam-average neutron polarization and spin-flip efficiency from 3.7-5.8 Å for the hydrogen target.

Source of Uncertainty	Neutron Polarization	Spin-flip Efficiency
Uncertainty of spin-flip efficiency	0.003	N/A
Stability of guide field	N/A	0.001
Variance of measurements	0.002	0.001
Position-dependent flux for weighted average	0.001	0.001
Uncertainty of target capture rate	0.0006	<0.0001
Wavelength-dependent flux for weighted average	0.0005	<0.0001
Approximating the beam with 9 measurements	0.0001	0.002
AFP-flip efficiency	<0.0001	<0.0001
Relaxation of ^{3}He polarization	<0.0001	<0.0001
Incoherent scattering on GE180 glass	<0.0001	<0.0001
Spin-flip scattering on ^{3}He and N_2	<0.0001	<0.0001
Neutron absorption on ^{3}He	<0.0001	<0.0001
Total uncertainty	0.004	0.003

Table 6.2: The 4.1 Å to 6.8 Å.

Capture Target	Neutron Polarization	Spin-Flip Efficiency
Para-Hydrogen	0.934 ± 0.005	0.975 ± 0.003

as expected. Polarimetry measurements with para-hydrogen in the neutron beam have low counting statistics that cannot be used to determine the neutron polarization to the same precision measured during commissioning of the NPDGamma experiment. However, polarimetry has been performed during periods when the para-hydrogen target vessel is empty. Two neutron polarization measurements taken during operation of the NPDGamma experiment are plotted against wavelength in Fig. 6.1 along with the polarization measured in the center of the beam before the para-hydrogen target was installed. The polarization appears to be stable before and during the operation of the NPDGamma experiment.

The neutron room background is the largest source of uncertainty in the beam-average neutron polarization due to the difficulty in determining it (discussed in Sec. 5.6.2). In the

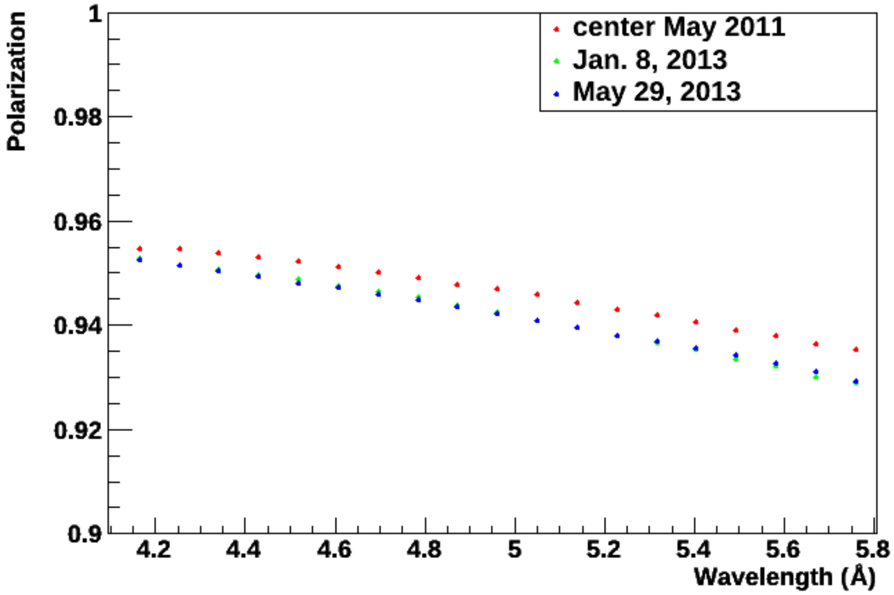

Figure 6.1: The measured neutron polarization during the running of the NPDGamma experiment with the hydrogen target vessel empty. Data points given in Tab. A.13.

future, neutron polarization measurements could be improved by reducing the neutron room background or by making a precision measurement of the background at each collimator position. The accuracy of the beam-average polarization could also be improved by measuring the beam polarization with either a large ^{3}He cell that intersects the entire beam or with non-overlapping square cross-sections of the beam with a small ^{3}He cell to prevent double sampling of part of the beam.

Bibliography

[1] Jeffrey S. Nico and W. Michael Snow. Fundamental Neutron Physics. *Annual Review of Nuclear and Particle Science*, 55(1):27–69, December 2005. ISSN 0163-8998. doi: 10.1146/annurev.nucl.55.090704.151611. URL `http://www.annualreviews.org/doi/abs/10.1146/annurev.nucl.55.090704.151611`. 1

[2] J.F. Cavaignac, B. Vignon, and Richard Wilson. Search for parity violation in neutron-proton capture. *Physics Letters B*, 67(2):148–150, March 1977. ISSN 03702693. doi: 10.1016/0370-2693(77)90088-0. URL `http://linkinghub.elsevier.com/retrieve/pii/0370269377900880`. 2, 10

[3] M. Gericke, R. Alarcon, S. Balascuta, L. Barrón-Palos, C. Blessinger, J. Bowman, R. Carlini, W. Chen, T. Chupp, C. Crawford, S. Covrig, M. Dabaghyan, N. Fomin, S. Freedman, T. Gentile, R. Gillis, G. Greene, F. Hersman, T. Ino, G. Jones, B. Lauss, M. Leuschner, W. Lozowski, R. Mahurin, Y. Masuda, J. Mei, G. Mitchell, S. Muto, H. Nann, S. Page, S. Penttilä, W. Ramsay, a. Salas-Bacci, S. Santra, M. Sharma, P.-N. Seo, E. Sharapov, T. Smith, W. Snow, W. Wilburn, and V. Yuan. Measurement of parity-violating γ-ray asymmetry in the capture of polarized cold neutrons on protons. *Physical Review C*, 83(1):1–18, January 2011. ISSN 0556-2813. doi: 10.1103/PhysRevC.83.015505. URL `http://link.aps.org/doi/10.1103/PhysRevC.83.015505`. 2, 10

[4] BG Erozolimskii and IA Kuznetsov. New measurements of the electron-neutron spin asymmetry in neutron beta-decay. *Physics Letters B*, 263(1):33–38, 1991. URL `http://www.sciencedirect.com/science/article/pii/037026939191703X`. 3

[5] A P Serebrov, A V Aldushchenkov, M S Lasakov, I A Kuznetsov, and I V Stepanenko. New method for precise determination of neutron beam polarization. *Nuclear Instruments and Methods in Physics Research Section A: Accelerators, Spectrometers, Detectors and Associated Equipment*, 357:503–510, 1995. ISSN 1539-2570. 3

[6] G Greene, A K Thompson, and M S Dewey. A method for the accurate determination of the polarization of a neutron beam using a polarized 3He spin filter. *Nuclear Instruments and Methods in Physics Research Section A: Accelerators, Spectrometers, Detectors and Associated Equipment*, 356(2-3):177–180, March 1995. ISSN 01689002. doi: 10.1016/0168-9002(94)01249-0. URL http://linkinghub.elsevier.com/retrieve/pii/0168900294012490. 3

[7] M. Bouchiat, T. Carver, and C. Varnum. Nuclear Polarization in He^{3} Gas Induced by Optical Pumping and Dipolar Exchange. *Physical Review Letters*, 5(8):373–375, October 1960. ISSN 0031-9007. doi: 10.1103/PhysRevLett.5.373. URL http://link.aps.org/doi/10.1103/PhysRevLett.5.373. 3, 44

[8] T. Chupp, M. Wagshul, K. Coulter, A. McDonald, and W. Happer. Polarized, high-density, gaseous He3 targets. *Physical Review C*, 36(6):2244–2251, December 1987. ISSN 0556-2813. doi: 10.1103/PhysRevC.36.2244. URL http://link.aps.org/doi/10.1103/PhysRevC.36.2244. 46

[9] Thad G Walker and William Happer. Spin-exchange optical pumping of noble-gas nuclei. *Reviews of Modern Physics*, 69(2):629–642, April 1997. ISSN 0034-6861. doi: 10.1103/RevModPhys.69.629. URL http://link.aps.org/doi/10.1103/RevModPhys.69.629. 3, 44

[10] E. Fermi. Versuch einer theorie der -strahlen. i. *Zeitschrift fr Physik*, 88(3-4):161–177, 1934. ISSN 0044-3328. doi: 10.1007/BF01351864. URL http://dx.doi.org/10.1007/BF01351864. 5

[11] Bertrand Desplanques, J.F. Donoghue, and B.R. Holstein. Unified treatment of the parity violating nuclear force. *Annals of Physics*, 124(2):449–495, 1980. ISSN 0003-4916. URL http://linkinghub.elsevier.com/retrieve/pii/0003491680902171. 5

[12] T. Lee and C. Yang. Question of Parity Conservation in Weak Interactions. *Physical Review*, 104(1):254–258, October 1956. ISSN 0031-899X. doi: 10.1103/PhysRev.104.254. URL http://link.aps.org/doi/10.1103/PhysRev.104.254http://iktp.tu-dresden.de/uploads/media/Parity_conservation_in_weak_interactions_-_Lee_Yang.pdf. 8

[13] C. S. Wu. Experimental Test of Parity Conservation in Beta Decay. *Physical Review*, 105(4):1413–1415, February 1957. ISSN 0031-899X. doi: 10.1103/PhysRev.105.1413. URL http://link.aps.org/doi/10.1103/PhysRev.105.1413. 8

[14] G. Barton. Notes on the static parity non-conserving internucleon potential. *Il Nuovo Cimento Series 10*, 19(3):512–527, 1961. ISSN 0029-6341. doi: 10.1007/BF02733247. URL http://dx.doi.org/10.1007/BF02733247. 9

[15] Y Masuda, J D Bowman, R D Carlini, T Case, T E Chupp, K P Coulter, S J Freedman, T R Gentile, M Gericke, G L Greene, F W Hersmann, T Ino, S Ishimoto, G L Jones, M B Leuschner, G S Mitchell, K Morimoto, S Muto, H Nann, S A Page, S I Penttila, W D Ramsay, E I Sharapov, T B Smith, W M Snow, S W Wilburn, and Y W Yuan. Parity-violating gamma-ray asymmetry in the neutron-proton capture. *Nuclear Physics A*, 721:485–488, 2003. 9

[16] Michael J. Ramsey-Musolf and Shelley a. Page. Hadronic Parity Violation: A New View Through the Looking Glass. *Annual Review of Nuclear and Particle Science*, 56(1):1–52, November 2006. ISSN 0163-8998. doi: 10.1146/annurev.nucl.54.070103.181255. URL http://www.annualreviews.org/doi/abs/10.1146/annurev.nucl.54.070103.181255. 10

[17] Joseph Wasem. Lattice QCD calculation of nuclear parity violation. *Physical Review C*, 85(2):022501, February 2012. ISSN 0556-2813. doi: 10.1103/PhysRevC.

85.022501. URL http://arxiv.org/abs/1108.1151http://link.aps.org/doi/10.1103/PhysRevC.85.022501. 10

[18] EG Adelberger and WC Haxion. Parity violation in the nucleon-nucleon interaction. *Annual Review of Nuclear and Particle Science*, 35(1):501–558, 1985. ISSN 0163-8998. URL http://www.annualreviews.org/doi/full/10.1146/annurev.ns.35.120185.002441. 10

[19] C. S. Wood. Measurement of Parity Nonconservation and an Anapole Moment in Cesium. *Science*, 275(5307):1759–1763, March 1997. ISSN 00368075. doi: 10.1126/science.275.5307.1759. URL http://www.sciencemag.org/cgi/doi/10.1126/science.275.5307.1759. 10

[20] T.E. Mason, D. Abernathy, I. Anderson, J. Ankner, T. Egami, G. Ehlers, a. Ekkebus, G. Granroth, M. Hagen, K. Herwig, J. Hodges, C. Hoffmann, C. Horak, L. Horton, F. Klose, J. Larese, a. Mesecar, D. Myles, J. Neuefeind, M. Ohl, C. Tulk, X-L. Wang, and J. Zhao. The Spallation Neutron Source in Oak Ridge: A powerful tool for materials research. *Physica B: Condensed Matter*, 385-386(2006):955–960, November 2006. ISSN 09214526. doi: 10.1016/j.physb.2006.05.281. URL http://linkinghub.elsevier.com/retrieve/pii/S092145260601177X. 12

[21] SNS Parameters List. Technical Report June, 2005. URL http://neutrons.ornl.gov/media/pubs/pdf/sns_parameters_list_june05.pdf. 12

[22] R W Shaw, M A Plum, L L Wilson, Oak Ridge, C S Feigerle, M J Borden, T Spickermann, Los Alamos, Y Irie, I Sugai, and A Takagi. SPALLATION NEUTRON SOURCE (SNS) DIAMOND STRIPPER FOIL DEVELOPMENT. *Proceedings of PAC2007*, (2):620–622, 2007. 14

[23] N. Fomin. Fundamental neutron physics beamline at the spallation neutron source at ornl. Technical report, 2013. Manuscript in preparation. 15

[24] J. Orear and E. Fermi. *Nuclear Physics: A Course Given by Enrico Fermi at the University of Chicago*. Midway reprint. University of Chicago Press, 1950. ISBN 9780226243658. URL `http://books.google.com/books?id=WQtkYCWTcicC`. 17

[25] VF Turchin. Diffraction of slow neutrons by stratified systems. *Atomic Energy*, 22 (2):124–125, 1967. ISSN 1063-4258. URL `http://www.springerlink.com/index/j0526292q12430g9.pdf`. 19

[26] F. Mezei. Novel polarized neutron devices: supermirror and spin component amplifier. *Commun. Phys*, 1:81–85, 1976. URL `http://scholar.google.com/scholar?hl=en&btnG=Search&q=intitle:Novel+polarized+neutron+devices:+supermirror+and+spin+component+amplifier#0`. 19, 24

[27] O. Schaerpf. Comparison of theoretical and experimental behaviour of supermirrors and discussion of limitations. *Physica B: Condensed Matter*, 156-157:631–638, January 1989. ISSN 09214526. doi: 10.1016/0921-4526(89)90750-3. URL `http://linkinghub.elsevier.com/retrieve/pii/0921452689907503`. 19, 24

[28] R. Mahurin and C. Crawford. Opening angles for the sns fnpb choppers. Technical report, 2006. URL `http://battlestar.phys.utk.edu/wiki/images/3/38/SNS_choppers_opening_angles.pdf`. 20, 69

[29] M. McCrea. Npdgamma neutron beam monitors at fnpb. Technical report, 2013. Manuscript in preparation. 23

[30] L. Barron. Efficiency of the triple monitor. Technical report, 2011. Technical Report. 23, 104

[31] O Schaerpf. Properties of beam bender type neutron polarizers using supermirrors. *Physica B: Condensed Matter*, 156-157:639–646, February 1989. ISSN 09214526. doi: 10.1016/0921-4526(89)90751-5. URL http://linkinghub.elsevier.com/retrieve/pii/0921452689907515. 24

[32] C. Crawford. Supermirror polarizer for the fnpb cold line. Technical report, 2007. 24, 70

[33] Balascuta S. Schaedler, J. and S. Baessler. Technical report on the mapping of the magnetic field for the npdgamma experiment at fnpb13 spallation neutron source, ornl. Technical report, 2010. 26

[34] G. Greene. Measurement of the neutron magnetic moment. *Physical Review D*, 2(9): 663–2153, November 1979. doi: 10.1103/PhysRevD.20.2139. 26

[35] Vector Fields Software Cobham Technical Services. *Opera-3d User Guide, Version 15R3*, 2012. 27

[36] S. Balascuta. The transport of the neutrons through the magnetic field of the npdgamma experiment. Technical report, 2010. Technical Report. 27

[37] P.-N. Seo, L. Barrón-Palos, J. Bowman, T. Chupp, C. Crawford, M. Dabaghyan, M. Dawkins, S. Freedman, T. Gentile, M. Gericke, R. Gillis, G. Greene, F. Hersman, G. Jones, M. Kandes, S. Lamoreaux, B. Lauss, M. Leuschner, R. Mahurin, M. Mason, J. Mei, G. Mitchell, H. Nann, S. Page, S. Penttilä, W. Ramsay, a. Salas Bacci, S. Santra, M. Sharma, T. Smith, W. Snow, W. Wilburn, and H. Zhu. High-efficiency resonant rf spin rotator with broad phase space acceptance for pulsed polarized cold neutron beams. *Physical Review Special Topics - Accelerators and Beams*, 11(8):1–15, August 2008. ISSN 1098-4402. doi: 10.1103/PhysRevSTAB.11.084701. URL http://link.aps.org/doi/10.1103/PhysRevSTAB.11.084701. 29, 30, 72

[38] J. Byrne. *Neutrons, Nuclei, and Matter: An Exploration of the Physics of Slow Neutrons.* Institute of Physics Pub., 1994. ISBN 9780750302647. URL `http://books.google.com/books?id=Oa-yAAAAIAAJ`. 30

[39] S. Santra, L. Barrón Palos, C. Blessinger, J.D. Bowman, T.E. Chupp, S. Covrig, C. Crawford, M. Dabaghyan, J. Dadras, and M. Dawkins. A liquid parahydrogen target for the measurement of a parity-violating gamma asymmetry in n+pd+γ. *Nuclear Instruments and Methods in Physics Research Section A: Accelerators, Spectrometers, Detectors and Associated Equipment*, 620(2-3):421–436, August 2010. ISSN 01689002. doi: 10.1016/j.nima.2010.04.135. URL `http://linkinghub.elsevier.com/retrieve/pii/S0168900210009897`. 31

[40] E. Ilisca and S. Paris. Magnetic Field Acceleration of the ortho-para H2 Conversion on Transition Oxides. *Physical Review Letters*, 82(8):1788–1791, February 1999. ISSN 0031-9007. doi: 10.1103/PhysRevLett.82.1788. URL `http://link.aps.org/doi/10.1103/PhysRevLett.82.1788`. 32

[41] G.S Mitchell, C.S Blessinger, J.D Bowman, T.E Chupp, K.P Coulter, M Gericke, G.L Jones, M.B Leuschner, H Nann, S.a Page, S.I Penttilä, T.B Smith, W.M Snow, and W.S Wilburn. A measurement of parity-violating gamma-ray asymmetries in polarized cold neutron capture on , , and. *Nuclear Instruments and Methods in Physics Research Section A: Accelerators, Spectrometers, Detectors and Associated Equipment*, 521(2-3): 468–479, April 2004. ISSN 01689002. doi: 10.1016/j.nima.2003.11.192. URL `http://linkinghub.elsevier.com/retrieve/pii/S0168900203030961`. 33

[42] M Avenier, G Bagieu, H Benkoula, J.F. Cavaignac, A Idrissi, D.H. Koang, B Vignon, and Richard Wilson. Parity non-conservation in the radiative capture of polarized neutrons by 35Cl. *Nuclear Physics A*, 436(1):83–92, March 1985. ISSN 03759474. doi:

10.1016/0375-9474(85)90542-1. URL http://linkinghub.elsevier.com/retrieve/pii/0375947485905421. 33

[43] M Gericke, C Blessinger, J Bowman, R Gillis, J Hartfield, T Ino, M Leuschner, Y Masuda, G Mitchell, S Muto, H Nann, S A Page, S I Penttila, W D Ramsay, P-N Seo, W M Snow, J Tasson, and W S Wilburn. A current mode detector array for γ-ray asymmetry measurements. *Nuclear Instruments and Methods in Physics Research Section A: Accelerators, Spectrometers, Detectors and Associated Equipment*, 540(2-3):328–347, March 2005. ISSN 01689002. doi: 10.1016/j.nima.2004.11.043. URL http://linkinghub.elsevier.com/retrieve/pii/S0168900204024313. 34

[44] H Grassmann and E Lorenz. Properties of CsI (TI)–Renaissance of an old scintillation material. *Nuclear Instruments and Methods in*, 228:323–326, 1985. URL http://www.sciencedirect.com/science/article/pii/0168900285902761. 35

[45] D.R. Tilley. Energy levels of light nuclei A=4*. *Nuclear Physics A*, 541(1):1–104, April 1992. ISSN 0096-6207. 37

[46] Dodder D. Young P. Hale, G. Endf/b-vii.0. Technical report, DIST Dec. 2006. 39, 96

[47] William Happer. Optical Pumping. *Reviews of Modern Physics*, 44(2):169–249, April 1972. doi: 10.1103/RevModPhys.44.169. 44, 49

[48] B. Chann, E. Babcock, L. Anderson, and T. Walker. Skew light propagation in optically thick optical pumping cells. *Physical Review A*, 66(3):1–3, September 2002. ISSN 1050-2947. doi: 10.1103/PhysRevA.66.033406. URL http://link.aps.org/doi/10.1103/PhysRevA.66.033406. 46

[49] Wai Tung Lee, Xin Tong, Dennis Rich, Yun Liu, Michael Fleenor, Akbar Ismaili, Joshua Pierce, Mark Hagen, Jonny Dadras, and J. Lee Robertson. Increasing the pump-up

rate to polarize 3He gas using spin-exchange optical pumping method. *Physica B: Condensed Matter*, 404(17):2670–2672, September 2009. ISSN 09214526. doi: 10.1016/j.physb.2009.06.037. URL `http://linkinghub.elsevier.com/retrieve/pii/S0921452609004025`. 46

[50] M. Romalis and G. Cates. Accurate ˆ{3}He polarimetry using the Rb Zeeman frequency shift due to the Rb-ˆ{3}He spin-exchange collisions. *Physical Review A*, 58(4):3004–3011, October 1998. ISSN 1050-2947. doi: 10.1103/PhysRevA.58.3004. URL `http://link.aps.org/doi/10.1103/PhysRevA.58.3004`. 52

[51] Rademakers F. Canal P. Antcheva I. Buskulic D. Brun, R. *ROOT An Object-Oriented Data Analysis Framework, Users Guide 5.20*, 2008. 63

[52] N. Fomin. Summary of measurements with lithium plastic shielding. Technical report, 2011. Technical Report. 68

[53] K. Lefmann and K. Nielsen. Mcstas, a general software package for neutron ray-tracing simulations. *Neutron News*, 10(3):20–23, 1999. 69

[54] Farhi E. Knudsen E. Filges U. Willendrup, P. and K. Lefmann. *User and programmers guide to the neutron ray-tracing package McStas, version 2.0*, 2012. 69

[55] T Chupp, K Coulter, M Kandes, M Sharma, T Smith, G Jones, W Chen, T Gentile, D Rich, and B Lauss. A large area polarized 3He neutron spin filter. *Nuclear Instruments and Methods in Physics Research Section A: Accelerators, Spectrometers, Detectors and Associated Equipment*, 574(3):500–509, May 2007. ISSN 01689002. doi: 10.1016/j.nima.2007.02.091. URL `http://linkinghub.elsevier.com/retrieve/pii/S0168900207004111`. 79, 96

[56] S.F. Mughabghab and N.E. Holden. *Neutron Cross Sections: Neutron Resonance Parameters and Thermal Cross Sections*. Neutron Cross Sections Vol. 1. Academic

Press, 1984. ISBN 9780125097116. URL `http://books.google.com/books?id=cgk6AQAAIAAJ`. 95, 96

[57] Denise B Pelowitz. MCNPX User's Manual. 2011. 103

Appendix

Table A.1: Data summary for Fig. 5.10. The ^{3}He thickness of the ^{3}He cell Hedy Lamarr.

Wavelength (Å)	^{3}He Thickness
2.34835	1.1297
2.43994	1.05065
2.53153	1.01419
2.62312	0.996537
2.71472	0.98758
2.80631	0.983938
2.8979	0.98365
2.9895	0.983019
3.08109	0.98183
3.17268	0.977392
3.26428	0.975088
3.35587	0.968235
3.44746	0.964854
3.53906	0.958768
3.63065	0.945833
3.72224	0.930441
3.81384	0.948945
3.90543	0.957469
3.99702	0.966371
4.08862	0.9699
4.18021	0.96754
4.2718	0.951984
4.36339	0.934081
4.45499	0.915379
4.54658	0.902263
4.63817	0.903416
4.72977	0.917501
4.82136	0.943919
4.91295	0.962916
5.00455	0.967603
5.09614	0.95494
5.18773	0.917381
5.27933	0.869285
5.37092	0.830127
5.46251	0.794091
5.55411	0.770054
5.6457	0.758218
5.73729	0.776017
5.82889	0.763238
5.92048	0.637457

Table A.2: Data summary for Fig. 5.12a. The measured spin-flip efficiency compared to the RFSF and beamline models at the center of the neutron beam.

Wavelength (Å)	Data 1	Data 2	Data 3	RFSF Model
3.53906	0.992503	0.992657	0.992408	0.99284
3.63065	0.993469	0.99353	0.993435	0.992747
3.72224	0.993788	0.994032	0.993671	0.992664
3.81384	0.994032	0.993994	0.994112	0.992677
3.90543	0.994084	0.994058	0.993919	0.992594
3.99702	0.994062	0.994071	0.993734	0.992669
4.08861	0.994204	0.994192	0.993537	0.992715
4.18021	0.994371	0.994211	0.993786	0.992806
4.2718	0.994486	0.994489	0.993863	0.992673
4.36339	0.994629	0.994543	0.994078	0.992598
4.45499	0.994631	0.994326	0.994051	0.992558
4.54658	0.994807	0.994545	0.994166	0.992555
4.63817	0.994857	0.994587	0.994673	0.992437
4.72977	0.994953	0.994807	0.99438	0.992521
4.82136	0.995019	0.994818	0.994424	0.992498
4.91295	0.994947	0.994841	0.994623	0.992561
5.00455	0.995096	0.99496	0.994795	0.992619
5.09614	0.995005	0.994762	0.994622	0.99259
5.18773	0.995001	0.994734	0.994299	0.992408
5.27933	0.994994	0.994945	0.994051	0.99261
5.37092	0.99499	0.994852	0.994346	0.99249
5.46251	0.994926	0.99457	0.994001	0.99255
5.55411	0.994938	0.994924	0.994206	0.992592
5.6457	0.994908	0.994835	0.993457	0.992383
5.73729	0.994606	0.99415	0.993376	0.992507

Table A.3: Data summary for Fig. 5.12b. The measured spin-flip efficiency compared to the RFSF and beamline models 4 cm beam-right of center.

Wavelength (Å)	Data	RFSF Model
3.53906	0.96666	0.968316
3.63065	0.966214	0.968628
3.72224	0.96592	0.968509
3.81384	0.965661	0.968906
3.90543	0.965389	0.968427
3.99702	0.965511	0.968329
4.08861	0.965641	0.968757
4.18021	0.965978	0.967975
4.2718	0.966309	0.968491
4.36339	0.966917	0.968974
4.45499	0.967357	0.969398
4.54658	0.967656	0.968743
4.63817	0.968166	0.969062
4.72977	0.968709	0.969385
4.82136	0.969199	0.969739
4.91295	0.969519	0.970054
5.00455	0.969825	0.969663
5.09614	0.970172	0.969938
5.18773	0.970838	0.970094
5.27933	0.970901	0.970084
5.37092	0.971127	0.969877
5.46251	0.971539	0.970327
5.55411	0.97194	0.969637
5.6457	0.971798	0.970272
5.73729	0.970294	0.970202

Table A.4: Data summary for Fig. 5.14. The neutron room background when polarimetry measurements were performed to determine the beam average polarization.

Wavelength (Å)	Background
3.72224	0.0139863
3.81384	0.0152772
3.90543	0.0160073
3.99702	0.0136479
4.08862	0.0179385
4.18021	0.015246
4.2718	0.0227232
4.36339	0.0213643
4.45499	0.0230465
4.54658	0.0231046
4.63817	0.0224707
4.72977	0.0224575
4.82136	0.0225785
4.91295	0.0227863
5.00455	0.0233705
5.09614	0.0217343
5.18773	0.0204534
5.27933	0.0196171
5.37092	0.0190129
5.46251	0.0181028
5.55411	0.0176798
5.6457	0.0163861
5.73729	0.0169148

Table A.5: Data summary for Fig. 5.16a. The neutron polarization measured at the top of the neutron beam.

Wavelength (Å)	Top Beam-Left	Top Beam-Center	Top Beam-Right
3.72224	1.08317	0.965076	0.949425
3.81384	1.0693	0.965357	0.950934
3.90543	1.05277	0.965039	0.95231
3.99702	1.03698	0.963385	0.95133
4.08861	1.02771	0.964239	0.955788
4.18021	1.01103	0.961918	0.951692
4.2718	1.00514	0.962672	0.95654
4.36339	0.995349	0.960683	0.955893
4.45499	0.989183	0.96023	0.957343
4.54658	0.982162	0.95912	0.957728
4.63817	0.974784	0.95801	0.95732
4.72977	0.967608	0.956976	0.957887
4.82136	0.961206	0.955475	0.956864
4.91295	0.953757	0.954094	0.955921
5.00455	0.951109	0.953235	0.957051
5.09614	0.945931	0.951656	0.956409
5.18773	0.940587	0.950198	0.954927
5.27933	0.935776	0.948824	0.95446
5.37092	0.930912	0.947579	0.953901
5.46251	0.926373	0.946175	0.952739
5.55411	0.921771	0.944704	0.952435
5.6457	0.916116	0.942901	0.950503
5.73729	0.913807	0.942339	0.951078

Table A.6: Data summary for Fig. 5.16b. The neutron polarization measured at the center of the neutron beam.

Wavelength (Å)	Center Beam-Left	Center Beam-Center	Center Beam-Right
3.72224	0.943399	0.955783	0.957673
3.81384	0.944361	0.9563	0.957996
3.90543	0.943517	0.956223	0.957826
3.99702	0.941241	0.955565	0.956638
4.08861	0.941111	0.955878	0.957964
4.18021	0.938078	0.954262	0.955782
4.2718	0.937556	0.954672	0.956988
4.36339	0.935078	0.953505	0.955808
4.45499	0.933475	0.952881	0.955679
4.54658	0.931682	0.951825	0.955357
4.63817	0.929306	0.95078	0.954744
4.72977	0.92744	0.949803	0.954044
4.82136	0.925098	0.94849	0.952882
4.91295	0.922109	0.947334	0.952074
5.00455	0.92072	0.946469	0.951617
5.09614	0.918742	0.945072	0.950449
5.18773	0.915648	0.943666	0.949304
5.27933	0.913316	0.942357	0.948189
5.37092	0.910847	0.941221	0.947095
5.46251	0.908059	0.93949	0.946183
5.55411	0.905318	0.93838	0.945455
5.6457	0.902217	0.936698	0.94335
5.73729	0.899794	0.935478	0.942794

Table A.7: Data summary for Fig. 5.16c. The neutron polarization measured at the bottom of the neutron beam.

Wavelength (Å)	Bottom Beam-Left	Bottom Beam-Center	Bottom Beam-Right
3.72224	0.944795	0.950074	0.947109
3.81384	0.946808	0.951245	0.947683
3.90543	0.946288	0.951836	0.948462
3.99702	0.944535	0.951594	0.947448
4.08861	0.945553	0.952951	0.949546
4.18021	0.942513	0.951375	0.947627
4.2718	0.942998	0.952625	0.94987
4.36339	0.940739	0.951759	0.948871
4.45499	0.939952	0.951645	0.949383
4.54658	0.93854	0.951195	0.949319
4.63817	0.936619	0.950722	0.948606
4.72977	0.935253	0.949952	0.948628
4.82136	0.933511	0.949121	0.947671
4.91295	0.931605	0.948326	0.946974
5.00455	0.930373	0.94798	0.947092
5.09614	0.928125	0.946742	0.9457
5.18773	0.926027	0.945488	0.944405
5.27933	0.924379	0.944642	0.943436
5.37092	0.921889	0.943692	0.942589
5.46251	0.919841	0.942696	0.941551
5.55411	0.917644	0.941669	0.940854
5.6457	0.91512	0.940344	0.939231
5.73729	0.913702	0.939974	0.938431

Table A.8: Data summary for Fig. 5.18. The beam-average neutron polarization incident on the para-hydrogen, aluminum, and chlorine targets.

Wavelength (Å)	Polarization, para-H2	Polarization, Al & Cl
3.72224	0.951677±0.00382114	0.952986±0.00363297
3.81384	0.952613±0.00376058	0.953807±0.00359077
3.90543	0.952599±0.00374655	0.953663±0.00358898
3.99702	0.951454±0.0037698	0.952588±0.00360136
4.08861	0.952584±0.00374096	0.953557±0.00359114
4.18021	0.950273±0.00380015	0.951229±0.00365798
4.2718	0.95127±0.00380109	0.952304±0.00364853
4.36339	0.949755±0.00386391	0.950842±0.0037192
4.45499	0.94939±0.0038986	0.950451±0.00375088
4.54658	0.948516±0.00396075	0.949647±0.00381114
4.63817	0.947363±0.00403493	0.948494±0.00388083
4.72977	0.946405±0.00411166	0.94765±0.00393882
4.82136	0.945018±0.00419389	0.946389±0.00402647
4.91295	0.94355±0.00430926	0.944966±0.00412136
5.00455	0.942878±0.00439763	0.944306±0.00421686
5.09614	0.941311±0.00451255	0.942743±0.0043218
5.18773	0.939558±0.00464516	0.941241±0.00443919
5.27933	0.938141±0.00477505	0.93988±0.00456705
5.37092	0.936641±0.00492778	0.938634±0.00470878
5.46251	0.934954±0.00508628	0.93708±0.00487343
5.55411	0.933498±0.00526048	0.935882±0.00503295
5.6457	0.931299±0.00545277	0.9339±0.0052116
5.73729	0.930199±0.00562758	0.932956±0.0053798

Table A.9: Data summary for Fig. 5.19. The beam-average spin-flip efficiency for the para-hydrogen, aluminum, and chlorine targets.

Wavelength (Å)	Spin-Flip Eff., para-H2	Spin-Flip Eff., Al & Cl
3.72224	0.974753±0.00213991	0.977988±0.00146997
3.81384	0.974918±0.00213809	0.978061±0.00144559
3.90543	0.975007±0.00205884	0.977965±0.00145265
3.99702	0.975119±0.00216827	0.978216±0.00141197
4.08861	0.975239±0.00208909	0.978217±0.0014671
4.18021	0.975114±0.00219285	0.97805±0.00142548
4.2718	0.975231±0.00222058	0.978386±0.00150375
4.36339	0.975478±0.00233839	0.978479±0.00154476
4.45499	0.975525±0.00230987	0.978615±0.00158363
4.54658	0.975534±0.00235644	0.978619±0.00156713
4.63817	0.975533±0.00248437	0.978597±0.00165868
4.72977	0.975634±0.00235142	0.978902±0.00171702
4.82136	0.975694±0.00242683	0.979004±0.00171351
4.91295	0.975596±0.00250718	0.97892±0.00173712
5.00455	0.975464±0.00248421	0.978739±0.00176953
5.09614	0.97578±0.00246134	0.978987±0.00180444
5.18773	0.975612±0.00260414	0.979134±0.00181284
5.27933	0.975423±0.00263553	0.978979±0.0018344
5.37092	0.975414±0.00276562	0.979072±0.00189064
5.46251	0.975407±0.00265192	0.978991±0.0019562
5.55411	0.975207±0.00268431	0.978837±0.00193293
5.6457	0.975439±0.00269008	0.979144±0.00195428
5.73729	0.975203±0.00275966	0.979091±0.00201893

Table A.10: Data summary for Fig. 5.20. The simulated and measured capture rates of the para-hydrogen, aluminum, and chlorine targets.

Wavelength (Å)	H2 & Boron Sig. Ratio	H2 MCNPX Capture Rate	Al & Boron Sig. Ratio	Al MCNPX Capture Rate	Cl & Boron Sig. Ratio	Cl MCNPX Capture Rate
3.72224	0.516506	0.547754	0.185124	0.178391	0.287669	0.41604
3.81384	0.600404	0.579275	0.183916	0.181403	0.339628	0.418797
3.90543	0.706982	0.611425	0.193304	0.184045	0.393212	0.422496
3.99702	0.765534	0.647706	0.196432	0.18804	0.418579	0.427728
4.08861	0.840746	0.681704	0.197231	0.200866	0.458586	0.43367
4.18021	0.845049	0.712053	0.196691	0.203123	0.466762	0.43452
4.2718	0.863677	0.743567	0.199934	0.208443	0.458324	0.444376
4.36339	0.876393	0.770696	0.208748	0.210009	0.456756	0.44542
4.45499	0.888455	0.800084	0.222397	0.217239	0.457638	0.44716
4.54658	0.898951	0.833904	0.236548	0.222172	0.458125	0.450685
4.63817	0.903657	0.86802	0.247396	0.245009	0.459742	0.457393
4.72977	0.910259	0.893024	0.254427	0.257481	0.477968	0.455714
4.82136	0.921231	0.91839	0.259158	0.261704	0.476699	0.461649
4.91295	0.944748	0.943208	0.26326	0.264429	0.466755	0.463006
5.00455	0.956088	0.967723	0.267075	0.266568	0.464319	0.462836
5.09614	0.964882	0.986751	0.27068	0.273207	0.464299	0.470274
5.18773	0.972874	1.00146	0.274145	0.275426	0.464549	0.472114
5.27933	0.980309	1.02854	0.277326	0.279153	0.464726	0.474831
5.37092	0.987424	1.0417	0.280356	0.281952	0.464727	0.477204
5.46251	0.994405	1.05879	0.283288	0.286483	0.464514	0.479881
5.55411	1.00153	1.07039	0.286063	0.288718	0.464231	0.480609
5.6457	1.00861	1.08926	0.288798	0.291988	0.464029	0.482509
5.73729	1.01704	1.10881	0.291547	0.294473	0.464176	0.480617

Table A.11: Data summary for Fig. 5.21. The beam-average neutron flux normalized to an average value of 1.0 between 3.7 Å to 5.8 Å.

Wavelength (Å)	McStas Simulation	Boron Target Signal	Unp. ^{3}He Transmission
3.72224	1.11406	0.888709	0.88008
3.81384	1.15642	0.950372	0.911694
3.90543	1.18288	0.931851	0.925099
3.99702	1.20009	0.91858	0.921067
4.08861	1.20331	0.895643	0.875456
4.18021	1.18192	0.998632	0.965951
4.2718	1.16258	1.06388	1.05616
4.36339	1.15589	1.08487	1.08769
4.45499	1.12508	1.08727	1.09271
4.54658	1.10151	1.08157	1.08974
4.63817	1.06432	1.06863	1.07879
4.72977	1.03987	1.06074	1.05927
4.82136	1.03508	1.09019	1.08483
4.91295	1.00676	1.10425	1.12143
5.00455	0.965218	1.09196	1.10414
5.09614	0.937203	1.07045	1.08253
5.18773	0.905963	1.04609	1.05735
5.27933	0.876418	1.02043	1.02975
5.37092	0.843191	0.993928	1.00041
5.46251	0.806311	0.96682	0.972978
5.55411	0.779246	0.939203	0.942141
5.6457	0.758351	0.910999	0.916827
5.73729	0.733681	0.882206	0.88317

Table A.12: Data summary for Fig. 5.22. The measured beam-average polarization, the simulated polarization, the beam-average polarization extrapolated to larger wavelengths with the McStas simulation, and the measured polarization with th new chopper phases.

Wavelength (Å)	Beam-Average Polarization	McStas Simulation	Extrapolated Polarization	Jan. 2013 Polarization
3.44746	0.951985±0.00387381	0.978696	0.951985	0.948289
3.53906	0.951599±0.0038505	0.980312	0.951599	0.971124
3.63065	0.95177±0.00381397	0.979206	0.95177	0.973026
3.72224	0.951677±0.00382114	0.979245	0.951677	0.970451
3.81384	0.952613±0.00376058	0.979801	0.952613	0.966095
3.90543	0.952599±0.00374655	0.979404	0.952599	0.960934
3.99702	0.951454±0.0037698	0.97802	0.951454	0.956519
4.08861	0.952584±0.00374096	0.976651	0.952584	0.954331
4.18021	0.950273±0.00380015	0.975603	0.950273	0.952845
4.2718	0.95127±0.00380109	0.976048	0.95127	0.951797
4.36339	0.949755±0.00386391	0.974072	0.949755	0.950964
4.45499	0.94939±0.0038986	0.972138	0.94939	0.949935
4.54658	0.948516±0.00396075	0.971953	0.948516	0.948843
4.63817	0.947363±0.00403493	0.970774	0.947363	0.94757
4.72977	0.946405±0.00411166	0.971547	0.946405	0.946559
4.82136	0.945018±0.00419389	0.968274	0.945018	0.945213
4.91295	0.94355±0.00430926	0.968407	0.94355	0.943818
5.00455	0.942878±0.00439763	0.964616	0.942878	0.942347
5.09614	0.941311±0.00451255	0.965763	0.941311	0.940825
5.18773	0.939558±0.00464516	0.963099	0.939558	0.939362
5.27933	0.938141±0.00477505	0.963205	0.938141	0.93793
5.37092	0.936641±0.00492778	0.959736	0.936641	0.936537
5.46251	0.934954±0.00508628	0.960498	0.934954	0.934753
5.55411	0.933498±0.00526048	0.955048	0.933498	0.933258
5.6457	0.931299±0.00545277	0.955306	0.931299	0.931373
5.73729	0.930199±0.00562758	0.954201	0.930199	0.92991
5.82889	0.930606±0.00565135	0.952233	0.928502	0.928285
5.92048	0.936871±0.00529004	0.949605	0.925782	0.926391
6.01207		0.950281	0.926347	0.924886
6.10366		0.946844	0.922781	0.923294
6.19526		0.946294	0.922084	0.921257
6.28685		0.941495	0.91712	
6.37844		0.940036	0.915477	
6.47004		0.937698	0.912937	
6.56163		0.938664	0.913683	
6.65322		0.942506	0.917286	
6.74482		0.935443	0.909966	
6.83641		0.931004	0.905252	

Table A.13: Data summary for Fig. 6.1. The measured neutron polarization during the running of the NPDGamma experiment with the hydrogen target vessel empty.

Wavelength (Å)	May 2011	Jan. 2013	May 2013
4.16404	0.954547	0.952667	0.952488
4.25268	0.954586	0.951522	0.951465
4.34132	0.953786	0.950772	0.950345
4.42996	0.953052	0.949734	0.94925
4.5186	0.952148	0.948853	0.948118
4.60724	0.951133	0.947416	0.94711
4.69587	0.950165	0.946507	0.945775
4.78451	0.949018	0.945298	0.944741
4.87315	0.947836	0.943811	0.943482
4.96179	0.946873	0.942529	0.942251
5.05043	0.945769	0.940834	0.940899
5.13907	0.944413	0.939629	0.939525
5.22771	0.943095	0.937969	0.93794
5.31634	0.941898	0.936664	0.936859
5.40498	0.940577	0.935213	0.935633
5.49362	0.939113	0.933439	0.934296
5.58226	0.937863	0.932183	0.932745
5.6709	0.936362	0.930055	0.930986
5.75954	0.935377	0.928892	0.929307

Vita

Matthew Martin Musgrave was born on February 1, 1985 to Glenn Musgrave and Eileen Musgrave. After moving to Oak Ridge, TN in 1996, he graduated from Oak Ridge High School in 2003. He attended James Madison University in Harrisonburg, VA until 2006, when he graduated with a B.S. with a double major in Physics and Mathematics. He then attended the University of Tennessee, Knoxville, where he studied experimental nuclear physics and received his Ph.D. in 2013